



UNIVERSITÀ DEGLI STUDI
DI NAPOLI FEDERICO II

Corso di Dottorato in Ingegneria Industriale (XXXII ciclo)

**Compressor and hybrid ejector systems:
assessment of performance and costs
based on current technology via
experiments and models**

Supervisors

Prof. Rita Mastrullo

Prof. Alfonso William Mauro

PhD Coordinator

Prof. Michele Grassi

PhD Candidate

Gianluca Lillo

April 2020

Abstract

The fast growth of the world population leads to an increase of the global energy demand and carbon dioxide emissions, with an increase of the worldwide average temperature. Residential and commercial buildings represent the most energy-consuming sector with an electricity consumption approximately equal to 60% of the worldwide one. In particular, over 70% of the residential energy requests are due to air-conditioning systems. The reduction of the primary energy consumption related to the residential sector can be obtained by acting on the building envelope as well as by using more efficient heating and cooling systems.

According to this scenario, electrical heat pump technology represents a very efficient solution and their adoption is expected to be much larger into the energy transition to renewable energy sources. The recent regulations imposed two opposite targets: the introduction of new eco-friendly refrigerants and the improvement of performance, with the adoption of new technologies/plant schemes. However, the use of new refrigerants does not imply the increase of the performances. In this thesis two heat pump types will be investigated, one driven by electricity and the other one by heat (waste heat or produced by renewable energies) both using a technology not so common in the market, the ejector.

The first case study concerns the experimental evaluation of the benefits related to the use of a multi-ejector expansion device in a prototype of an air-to-water carbon dioxide heat pump for sanitary hot water production. The effects of the ejector geometry and the operating conditions on the system as well as on the ejector performance are analysed. The sizing of the ejector represents one of the main technical issues in order to maximize the benefits in the use of the ejector with respect to a conventional vapor compression cycle: from this point of view, a comparison between the experimental data and predictive methods by the literature is carried-out. Furthermore, a new correlation calibrated on experimental data is proposed.

The second case study investigates the possible technical and economical convenience in the use of a hybrid ejector cooling system powered by an heat source, where the ejector realizes the expansion of the high pressure fluid from the direct cycle and drives the low pressure flow from the inverse cycle to produce cooling effect. In this analysis different working fluids are considered, paying more attention to eco-friendly solutions such as

hydrocarbons, HFOs and natural fluids (R717, R600, R600a, R290, R1233zd, R1234ze). The HFC R134a is considered due to its wide usage in vapor compression cycles, despite its high GWP. Costs functions for each component are considered to estimate the investment costs and to compare the hybrid ejector cycle with the current heat driven technology on the market.

List of contents

1	Introduction	1
1.1	Motivations and Background.....	1
1.2	Structure of the thesis.....	4
2	Vapor compression cycle using ejector as expansion device: system analysis.....	6
2.1	State of the art	7
2.2	Objective of the research	11
2.3	Experimental activity	12
2.3.1	Test facility.....	12
2.3.2	Experimental procedure	15
2.3.3	Data reduction	17
2.3.4	Uncertainty analysis	18
2.3.5	Test results.....	20
	Influence of different multi-ejector configuration on system performance	21
	Influence of source and sink temperatures on system performance.....	23
	Influence of compressor frequency on system performance.....	24
2.4	Main outcomes of the chapter.....	26
3	Prediction of primary mass flow rate for the ejector device in transcritical vapor compression cycles	28
3.1	State of the art	28
3.2	Objectives of the research.....	34
3.3	Experimental results: primary mass flow rate and ejector parameters	34
3.4	Experimental investigation on predictive models for motive flow.....	36
3.4.1	Results and discussion.....	38
3.5	Main outcomes of the chapter.....	43
4	Heat driven ejector systems: thermo-economic analysis and two-phase heat transfer	44

4.1	Heat driven systems state of the art	44
4.1.1	Absorption systems	44
4.1.2	Combined ORC/VCC systems	45
4.1.3	Heat driven ejector systems.....	48
4.2	Objectives of the research.....	52
4.3	Thermo-economic analysis of heat driven ejector cycle.....	53
4.3.1	Ejector model	54
	Governing equations	57
	Computational procedure	61
4.3.2	Heat exchanger modelling.....	61
4.3.3	Working fluids.....	65
4.3.4	Cost function	66
4.3.5	Performance analysis.....	67
4.4	Thermo-economic optimization.....	70
4.4.1	Case study analysis.....	74
4.5	Focus on two-phase heat transfer at high temperature for low GWP refrigerants	78
4.5.1	Test facility.....	79
	Test section.....	80
	Measurement instrumentation	81
	Experimental procedure	81
4.5.2	Experimental method	82
	Data reduction	82
	Uncertainty analysis and validation	83
4.5.3	Experimental results: effect of operating conditions on heat transfer coefficient 84	
	R1233zd(E)	84

Propane (R290)	87
4.5.4 Assessment with prediction methods by literature.....	89
4.6 Main outcomes of the chapter.....	90
4.6.1 Summary of the WHRHEC thermo-economic analysis.....	91
4.6.2 Summary of the experimental results on flow boiling heat transfer at high temperature	92
5 Design of a heat driven ejector cycle prototype.....	94
5.1 Experimental rig description.....	94
5.2 Components selection and sizing.....	96
5.2.1 Compressor.....	97
5.2.2 Low and high-pressure evaporators	100
5.2.3 Condenser.....	102
5.2.4 Sub-cooler	103
5.2.5 Electrical heaters	104
5.2.6 Liquid pump	105
5.2.7 Expansion valve	106
5.3 Measurement instrumentation and data acquisition system.....	107
5.4 3D lay-out	109
6 Conclusions	111
6.1 Summary of the research on two-phase ejector in transcritical vapor compression cycles.....	111
6.2 Summary of the research waste heat driven hybrid ejector cycles	112
6.2.1 Summary of the WHRHEC thermo-economic analysis.....	112
6.2.2 Summary of the experimental results on flow boiling heat transfer at high temperature	113
Appendix	115
A. Thermodynamic analysis results	115

B. Heat exchangers geometrical data	119
Nomenclature	120
List of Figures	125
List of Tables.....	130
Bibliography.....	132

1 Introduction

1.1 Motivations and Background

According to the studies of the International Energy Agency, the global energy demand and carbon dioxide emissions would increase by 37% and 20%, respectively, between 2014 and 2040. Moreover, it is expected that the global average temperature will grow up to 3.6°C in the same period [1]. These trends are led by the three OECD regions (Europe, North America and Pacific) and especially by China, India and Africa, driven by the rapid population growth in developing countries. In particular, the CO₂ emissions are expected to be nearly doubled while the global final energy demand will rise up to 60% in 2050 in the building sectors, as illustrated in International Energy Agency (2010) [2]. These trends are related to the expected growth of the world population (+40% in 2050) and the consequent global number of households (+67% between 2005 and 2050), particularly faster in developing countries. In this scenario, the largest consumption of energy is due to the residential sector, carrying a worldwide energy demand growth of 1% per year until 2050, while in India and China it will grow by 1.7% and 1.1% per year, respectively. The related CO₂ emissions will likewise increase up to 87% in 2050. In particular, the electricity consumption in residential and commercial buildings is approximately 60% of the worldwide one [3]; in Europe, the residential sector requires 27% of the total energy and it contributes proportionally to the emission of CO₂ [4]. To reduce the consumption of primary energy associated to the residential sector it is possible to act on two leverages: from one side reducing the energy demand at the end user side with interventions on the building envelope of the new edifices; on the other side it is possible to reduce the primary energy required to reach the same scope at the user, improving the efficiency of the energy consumption systems used for the heating and the cooling.

Several initiatives have been promoted along these two main streams. For example, with the aim to reduce energy consumption in buildings the Zero Energy Building (ZEB) goal has been defined. In Europe, the Energy Performance of Buildings Directive (2010/31/EU) [5] requires that “Member States shall ensure that by 31 December 2020, all new buildings are nearly zero-energy buildings and after 31 December 2018, new buildings occupied and owned by public authorities are nearly zero-energy buildings”. The application of EU Directives has reduced significantly the energy needed by new

constructions and partially of the stock of existing buildings. The improvements in the building sector are not be independent to the adoption of more efficient heating and cooling systems. From this point of view, electrical heat pump technology is a very efficient solution, especially when the temperature difference with the ambient is small. From an economical point of view its use is not always the most convenient: the reason is that the extra energetic performance in comparison to other available technologies is not enough to compensate the extra cost per unit of energy; this aspect is strictly related to the costs of electrical energy in each country compared to the costs of the other energy sources. Actually, the number of heat pump units sold in the European market in 2018 is growing [6]. European heat pump sales grew by 12.5% in 2018, with 1.26 million of units sold. Assuming a life expectancy of approximately 20 years, the current European heat pump stock amounts of 11.80 million units. With approximately 244 million residential buildings in Europe, the heat pump market share in the buildings stock is about 5%.

The adoption of the heat pump technology is expected to be much larger into the energy transition to renewable energy sources, for two reasons: first, the heat removed from the environment is recognized as equivalent to the adoption of renewable energy sources [7]; second, as the energy transition proceeds the main energy carrier will be the electricity and the electrical heat pumps will allow the production of both heating and cooling in the most of situations. Policy makers are aware about the key role of heat pumps and have encouraged the improvement of their energy performance especially in in the residential sector. In facts EU commission introduced the European regulation Eco-Design [8] which imposes more and more stringent design requirements on the heat pump performance for the space heating and HSW production (space heaters and combination heaters). Potential direct environmental impact of the heat pump technology has been limited by several international regulations related to the limitation in the use of fluorinated gases. Specifically, to reduce the impact of the direct emissions due to possible leakages, the European F-Gas Regulation [9] will progressively limit the total amount of CO₂ corresponding to the refrigerants introduced into the market each year, attaining a limit at 2030 equal to 21% of the average placed on the market into the EU area, in the period 2009-2012. Furthermore, the United States, Canada and Mexico proposed, in 2014, an amendment to the Montreal Protocol to reduce production and consumption of HFCs by 85% during the period 2016-2035, for the developed countries [10].

In this framework, two goals have to be achieved by the research related to the heat pumps: the introduction of new refrigerants with low GWP and the improvement of performance, with new technologies/plant schemes. These two targets required by current regulations are opposed, since the use of new refrigerants does not imply the increase of performances. Also, the attention towards the investment costs require the need for some cost evaluation especially for brand new technologies.

The aim of this thesis is to investigate two heat pumps types: one driven by electricity and the other one by heat (waste heat or produced by renewable energies) both using a technology not so common in the market, the ejector. Regarding the case of the electrical heat pumps the use of the ejector is considered as expansion system of a CO₂ transcritical cycle, where the use of the CO₂ is beneficial for the direct environment impact but potentially detrimental for energy performance; the sector considered is the one related to the sanitary hot water production, where the performance of the CO₂ systems are close to the ones achievable with other HFC refrigerants. The main scope concerns the experimental evaluation of the effective benefits related to the adoption of this new technology and the individuation of potentially technical issues.

The second case study concerns the possibility to realize a hybrid direct/inverse system powered by heat, where an ejector realizes the expansion of the fluid from the direct cycle and drives the flow from the inverse cycle to reach temperatures lower than the ambient. The main scope is the estimation of the performance with different fluids and the estimation of the costs to evaluate the chance of this quite new solution to be a potential option in the market.

Related to the research topics described above, the following activities were carried-out:

1. Study of the state of the art related to the use of a two-phase ejector in vapor compressor cycle as an expansion device; production of experiments on a CO₂ heat pump working under real conditions; data process; study of the benefit of the adoption of the ejector technology at a system level; segregation of the experimental performance of the ejector as a component and assessment of the predictive methods from literature; development of a new correlation to predict the primary flow of the ejector as a function of the boundary conditions.

2. Study of the state of the art related to the use of vapor ejector in heat driven ejector cooling systems; thermo-economic analysis of such a system using different fluids to define the potential of application in the market compared to alternative technologies; design of a prototype.

1.2 Structure of the thesis

The present thesis is divided in six chapters, organized as follows:

- Chapter 1 provides a background to the study, by motivating the work and stating the objectives of the research.
- In Chapter 2, an overview of the state of the art related to the use of a two-phase ejector in vapor compression cycles as expansion device is provided. In the second part of the chapter, the description of the experimental activity on a real heat pump working with CO₂ as refrigerant by employing a multi-ejector system as expanding device is presented. The experimental methodology, data reduction process and evaluation of the experimental uncertainty of all the parameters of interest are also shown. Finally, the experimental results focused on the performance enhancement related to the use of the ejector are illustrated.
- Chapter 3 is focused on the performance of the ejector. In the first part, an overview of the state of the art related to the modelling methodology and predictive methods for the performance evaluation of two-phase ejectors is presented. The experimental data collected and presented in the previous Chapter are used to analyse the performance of the multi-ejector pack at different operating conditions. Furthermore, the experimental data on the primary mass flow rate was compared to prediction methods obtained by literature, finally proposing a new correlation.
- Chapter 4 is focused on the possibility to use the ejector in waste heat driven cooling cycles (Waste Heat Driven Hybrid Ejector Cycles, WHRHEC). In the first part, the state of art of WHRHEC systems is presented as well as conventional heat driven cooling technologies (absorption and combined ORC/VCC systems). In the second part, a thermo-economic analysis of a waste heat recovery hybrid ejector cycle is described, and its results are compared to those collected from the existing technologies. Also, an analysis on the required conditions to obtain an economical convenience for a WHRHEC integrated to

a conventional vapor compression cycle is shown as case study. In the last part, the experimental activity for the collection of experimental data of flow boiling heat transfer coefficient for typical fluids employed in waste heat driven technologies (R1233zd(E) and propane (R290)) is described, by analysing the effects of mass flux, saturation temperature and imposed heat flux on the heat transfer coefficient.

- Chapter 5 provides the design steps of a heat driven ejector cycle prototype, including the definition of the operative conditions of each component and the measurement instrumentation. Finally, a 3-D layout is shown.
- Finally, Chapter 6 summarizes the main outcomes of this work.

2 Vapor compression cycle using ejector as expansion device: system analysis

The use of an ejector as substitute of a common expansion valve in vapor compression cycles results to be an interesting solution for the refrigeration and air-spacing conditioning. The main modifications with respect to the conventional vapor compression cycle are the addition of a two-phase ejector and a liquid-vapor separator at the outlet of the ejector. A schematic lay-out of vapor compression cycle using ejector as expansion device is shown in Figure 1.

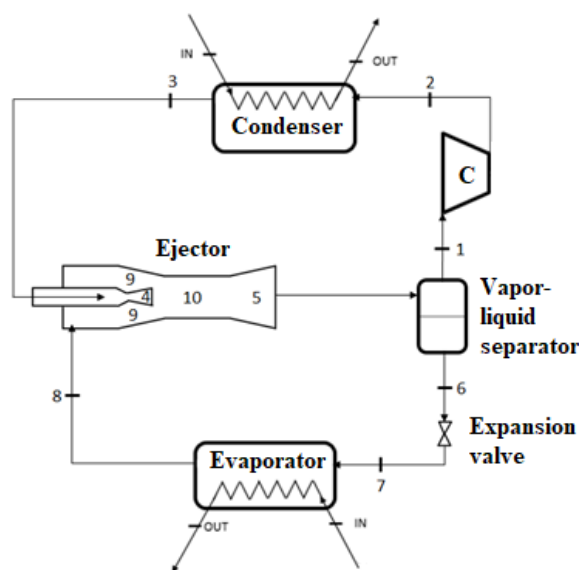


Figure 1. Schematic layout of vapor compression cycle using ejector as expansion device.

The high-pressure primary flow from the condenser (state 3) and the low-pressure secondary flow from the evaporator (state 8) are going through motive and secondary nozzles, respectively. Then both fluids mix in the mixing chamber and flow through the diffuser to convert the kinetic energies of mixture to pressure energy. The flow at the outlet of the ejector (state 5) is characterized by a pressure higher than the evaporating pressure. From the vapor-liquid separator, the liquid (state 6) circulates through the expansion valve and the evaporator, meanwhile the vapor (state 1) circulates through the compressor and the condenser. Several factors, including the properties of the working fluid, influence the COP improvement that can be obtained by using ejector as expansion device. Fluids characterized by high difference between isentropic and isenthalpic expansion in the

expansion device lead to greater irreversibility or throttling loss and hence, offer greater opportunity for performance improvement. It is to note that throttling losses are also proportional to mass flow rate; for the same capacity, the mass flow rate for each fluid is inversely related to the enthalpy difference in the evaporator. Therefore, in view of the previous consideration, carbon dioxide has significantly higher throttling loss compared to low-pressure fluids, especially at elevated ambient temperatures where a CO₂ cycle would operate in transcritical mode; this means that CO₂ has much greater opportunity for COP improvement when using a work recovery device such as an ejector. In order to characterize the performance of the ejectors a quite usual approach in the recent literature of the sector was used. In particular, three parameters are used: the entrainment ratio μ , the pressure lift ratio Π and the ejector efficiency η_{ej} , reported, respectively, in the Equations (2.1), (2.2), (2.3):

$$\mu = \frac{\dot{m}_8}{\dot{m}_3} \quad (2.1)$$

$$\Pi = \frac{p_5}{p_8} \quad (2.2)$$

The ejector efficiency can be defined as the actual amount of work recovered by the ejector divided by the theoretical maximum amount that could be recovered. The processes occurring inside the ejector can be simplified by two different transformations: the expansion of the motive flow and the compression of the secondary flow, both to the pressure at the outlet of the ejector. Different methods to estimate the ejector performance can be found in scientific literature: in this analysis the method proposed by Elbel and Hrnjak [11] was considered. They defined the ejector efficiency, calculated as the power to compress the suction stream with an isentropic transformation from suction inlet to diffuser outlet pressure, divided by an isentropic expansion of the motive stream from motive inlet to diffuser outlet pressure, as shown in Eq. (2.3) according to the numbering in Figure 1.

$$\eta_{ej} = \mu \frac{h(p_5, s_8) - h_8}{h_3 - h(p_5, s_3)} \quad (2.3)$$

2.1 State of the art

At the current state-of-the art of the technology, the ejectors have efficiencies comparable to the ones of the expanders, but they attain much interest for real applications,

since they do not have any moving parts, have low cost and high reliability compared to the expanders. The ejector working principle and its applications in vapor compression refrigeration and heat pump systems was explained in a literature review by Sarkar [12]. Many experimental studies on two-phase ejector expansion systems in transcritical carbon dioxide refrigeration cycles were carried-out. Several studies are related to the experimental evaluation of the system performance by varying the geometrical characteristics of the ejector meanwhile a large number of researches are focused on the comparison between the performance of vapor compression cycle using ejector as expansion device and conventional cycle, by analysing the effects of the operating temperatures. Elbel and Hrnjak (2008) [11] investigated a transcritical CO₂ ejector system with an adjustable ejector in order to control high-side pressure in the transcritical system. Their experimental results showed that the system COP can be maximized by using an adjustable needle able to find the optimum value of the high-side pressure. However, due to higher friction occurring when the flow expands into the motive nozzle the ejector efficiency decreases. They also found that the COP of the ejector cycle increased with internal heat exchanger efficiency while ejector efficiency was not significantly affected by IHE effectiveness. Elbel and Hrnjak (2008) [11] observed simultaneous COP and capacity improvements of 7 and 8%, respectively, and they estimated that COP improvement could reach as high as 18% if capacity were matched; they observed ejector work recovery efficiency of up to 15%.

Liu et al. (2012a) [13] also used an adjustable ejector with a converging-only nozzle to analyze the performance of a transcritical carbon dioxide air conditioner. As reported by the authors, the use of an ejector as expansion device instead of a conventional expansion valve led to an enhancement of the system performance. They observed that an optimum value of the throat size can be found in order to maximize the system performance, with an increase of the COP up to 60% by decreasing the nozzle throat diameter. The ejector system performance is affected by the boundary conditions as well as the compressor frequency: they found a COP enhancement up to 36% and 147% when the outdoor air temperature increased and the compressor frequency decreased (if compared to a conventional cycle with compressor frequency set to 50 Hz), respectively. Liu et al. (2012b) [14] investigated the same ejector and developed a method by which the efficiencies of the (converging-only) motive nozzle, suction nozzle, and mixing section could be determined. They showed that the efficiencies of the motive and suction nozzles generally ranged from about 50% to 90% while the mixing section efficiency ranged from about 50% to 100%; these values are

lower than what are often assumed in theoretical modeling studies described above. They observed that motive nozzle efficiency decreased with decreasing nozzle size; as the needle is inserted further into the nozzle to decrease nozzle opening, more friction between the fluid and needle occurs, lowering nozzle efficiency. This observation agrees with the finding of Elbel and Hrnjak (2008) [11]. The work by Liu et al. (2012b) [14] was an important study because it presented realistic results for ejector component efficiencies over a range of operating conditions and variations in ejector geometry. Numerous studies have investigated the performance of transcritical CO₂ ejector cycles using fixed geometry ejectors without any means of high-side pressure control.

Lee et al. (2011) [15] used a fixed geometry ejector and investigated the effects of motive nozzle throat diameter, motive nozzle outlet position, and mixing diameter, and they observed an optimum value for each of these parameters. They noted that the highest COP was achieved with the motive nozzle size for which the flow just becomes choked. They also observed that the cycle performance was not very sensitive to motive nozzle position for small variations from the optimum position; however, cycle performance could decrease rapidly if this parameter deviated significantly from its optimum. An optimum in entrainment ratio was observed near 0.9, where the evaporator outlet was close to a saturated vapor state. Lee et al. (2011) [15] observed ejector cycle COP improvement of 15% at matched capacity. Lee et al. (2014) [16] continued the study by investigating experimentally the performance of a CO₂ air conditioning system using a two-phase ejector as expansion device and comparing the performance of the ejector system with the conventional system. As the fluid secondary temperature at gas cooler inlet increases from 30 to 40 °C, the total COP was decreased; however, higher secondary fluid temperature leads to higher gas cooler pressure and therefore more work recovery using the ejector. Comparing the performance of the ejector system with respect to conventional vapor compression cycle, COP and cooling capacity increase of about 2-5% and 6-9%. Furthermore, the influence of different values of ambient temperature and compressor frequency on the entrainment ratio are investigated: the optimum entrainment ratio was generally in the range of 0.7-0.9.

The effect of different internal heat exchanger sizes on the performance of a transcritical CO₂ ejector cycle was experimentally investigated by Nakagawa et al. (2011a) [17] and compared with conventional expansion refrigeration system. The experiments

carried-out at different operating pressure and temperature considering the following cycle configurations: without IHE, 30 cm IHE and 60 cm IHE. They found that a larger IHE (greater effectiveness) increased ejector cycle COP with a maximum enhancement in term of COP with respect to conventional system under the same operating conditions up to 27%. Also, they observed ejector work recovery efficiency up to 22% with the largest IHE, while ejector efficiency decreased as IHE effectiveness decreased. The study of Nakagawa et al. (2011a) [17] also noted the fact that the liquid–vapor separator in the ejector cycle does not always separate the two phases perfectly. Separator inefficiency can decrease cycle performance because liquid that leaves the separator at the vapor outlet results in lower evaporator capacity and greater compressor work while vapor that leaves the separator at the liquid outlet results in additional mass flow that the ejector must pump without increasing cooling capacity. Additionally, too much liquid being sent to the compressor can damage the compressor if an IHE is not included in the cycle; note also that the lost capacity due to liquid being sent to the compressor can be partially recovered if an IHE is used in the cycle. Nakagawa et al. (2011a) [17] estimated that the quality of refrigerant leaving the separator at the vapor port was approximately 0.9, meaning that a significant amount of liquid was not being separated properly. Thus, when designing and operating an ejector cycle, one should be aware of the effect that poor liquid–vapor separation can have on the cycle.

In the experimental work of Nakagawa et al. (2011b) [18] the effect of mixing section length on the performance of a fixed geometry two-phase ejector for CO₂ refrigeration cycle was investigated. The experiments were carried-out for both ejector and conventional system analyzing also the effect on the internal heat exchanger. It was found that there was an optimum in the mixing section length and that this optimum value was not affected using IHE. A maximum COP improvement of up to 26% compared to similar conventional systems can be obtained for ejector system with IHE using the optimum value of the mixing section length among the range investigated by the authors. However, improper sizing of mixing length could lower the COP by as much as 10%.

Banasiak et al. (2012) [19] investigated experimentally and numerically the effects of various ejector geometry on the performance of a small capacity transcritical carbon dioxide heat pump. The experimental investigation revealed that the COP of the ejector system could obtain improvement in a range 6-8% with respect to a system with classic

expansion valve (for non-optimized systems). The experimental results also showed they also showed that ejector efficiency can be maximized by setting the high-side pressure at the optimum value by changing compressor frequency. In this analysis the effect of the length and diameter of the mixing section and the diffuser angle on the ejector performance was investigated obtaining an ejector work recovery efficiency of up to 31%.

The experimental work of Lucas and Koehler (2012) [20] show the comparison between the traditional carbon dioxide refrigeration system and ejector refrigeration cycle (both without internal heat exchanger) varying the high-side pressure for different evaporation pressures and gas cooler outlet temperatures. The optimum values of the high-side pressure for a fixed geometry ejector was obtained by varying the compressor speed in order to maximize the COP for a given operating conditions. Furthermore, the performance of the ejector in terms of entrainment ratio, pressure lift and efficiency are investigated. The authors observed ejector cycle COP improvement of up to 17% at matched capacity while achieving ejector work recovery efficiency of up to 22%. The COP improvement is increasing with increasing gas cooler outlet temperature at the higher evaporation pressure. At the lower evaporation pressure, no clear trend of the COP improvement with respect to the gas cooler temperature can be determined.

Minetto et al. (2013) [21] presented an experimental analysis of a 5 kW heating power prototype R744 water/water heat pump which was equipped with a two-phase ejector. In order to obtain a comparison between ejector system and traditional expansion valve system, the same heat pump was also provided with a back-pressure valve as the expansion device. Tests were performed to evaluate the performance when the heat pump produced hot tap water (~ 60 °C). Additionally, an investigation took place to understand how the system performed when space heating was required, i.e. providing hot water with a limited temperature lift, however at relatively high inlet temperatures. Experiments demonstrated that the ejector is helpful to improve the heat pump performance, thus promoting the diffusion of R744 units also for domestic space heating and air conditioning. Technological issues related to lubricant recovery were carried-out.

2.2 Objective of the research

According the state of the art on the use of two-phase ejector in vapor compression cycles, most of the researches are related to refrigeration cycles with fixed geometry ejector

or ejector using variable motive nozzle throat. In the refrigeration sector, the stability of operating pressures facilitates the ejector working with high efficiency. On the contrary, in the air-conditioning sector, due to the high outlet temperature at the gas cooler, large benefits could be obtained; however, there are variable operating conditions and the real benefit related to the use of ejectors is still under investigation. Although the system optimization is possible with an ejector with variable throat area, the shape factor among the ejector parts does not correspond to the optimal one for all the operating conditions, causing lower ejector efficiency. The main technical issue is related to the fact that as the balancing among the components changes (due to different boundary conditions and/or different loads) the ejector should have a variable section at the throat.

Therefore, the aim of the research is to verify experimentally the effective performance reached by a real heat pump working with the CO₂ as refrigerant provided by a multi-ejector system as expanding device instead of a traditional expansion valve. A thermodynamic analysis, with varying the ejector system configuration characterized by different geometries, the operation condition and the compressor frequency, was run to investigate the effect of these parameters on the balancing of the whole system and consequently on its global performances.

2.3 Experimental activity

2.3.1 Test facility

The tests were run using the experimental facility “Calorimetro Enea” at ENEA (Casaccia) research center. The climatic chamber, showed in Figure 2a, allows to test an air-to-water reversible heat pump, with thermal capacity until 50 kW, according to UNI EN 14511/2011 [22]. It is possible to control and measure the air conditions in terms of temperature (in a range -15°C/35°C), relative humidity (from 10% to 95%) and the air speed in the climatic chamber under 1 m s⁻¹. Therefore, the stability of the test conditions and the measurement accuracy within the limits are ensured. Furthermore, it is possible to set the water mass flow rate at the gas cooler. The prototype, showed in Figure 2b, is a heat pump with components assembled on a frame typical for a commercial product and was intended to demonstrate the feasibility of the use of such a solution with real spacing. Specifically, it consists in an air-to-water carbon dioxide heat pump with heating capacity of 30 kW at nominal conditions ($T_{w,in} = 40^{\circ}\text{C}$, $T_{w,out} = 60^{\circ}\text{C}$ and $T_{amb} = 7^{\circ}\text{C}$). The multi-

ejector CO₂ system consists of an alternative semi-hermetic compressor (CP) driven by an inverter, a plate heat exchanger (GC), a finned coil (EVAP), a plate internal heat exchanger (IHE), an electronic valve (EEV) and a multi-ejector expansion pack (EJEC), including four ejectors with different geometries.



Figure 2. (a) Climatic chamber at ENEA research center. (b) Prototype of a carbon dioxide heat pump with multi-ejector system as expansion device.

At the outlet of the multi-ejector pack the mixed flow in saturated condition flows inside a vapor-liquid separator. The use of the IHE has been necessary to prevent that in some operating conditions large fractions of liquid entrained in the vapor core at the exit of the liquid separator could reach the compressor suction. Also, the IHE is necessary to vaporize the liquid refrigerant solved into the lubricant, when it is pulled out from the bottom of the liquid separator. Table 1 shows the motive nozzle geometric characteristics, as provided by the manufacturer. Ejectors with the same shape ratio are employed in the multi-ejector pack installed on the heat pump: the ratio between the throat sections diameters is equal to $\sqrt{2}$.

Table 1. Motive nozzle geometric characteristics.

Ejectors [#]	Inlet diameter [mm]	Throat diameter [mm]	Outlet diameter [mm]	Converging angle [°]	Diverging angle [°]
1	3.8	0.70	0.78	30	2
2	3.8	1.00	1.12	30	2
3	3.8	1.41	1.58	30	2
4	3.8	2.00	2.24	30	2

The heat pump control system can activate each ejector independently, depending on operation conditions, with 15 different configurations. Therefore, different overall cross sections can be obtained. Figure 3 shows a schematic layout of the multi ejector prototype with the location of the temperature measurements and the pressure gauges. The location of the points showed in the system layout are specified on the thermodynamic cycles in Figure 4. The figure also shows the location of the points within the ejector which are not evaluated with experimental data. Therefore, the trends of the transformations inside the ejector are only qualitative and indicated with dotted lines and they are evaluated by assuming isentropic expansion and compression processes and constant pressure mixing process. The point 11 represents the CO₂ thermodynamic state at the exit of the motive nozzle; the point 12 represents the state of CO₂ secondary flow, after expansion in the ejector; the point 13 denotes the CO₂ state after the mixing zone of ejector. These illustrative cycles were obtained at T_{amb} of 7°C, $T_{w,in}$ of 40°C, $T_{w,out}$ of 60°C and heating capacity of 11.7 kW. All measurement instruments accuracies satisfy the UNI EN 14511 indications [22]. Table 2 summarizes the instrument specifications and their uncertainty. K-type and J-type thermocouples and pressure sensors are installed at the inlet and outlet of each component. The water volumetric flow rate is measured by an electromagnetic transmitter. The electrical power (including the compressor and the auxiliary components) is measured by a wattmeter.

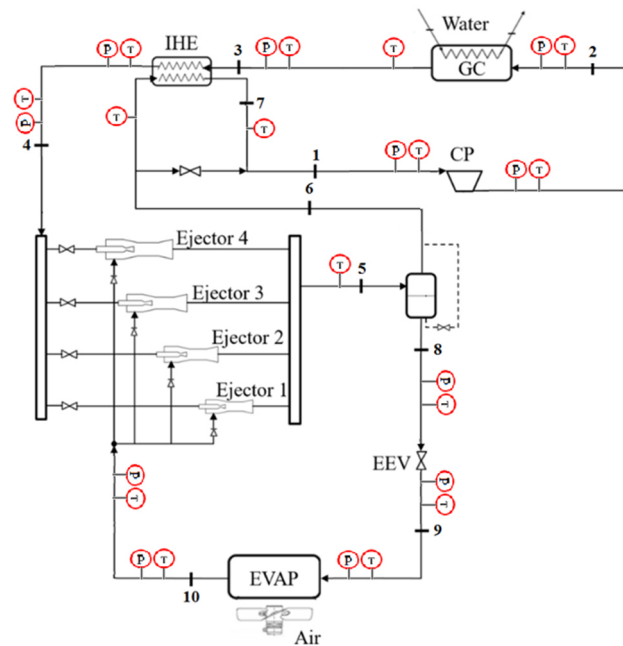


Figure 3. Schematic layout of multi ejector expansion CO₂ vapor compression system.

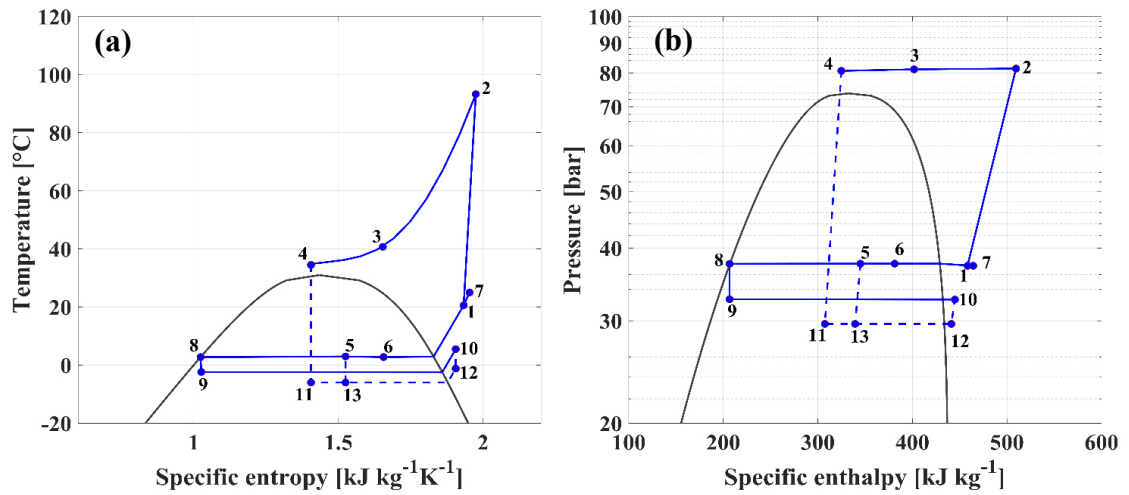


Figure 4. Thermodynamic cycles on (a) T - s and (b) p - h diagram of the multi ejector heat pump at the following operating conditions: T_{amb} of 7°C , $T_{w,in}$ of 40°C , $T_{w,out}$ of 60°C and heating capacity of 11.7 kW .

Table 2. Measurement instrumentation and uncertainty.

Measurement	Range/Unit	Uncertainty/ Precision class
Temperature (K-type)	0/150 $^{\circ}\text{C}$	$\pm 0.4\%$ reading
Temperature (J-type)	-40/80 $^{\circ}\text{C}$	$\pm 0.4\%$ reading
Pressure	0/60 - 0/100 - 0/160 bar	0.08% full scale
Water volumetric flow rate	0/200 l min^{-1}	0.02% reading
Electrical power	0/25 kW	0.5

2.3.2 Experimental procedure

During the tests, the total throat area of the ejectors was kept constant because it was possible to set manually the ejectors configuration. Also, all the other operating parameters, internal to the heat pump circuit, were kept constant (i.e. compressor frequency, throttling valve opening) in order to run a parametric analysis under fixed and stable thermodynamic conditions. Air and water flows were controlled according to UNI EN 14511, part 3 [22]: periodic fluctuations of the measured quantities caused by the operation of regulation and control devices are permissible, on condition the mean value of such fluctuations does not exceed the permissible deviations listed in Table 3. Considering a test characterized by $T_{w,in}$ of 40°C , a $T_{w,out}$ of 60°C and a T_{amb} of 7°C , the inverter of the compressor of 50 Hz and ejector n^o3, Figure 5 and Figure 6 show the trends of the operating temperatures and the pressure levels respectively during the test. The variation of the gas cooler pressure

compared to the mean value is within $\pm 0.14\%$ whereas the evaporator pressure one is within $\pm 1.12\%$. During the tests, it was possible to set the outlet evaporator and inlet compressor superheating. The trends of the thermodynamic measured variables were monitored via a software specifically designed. The main thermodynamic parameters were recorded and processed using Matlab software [23].

Table 3. Permissible deviations from set values [22].

Measured quantity	Permissible deviation of the arithmetic mean values from set values	Permissible deviations of individual measured values from set values
Liquid		
Inlet temperature	± 0.2 K	± 0.5 K
Outlet temperature	± 0.3 K	± 0.6 K
Volumetric flow rate	$\pm 1\%$	$\pm 2.5\%$
Air		
Inlet temperature	± 0.3 K	± 1 K

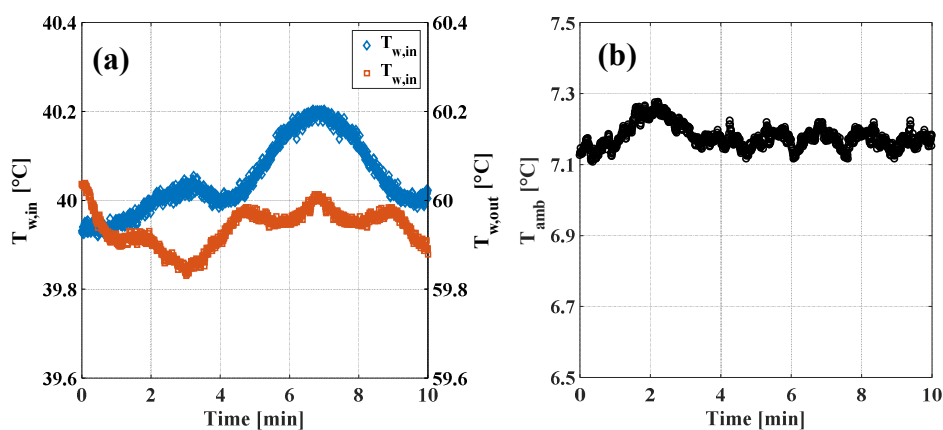


Figure 5. Gas cooler inlet and outlet water temperatures (a) and climatic chamber temperature (b) variations during the test.

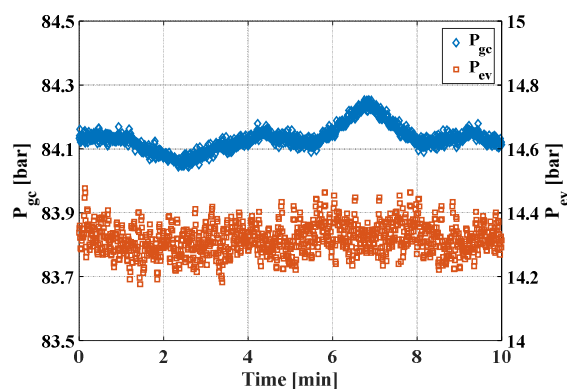


Figure 6. Gas cooler and evaporator pressures variations during the test.

2.3.3 Data reduction

The measured parameters are used to evaluate the following quantities. The point of state 6 in Figure 4 (the vapor port of the liquid separator) is in two-phase region. Hence, its specific enthalpy was evaluated by an energy balance on the control volume containing the IHE and the by-pass valve, expressed by the Eq. (2.4). An energy balance on the vapor/liquid separator (Eq. (2.5)) ensures that the separator accomplish the required conditions to stabilize the mass flow rates in the system.

$$h_6 = h_4 + h_1 - h_3 \quad (2.4)$$

$$(1 + \mu)h_5 = h_6 + \mu h_8 \quad (2.5)$$

The heating capacity \dot{Q}_{gc} (kW) and the primary mass flow rate \dot{m}_{pf} (kg s⁻¹) were evaluated as follows:

$$\dot{Q}_{gc} = \rho_w \dot{V}_w c_{p,w} (T_{w,out} - T_{w,in}) \quad (2.6)$$

$$\dot{m}_{pf} = \frac{\dot{Q}_{gc}}{h_{in,gc} - h_{out,gc}} \quad (2.7)$$

where \dot{V}_w is the water volumetric flow rate in m³ s⁻¹; ρ_w , $c_{p,w}$, $T_{w,out}$ and $T_{w,in}$ are the density (kg m⁻³), the specific heat at constant pressure (kJ kg⁻¹K⁻¹), the gas cooler outlet and inlet water temperatures (°C) respectively; $h_{in,gc}$ and $h_{out,gc}$ are the refrigerant gas cooler inlet and outlet enthalpy (kJ kg⁻¹), calculated via Refprop 9.1 [24].

In a preliminary set-up of the prototype a Coriolis mass flow meter has been introduced in order to measure the secondary flow; it was placed in the only position it does not affect the system performance, that is before the throttling valve. Anyway, instabilities of the measured signals occurred. The reason has not been determined precisely: it might be due to an error in the reading of the flow meter due to the presence of two-phase flow or to a dynamic instability of the flow due to the coupling of the secondary flow of the ejector with a too high pressure drop of the secondary circuit (a throttling valve instability is excluded since it was kept at a constant opening). To avoid a large alteration of the circuit of the heat pump and keep the circuit close to a heat pump ready for the market, the cooling capacity (kW) at the evaporator was evaluated by Eq. (2.8) by applying an energy balance on the

whole system: the heat losses were neglected, since all the components (included the compressor) can be reasonably considered adiabatic to the surroundings thanks to a hard-thermal insulation. The secondary mass flow rate was calculated by an energy balance on the evaporator, expressed by Eq. (2.9).

$$\dot{Q}_{ev} = \dot{Q}_{gc} - \dot{W}_{cp} \quad (2.8)$$

$$\dot{m}_{sf} = \frac{\dot{Q}_{ev}}{h_{out,ev} - h_{in,ev}} \quad (2.9)$$

Where, $h_{in,ev}$ and $h_{out,ev}$ are respectively the refrigerant evaporator inlet and outlet enthalpies (kJ kg^{-1}). The coefficient of performance was evaluated by Eq. (2.10). \dot{W}_{cp} is the electrical power required by the compressor (kW).

$$COP = \frac{\dot{Q}_{gc}}{\dot{W}_{cp}} \quad (2.10)$$

2.3.4 Uncertainty analysis

The instrumental B-type uncertainties are composed to the standard deviation evaluated in the recording time for all the measured parameters. The uncertainty analysis of the derived results is carried out by using the law of propagation of errors [25]. The uncertainty analysis is shown in Table 4. The results showed in this work are characterized by uncertainties lower than the following values: the primary mass flow rate can be measured within $\pm 6.7\%$, the secondary mass flow rate within $\pm 8.8\%$ (under the hypothesis of adiabaticity of the system to the surrounding), the entrainment ratio within $\pm 9.8\%$, the pressure lift ratio within $\pm 1.8\%$, the heating capacity within $\pm 3.9\%$ and the COP within $\pm 2.3\%$, given the listed accuracy of the various measurement instrumentations.

Table 4. Uncertainty analysis.

Heating capacity	$u_c(\dot{Q}_{gc}) = \sqrt{\left[\left(\frac{\partial \dot{Q}_{gc}}{\partial \rho_w} \right)^2 \cdot u_c^2(\rho_w) \right] + \left[\left(\frac{\partial \dot{Q}_{gc}}{\partial \dot{V}_w} \right)^2 \cdot u_c^2(\dot{V}_w) \right] + \left[\left(\frac{\partial \dot{Q}_{gc}}{\partial c_{p,w}} \right)^2 \cdot u_c^2(c_{p,w}) \right] + \left[\left(\frac{\partial \dot{Q}_{gc}}{\partial T_{w,out}} \right)^2 \cdot u_c^2(T_{w,out}) \right] + \left[\left(\frac{\partial \dot{Q}_{gc}}{\partial T_{w,in}} \right)^2 \cdot u_c^2(T_{w,in}) \right]}$
Primary mass flow rate	$u_c(\dot{m}_{pf}) = \sqrt{\left[\left(\frac{\partial \dot{m}_{pf}}{\partial \dot{Q}_{gc}} \right)^2 \cdot u_c^2(\dot{Q}_{gc}) \right] + \left[\left(\frac{\partial \dot{m}_{pf}}{\partial \Delta h_{gc}} \right)^2 \cdot u_c^2(\Delta h_{gc}) \right]}$
Secondary mass flow rate	$u_c(\dot{m}_{sf}) = \sqrt{\left[\left(\frac{\partial \dot{m}_{sf}}{\partial \dot{Q}_{ev}} \right)^2 \cdot u_c^2(\dot{Q}_{ev}) \right] + \left[\left(\frac{\partial \dot{m}_{sf}}{\partial \Delta h_{ev}} \right)^2 \cdot u_c^2(\Delta h_{ev}) \right]}$
Entrainment ratio	$u_c(\mu) = \sqrt{\left[\left(\frac{\partial \mu}{\partial \dot{m}_{pf}} \right)^2 \cdot u_c^2(\dot{m}_{pf}) \right] + \left[\left(\frac{\partial \mu}{\partial \dot{m}_{sf}} \right)^2 \cdot u_c^2(\dot{m}_{sf}) \right]}$
Pressure lift	$u_c(\Pi) = \sqrt{\left[\left(\frac{\partial \Pi}{\partial p_{out,ej}} \right)^2 \cdot u_c^2(p_{out,ej}) \right] + \left[\left(\frac{\partial \Pi}{\partial p_{in,sf}} \right)^2 \cdot u_c^2(p_{in,sf}) \right]}$
Heating COP	$u_c(COP) = \sqrt{\left[\left(\frac{\partial COP}{\partial \dot{Q}_{gc}} \right)^2 \cdot u_c^2(\dot{Q}_{gc}) \right] + \left[\left(\frac{\partial COP}{\partial \dot{W}_{cp}} \right)^2 \cdot u_c^2(\dot{W}_{cp}) \right]}$
Ejector efficiency	$u_c(\eta_{ej}) = \sqrt{\left[\left(\frac{\partial \eta_{ej}}{\partial \mu} \right)^2 \cdot u_c^2(\mu) \right] + \left[\left(\frac{\partial \eta_{ej}}{\partial h_B} \right)^2 \cdot u_c^2(h_B) \right] + \left[\left(\frac{\partial \eta_{ej}}{\partial h_{in,pf}} \right)^2 \cdot u_c^2(h_{in,pf}) \right] + \left[\left(\frac{\partial \eta_{ej}}{\partial h_D} \right)^2 \cdot u_c^2(h_D) \right] + \left[\left(\frac{\partial \eta_{ej}}{\partial h_{in,sf}} \right)^2 \cdot u_c^2(h_{in,sf}) \right]}$
Specific enthalpy	$u_c(h) = \left \left(\frac{\partial h}{\partial T} \right)_{p=\text{const}} \cdot u_c(T) + \left(\frac{\partial h}{\partial p} \right)_{T=\text{const}} \cdot u_c(p) \right $

2.3.5 Tests results

The system and multi-ejector performance were explored in a wide range of operation condition in terms of source temperatures and heat pump parameters setting carrying out 34 tests (the investigated conditions of each test are shown in Table 5). The ambient temperature ranging between -15°C and 12°C in order to investigate the effects of a wide range external conditions. In the following paragraphs, the influence of each parameter (ejector geometry, operation conditions and compressor frequency) on the system performance were studied.

Table 5. Investigated test conditions.

Test [#]	$T_{w,in}$ [$^{\circ}\text{C}$]	$T_{w,out}$ [$^{\circ}\text{C}$]	T_{amb} [$^{\circ}\text{C}$]	f [Hz]	Ejectors configuration
1	40	60	12	50	ej1 + ej3
2	40	60	12	50	ej2 + ej3
3	40	60	12	50	ej1 + ej2 + ej3
4	40	60	12	50	ej4
5	40	60	12	50	ej2 + ej4
6	40	60	12	50	ej1 + ej2 + ej4
7	40	60	12	50	ej3 + ej4
8	40	60	12	50	ej1 + ej3 + ej4
9	30	60	-15	50	ej3
10	30	60	-10	50	ej3
11	30	60	-5	50	ej3
12	30	60	0	50	ej3
13	30	60	7	50	ej3
15	40	60	-15	50	ej3
16	40	60	-7	50	ej3
17	40	60	0	50	ej3
18	40	60	7	50	ej3
19	30	60	-10	50	ej4
20	30	60	-5	50	ej4
21	30	60	0	50	ej4
22	30	60	4	50	ej4
23	40	60	-15	50	ej4
24	40	60	-7	50	ej4
25	40	60	0	50	ej4
26	40	60	7	50	ej4

Test [#]	$T_{w,in}$ [°C]	$T_{w,out}$ [°C]	T_{amb} [°C]	f [Hz]	Ejectors configuration
27	40	60	12	50	ej4
28	40	60	7	30	ej4
29	40	60	7	40	ej4
30	40	60	7	50	ej4
31	40	60	7	60	ej4
32	40	60	7	30	ej3
33	40	60	7	40	ej3
34	40	60	7	50	ej3

Influence of different multi-ejector configuration on system performance

At fixed operation conditions, the influence of the ejector internal geometry on the main thermodynamic and performance parameters of the heat pump system have been analysed. Tests with different combinations of active ejectors have been carried out (tests from 1 to 8 in Table 5). The internal geometry of the ejector was expressed as ratio between the effective cross section and the total cross section, evaluated at the motive nozzle throat. Table 6 shows the investigated area ratios.

Table 6. Investigated multi-ejector area ratios.

Ejectors [#]	A_{eff}/A_{tot} [%]
ej1 + ej3	33.1
ej2 + ej3	40.0
ej1 + ej2 + ej3	46.5
ej4	53.4
ej2 + ej4	66.9
ej1 + ej2 + ej4	73.4
ej3 + ej4	80.1
ej1 + ej3 + ej4	86.6

In Figure 7, the T - s and p - h diagrams are shown by considering tests characterized by a $T_{w,in}$ of 40 °C, a $T_{w,out}$ of 60 °C and a T_{amb} of 12 °C. The inverter of the compressor has been set to 50 Hz. Different overall cross section available to the primary mass flow rate in the motive nozzle ejector are considered by varying the active ejector configuration. The red, green and blue lines in Figure 7 correspond to an overall cross section of 33.1%, 53.4% and 86.6% respectively.

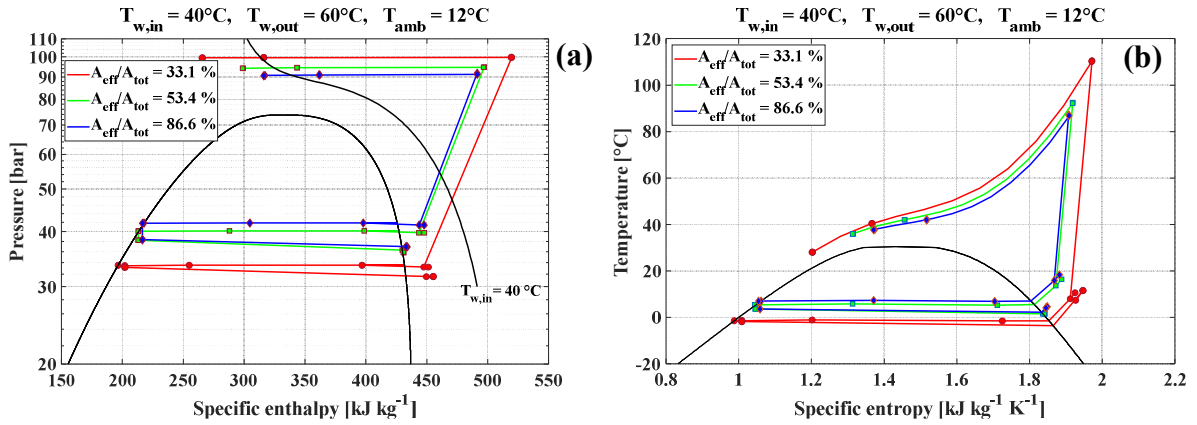


Figure 7. (a) p - h diagram and (b) T - s diagram, variation of the thermodynamic cycle varying the overall ejectors cross section.

The heating capacity and the electrical power required by the compressor as a function of the overall cross section available to the primary mass flow rate are shown in Figure 8a. The rapid increment of the primary mass flow rate with the increase of the throat section leads to the increases of the heating capacity, that reaches a maximum value and then sharply decreases. Instead, the compressor power decreases slightly. As consequence, there is an overall ejectors cross section which determines a maximum of the COP, with an increment equal to 13.8% with respect to the worst case, as shown in Figure 8b. The maximum value of the system performance is obtained for an ejectors cross section of 46.5% with respect to the overall ejectors cross section available, in the investigated conditions. The results are in line with the results shown by Liu et al. [26], which have experimentally studied the influence of the ejector internal geometry on the CO₂ heat pump performances. Their experimental results show that the heating capacity and the overall system COP reach a maximum in correspondence of the motive nozzle throat diameter of 2 mm.

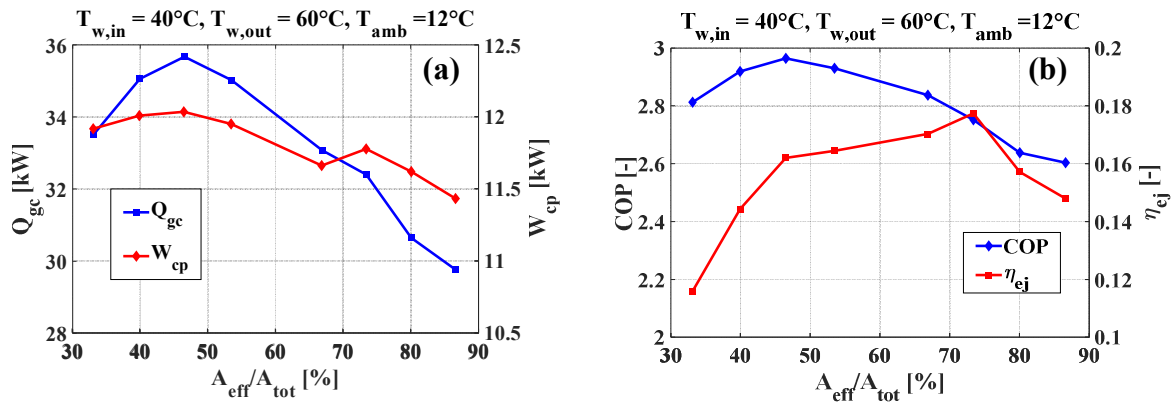


Figure 8. Performance variations as a function of the overall ejectors cross section. (a) Heating capacity (left) and compressor work (right); (b) COP (left) and ejector efficiency (right).

Influence of source and sink temperatures on system performance

In this section, tests were run in order to study the external source and sink temperatures influence on the system performance in terms of climatic chamber temperature, T_{amb} , and gas cooler inlet water temperature, $T_{w,in}$. In all tests, $T_{w,out}$ was set and kept constant at 60°C and the compressor frequency at 50 Hz, varying the T_{amb} in a range $-15^{\circ}\text{C} \div 12^{\circ}\text{C}$ (tests from 9 to 27 in Table 5). The ejectors n° 3 and n°4 were considered. The T_{amb} influence on the T - s and p - h diagrams are showed in Figure 9 at a $T_{w,in}$ of 40°C , a $T_{w,out}$ of 60°C and compressor frequency of 50 Hz. The red, green and blue lines in the figures correspond to an ambient temperature of -15°C , 0°C and 12°C respectively. The gas cooler pressure and the evaporator pressure increase as the ambient temperature increases (Figure 10). Instead, the pressure lift ratio decreases. This results in a higher intake pressure of the compressor and in a lower compressor ratio. Therefore, as the ambient temperature increases the primary mass flow rate increases.

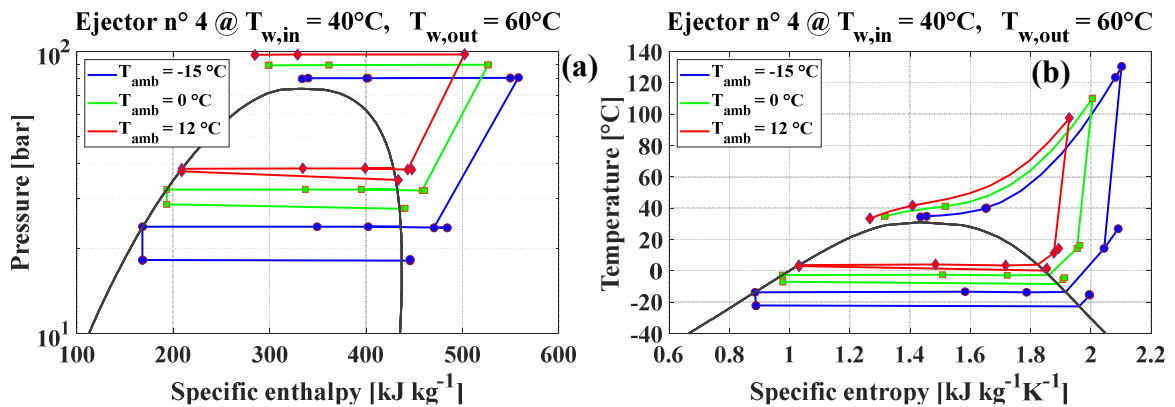


Figure 9. (a) p - h diagram and (b) T - s diagram, variation of the thermodynamic cycle varying the climatic chamber temperature.

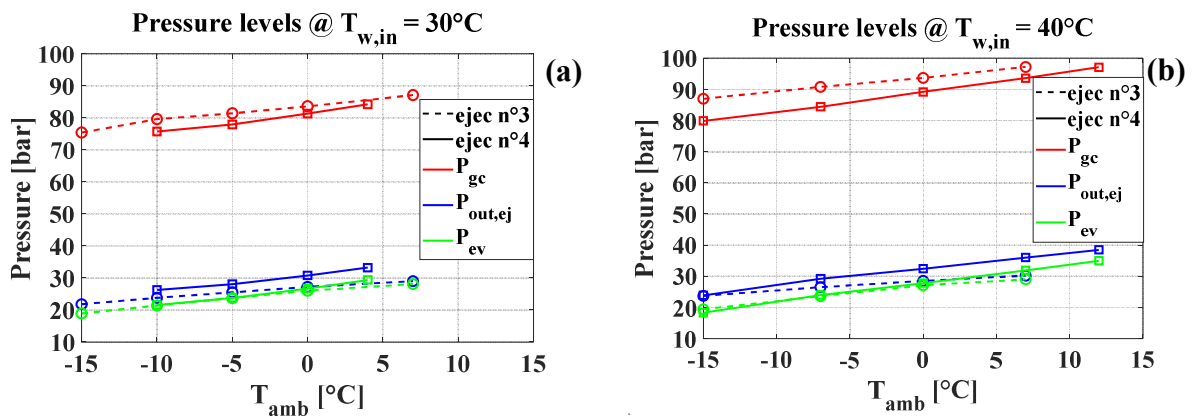


Figure 10. Pressure levels at (a) $T_{w,in} = 30^{\circ}\text{C}$ and (b) $T_{w,in} = 40^{\circ}\text{C}$ as a function of the climatic chamber temperature.

The enthalpy variation between inlet and outlet of the gas cooler and the compressor varies slightly. Consequently, the heating capacity increases with ambient temperature due to the increase of the primary mass flow rate. At the same time, the compressor work increases due to the higher mass flow rate. Also, higher compressor work results in higher water inlet temperature due to higher gas cooler pressure. Therefore, in terms of overall performance, the COP increases as T_{amb} increase and $T_{w,in}$ decreases, as shown in Figure 11. At $T_{w,in}$ of 40°C and ejector n°4 (the blue line in the figure), the heating COP increases from 1.48 to 2.93 as the ambient temperature increases from -15°C up to 12°C, with a percentage increment equal to 98%. Furthermore, in the investigated conditions, at fixed water inlet temperature it is possible to choose an ejector that allows better system performance. At $T_{w,in}$ of 40°C, ejector n°4 shows greater COP at ambient temperature higher than 4°C. At T_{amb} of 7°C, heating COP reaches value of 2.59 if the ejector n°3 is considered. At the same ambient temperature, with the ejector n°4, COP is 2.65. Differently, better performance is possible with the ejector n°3 for ambient temperature values lower than 4°C. At T_{amb} of -7°C, the COP assumes values of 2.14 and 1.88, corresponding to ejector n°3 and n°4 respectively, in the investigated conditions.

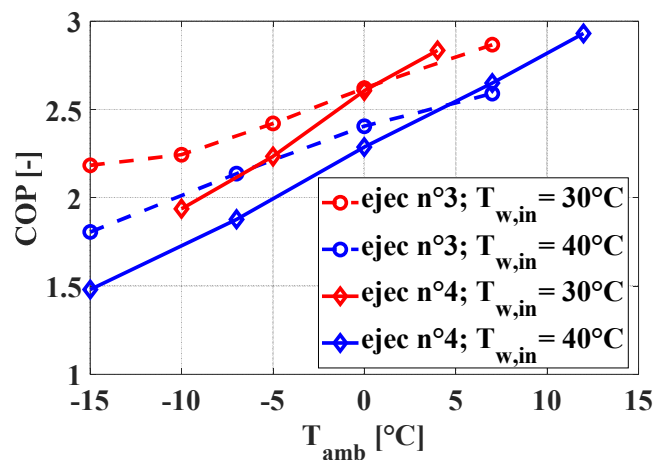


Figure 11. COP as a function of the climatic chamber temperature.

Influence of compressor frequency on system performance

In this section, the influence of the compressor volumetric capacity, controlled by the motor compressor frequency f , on the main thermodynamic and performance parameters of the heat pump system has been analysed. Tests characterized by $T_{w,in}$ of 40 °C, $T_{w,out}$ of 60 °C and T_{amb} of 7 °C have been considered. The tests have been run by varying

compressor frequency. If the ejector n°4 was considered, frequency values of 30 Hz, 40 Hz, 50 Hz and 60 Hz were investigated (tests from 28 to 31 in Table 4). Instead for the ejector n°3, the possible maximum frequency is 50 Hz due to the excessive value of the temperature at the compressor discharge (tests from 32 to 34 in Table 5). In Figure 12, the T - s and p - h diagrams are shown: the blue, green and red lines represent the thermodynamic cycles with compressor frequency equal to 30 Hz, 40 Hz and 60 Hz respectively, with ejector n°4.

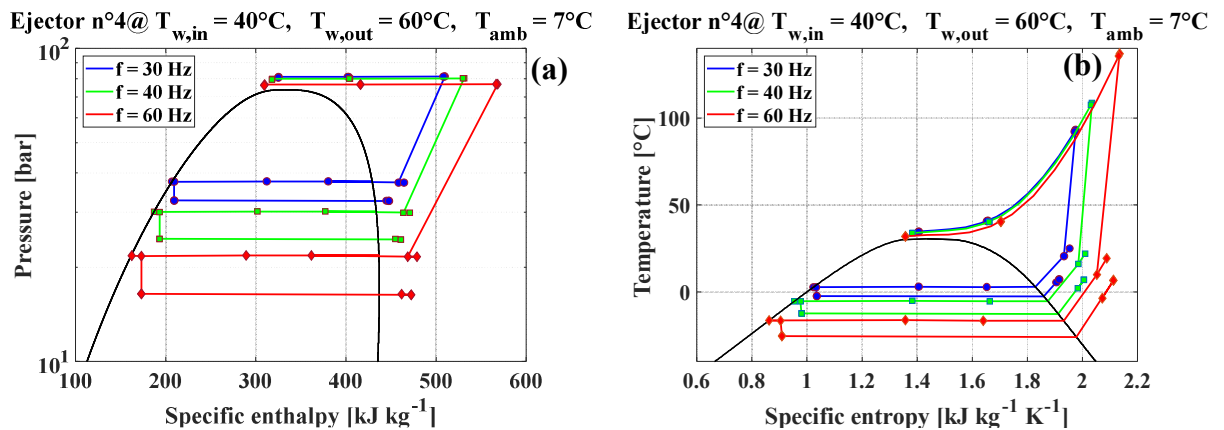


Figure 12. (a) p - h diagram and (b) T - s diagram, variation of the thermodynamic cycle varying the compressor frequency.

As the compressor frequency increases, the evaporator pressure decreases and the pressure lift ratio increases. Instead, the gas cooler pressure is not influenced by frequency: in these conditions, the gas cooler could have excessive dimensions (the refrigerant outlet gas cooler temperature is almost the same as the water inlet temperature). As the compressor frequency increases, the enthalpy variation at gas cooler and compressor increase. Therefore, the compressor power and the heating capacity increase. Combining the effects on the heating capacity and the compressor power, for the ejector n°4, the heating COP increases from 1.50 to 1.84 as the compressor frequency decreases from 60 Hz to 30 Hz, as shown in Figure 13, with a percentage increment of 22.7% (the lines in Figure 13 are only qualitative; the experimental data are only the points). The ejector n°3 shows the same trend: the heating COP assumes values of 2.10 and 1.65 that correspond to compressor frequency equal to 30 Hz and 50 Hz respectively, with a percentage increment of 27.3%. Figure 13 also shows the influence of the compressor frequency on the ejector efficiency: as the compressor frequency increases, ejector efficiency initially increases,

reaches a maximum value of 11% at compressor frequency of 50 Hz and then decreases, when the ejector n°4 was considered. Instead, ejector n°3 presents values of the efficiency higher than the ejector n°4, with a value of 20% at compressor frequency of 40 Hz. Furthermore, in these conditions, the maximum calculated ejector efficiency does not correspond to the maximum COP value due to the considerable increase of the compressor work with the increase of the compressor frequency.

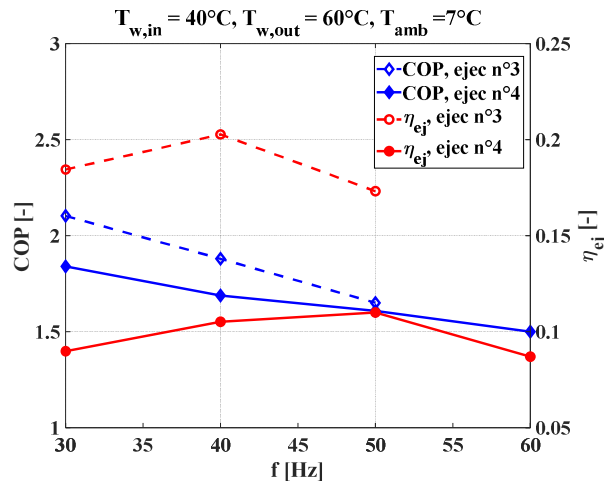


Figure 13. COP (left) and ejector efficiency (right) as a function of the compressor frequency.

2.4 Main outcomes of the chapter

In order to evaluate the actual performance of a CO₂ multi-ejector system in air conditioning applications, experimental tests on a complete heat pump system with multi-ejector pack and internal heat exchanger for space heating have been carried-out. The main outcomes of the research are listed as follow:

- The state of the art pointed-out that the use of an ejector system as expansion device in vapor compression cycles could lead to relevant increments of the system performance (up to 60% with respect to conventional vapor compression cycles) depending on operating conditions.
- The maximum value of the COP is equal to 2.93 and it was obtained when producing hot water at a temperature of 60 °C, starting from 40 °C, for an ambient temperature of 12 °C, at a compressor frequency of 50 Hz. The corresponding optimal multi-ejector throat section is 46.5% of the total cross

section compared. In these conditions, also the heat capacity assumes the maximum value.

- The system COP increases as the ambient temperature increases, at fixed water inlet temperature. Considering ejectors n°3 and n°4, the experimental results show a threshold value of the ambient temperature to switch from an ejector to another one in order to maximize the performance. In particular, at a water inlet temperature of 30 °C, ejector n° 4 shows higher COP than ejector n° 3 at ambient temperature higher than 0 °C. At a water inlet temperature of 40 °C and at ambient temperature of -7 °C, ejector n° 3 gives a heating COP of 2.14 with a percentage increment equal to 13.8% compared to ejector n° 4.
- Higher compressor frequency leads to a reduction of the COP due to the increase of the electric power required by the compressor. Furthermore, at high compressor frequency corresponds to higher cooling capacity, leading to an increase of thermal and internal inefficiencies (in the compressor and in the heat exchangers) due to the increase of the friction losses. Instead, an optimal value of the compressor frequency exists in order to maximize the ejector efficiency depending on the ejector geometry.

3 Prediction of primary mass flow rate for the ejector device in transcritical vapor compression cycles

An accurate design of the ejector could be useful to reduce the difference in terms of performance of the whole system varying the operating conditions. Also, a proper sizing of the ejector could lead the whole system to work with high performance at operating conditions different from the nominal ones. Due to this fact, in this chapter various two-phase ejector modeling procedures will be summarized, considering 0-D and 1-D models, predictive methods and CFD analysis. The data collected in the experimental campaign showed in the previous chapter will be used to compare the experimental data with semi-empirical correlation proposed by several authors for the motive mass flow rate prediction. Furthermore, a new semi-empirical model will be proposed.

3.1 State of the art

Various modeling procedures have been developed to predict the performance of two-phase ejectors. The simplest models are zero-dimensional models, which assign an efficiency and apply conservation equations to each of the components of the ejector (motive nozzle, suction nozzle, mixing section, and diffuser) to simulate performance. Zero-dimensional models nearly always assume homogeneous equilibrium flow. Zero-dimensional ejector models can generally be categorized by whether the mixing process is assumed to occur at constant pressure or through a constant cross-sectional area passage. Kornhauser [27] developed the first model of a two-phase ejector based on the assumption of constant pressure mixing, while Li and Groll [28] introduced a model of a two-phase ejector based on the assumption of constant area mixing. Detailed equation listings for the constant pressure mixing and constant area mixing ejector models can be found in these or other papers in the open literature. The majority of ejector cycle simulation papers have employed the zero-dimensional modeling approach described above.

The major drawback of this approach is the need to specify a proper value for the efficiency of each ejector component for each operating condition. The performance of the ejector is strongly dependent on the efficiency of its components, but these efficiencies are known to be highly dependent on geometry and operating conditions. Many studies in the literature have employed zero-dimensional ejector models without proper justification for the component efficiencies that were used and have assumed that the component

efficiencies remain constant as ejector operating conditions vary. Additionally, while zero-dimensional models do have limited ability to estimate certain flow cross-section areas, they do not have the ability to predict geometrical parameters that affect two-phase ejector performance. Furthermore, they are not able to predict local flow characteristics inside the ejector or accurately model the non-equilibrium expansion of two-phase fluid through the motive nozzle. Experimental validation of the individual ejector component efficiencies is a challenging task because most experimental setups do not allow to accurately measure all quantities needed. Among the most difficult issues to determine, there are the static pressure and the very high velocity at the outlet of the motive nozzle. Measurement of the mixing pressure is often difficult because of the pressure variations along the axial direction of the mixing section and the occurrence of complicated shock wave patterns that further complicate accurate measurements. Several recent papers have demonstrated simple methods to improve upon the accuracy of the zero-dimensional model while still retaining computational simplicity. To address the issue of how ejector component efficiencies vary with ejector geometry and operating conditions, Liu and Groll [29] developed empirical correlations based on their experimental data for the efficiencies of the motive nozzle, suction nozzle, and mixing section of a transcritical CO₂ ejector. The correlations were functions of the ratio of motive to suction pressure, ratio of nozzle throat to mixing diameter, and entrainment ratio. It should be noted that the motive nozzle of the ejector used to obtain the experimental data was a converging-only nozzle. The model used to simulate ejector performance was a constant area mixing model similar to that of Li and Groll [28] mentioned above; however, a significant improvement is offered by the formulation of Liu and Groll [29] because realistic values of component efficiencies can be applied over a wide range of operating conditions. Butrymowicz [30] was among the first to present experimental ejector data in the form of a two-phase ejector performance map. A performance map of an ejector calculates the overall performance of the ejector for the given operating conditions based on experimentally determined performance correlations.

Lucas et al. [31] also used the idea of a performance map for predicting the characteristics of an ejector. As described above, they developed an empirical correlation for ejector work recovery efficiency as a function of several ejector dimensions and operating conditions. The correlation was not a function of entrainment ratio, meaning that by specifying the ejector entrainment ratio and calculating ejector efficiency from the inlet states and necessary dimensions, the performance of the ejector could be fully specified.

Thus, with the required inputs, the efficiency correlation of Lucas et al. [31] can be used as a simple method to simulate the ejector performance based on experimental data.

Angielczyk et al. [32] proposed a new generalised procedure of the transonic trajectory determination that uses enhanced Possible-Impossible Flow algorithm. The procedure is much faster than the commonly used Newton Critical Point (NCP) approach. The approach was applied in modelling of carbon dioxide transonic two-phase flow through the convergent-divergent nozzle by means of Homogeneous Equilibrium Model (HEM) and Delayed Equilibrium Model (DEM). These models were used to simulate flows that were experimentally and theoretically investigated in literature.

Due to the above-mentioned limitations of zero-dimensional ejector modeling, one focus of ejector research for the past few years has been on developing CFD models capable of accounting for different ejector geometries and operating conditions as well as providing local flow characteristics throughout the ejector. The studies discussed below generally use commercial CFD software to model the turbulent mixing process between motive and suction streams, and in some cases, the models are able to account for the non-equilibrium flow in the nozzle and shock waves in the ejector.

Banasiak and Hafner (2011) [33] developed a one-dimensional model of a transcritical CO₂ ejector in which the flow path was discretized along the axial direction of the ejector and the flow was assumed uniform over a cross-section; the model considers ejector geometry, metastability effects, mixing of the two flows, and shock waves in the mixing section and diffuser. This model is able to predict motive flow rate and pressure lift to within 5%. The previous work was continued by Banasiak and Hafner (2013) [34] considering different phase change models in the motive nozzle. They compared the homogeneous equilibrium model (HEM) to the delayed equilibrium model (DEM) developing an empirical correlation to model the strength of heterogeneous nucleation.

Homogeneous relaxation model was used by Colarossi et al. (2012) [35] to develop a two-dimensional CFD model of a transcritical CO₂ ejector, taking into account non-equilibrium effects. The simulation results was compared to the experimental data of Nakagawa et al. (2011a) [18] founding that their model could match the data in term of pressure recovery to within 35%. Colarossi et al. (2012) [35] also found that the instantaneous quality was very close to the equilibrium quality throughout the nozzle, meaning that the expansion in the nozzle was nearly at thermodynamic equilibrium

according to their model; they concluded that the turbulence model and motive inlet condition have a more significant effect on the pressure recovery and accuracy of the ejector model than the relaxation model.

Yazdani et al. (2012) [36] developed a three-dimensional CFD model of a transcritical CO₂ ejector using boiling-controlled heat transfer and inertia-controlled cavitation models to predict phase change; they pointed-out that phase change is dominated by boiling near the center of the nozzle and by cavitation near the walls. The slip between phases has low impact on overall ejector performance but does produce a shock wave train at the exit of the motive nozzle. They used their model to show that reducing the mixing section diameter for the same nozzle diameter resulted in a reduction of the shock train amplitude at the outlet of the nozzle but a stronger shock wave downstream in the mixing section, resulting in lower overall pressure recovery with the ejector. Yazdani et al. (2014) [37] continued the study with a focus on the motive nozzle. They found that choking occurred in the nozzle downstream of the throat due to increasing velocity and decreasing speed of sound as liquid changes to vapor. Their model also showed that wider nozzle diverging angle results in more rapid phase change, choking closer to the nozzle throat, and flow behavior closer to equilibrium.

Smolka et al. (2013) [38] developed a three-dimensional CFD model of a transcritical CO₂ ejector but assumed homogeneous equilibrium flow throughout. They were able to predict experimental data for motive flow rates to within 14% and suction flow rates to within 20%, and pressure lift was also generally predicted accurately. They also accounted for the position of the suction inlet to the ejector and noted that doing so resulted in non-symmetric flow through the ejector mixing section and diffuser, meaning that depending on the particular ejector design, it may not be accurate to simplify the ejector model to axisymmetric geometry. Banasiak et al. (2014) [39] continued the study of Smolka et al. (2013) [38] by investigating the irreversibility of the flow at different locations in the ejector. Banasiak et al. (2014) [39] found that the greatest irreversibility was caused by the shock train at the nozzle outlet and turbulent mixing process in the mixing section, while the expansion in the motive nozzle generally accounted for only a small portion of the total irreversibility in the ejector. They also used their model to show that optimizing the geometry of one ejector section may not reduce overall ejector irreversibility but instead just shift it to another section of the ejector; this means that all ejector dimensions must be

considered simultaneously when optimizing ejector geometry. Palacz et al. (2015) [40] used a similar model to investigate the accuracy of the homogeneous equilibrium model over a larger range of conditions. They found that for operating conditions near or above the critical point, the model generally predicted motive mass flow rate to within 10% compared to the experimental data. However, for operating conditions at lower pressure or lower temperature, the accuracy of the model decreased.

Lucas et al. (2014) [41] also used a three-dimensional transcritical CO₂ ejector CFD model assuming homogeneous equilibrium flow throughout. They first compared their model results to experimental results for an ejector without suction flow and found that the model predicted motive flow rate and pressure rise to within 10%; an ejector with only motive flow still has frictional losses but does not have mixing losses. They then compared their model results to experimental results for the ejector with suction flow and found that the model only predicted pressure lift accurately to within 20% when suction flow was considered; this means that the model was not able to account for mixing losses as accurately as frictional losses.

It can be seen from the above studies that the most challenging aspect of developing an accurate CFD model of a two-phase ejector seems to be accurate modeling of the turbulent mixing process. Colarossi et al. (2012) [35] concluded that modeling of turbulence had a more significant effect on model accuracy than modeling of non-equilibrium motive flow expansion, while Lucas et al. (2014) [41] showed that losses caused by the mixing process were more difficult to predict than frictional losses. Additionally, the recent studies of Smolka et al, 2013 [38], Banasiak et al, 2014 [39], and Lucas et al. (2014) [41] all assumed homogenous equilibrium flow throughout the ejector and still achieved reasonable accuracy, which again indicates that accounting for non-equilibrium effects may not be as important as other aspects of the flow in the ejector. It should be noted, however, that the study of Palacz et al. (2015) [40] found the homogeneous equilibrium approach was less accurate at nozzle inlet conditions of lower pressure and lower temperature, meaning that for certain applications, such as refrigeration, a different approach may be necessary.

It should also be noted that many of the above studies do not always predict shockwaves in the ejector or do not validate the prediction of shockwaves. Shockwaves are known to occur in the mixing section and diffuser of two-phase CO₂ ejectors based on experimental observations and believed to occur at the outlet of the nozzle (shock train). A

shockwave is an irreversible process, meaning that it decreases the overall efficiency of an ejector compared to an isentropic pressure rise; this means that an accurate two-phase ejector model should be able to accurately predict location, shape, and strength of shockwaves. The difficulty in model prediction of shockwaves is in part due to the difficulty in determining shock structure experimentally, especially for the two-phase shock train at the outlet of the nozzle. The position and strength of shock waves are functions of the Mach number of the flow throughout the ejector. However, it is difficult to determine the Mach number for two-phase flow, as the speed of sound of a two-phase flow is highly dependent on the flow regime, and the flow regime throughout two-phase ejectors is generally not well known [42]. This adds further difficulty to obtain an accurate prediction of shockwaves in two-phase ejectors. It should be noted, however, that many of the above models have predicted the overall performance of the ejector accurately without necessarily predicting shockwaves accurately. Banasiak et al. (2015a) [42] provide a more detailed review of one- and multi-dimensional modeling of transcritical CO₂ ejectors. They also review several experimental studies that attempt to characterize the physics of the flow inside the ejector, noting that no study has successfully identified the two-phase flow patterns or velocity profiles inside the ejector. It is concluded in the study of Banasiak et al. (2015a) [42] that greater knowledge of the flow pattern in each ejector passage, turbulence modeling, shockwave shape and strength, metastability effects, and effect of lubricant in CO₂ ejectors is needed in order to improve the accuracy of multi-dimensional models. The objective of developing a multi-dimensional CFD model is not only to accurately predict ejector performance but also to aid in the design of a high-efficiency ejector. In order to be a useful tool for ejector design, the model should be able to accurately model ejector performance for all ejector geometries and operating conditions; however, the models presented here are generally adjusted to match a single set of data but have not necessarily been shown to be accurate when compared to data from multiple studies. Future studies will need to focus on developing CFD models that can accurately predict the performance of ejectors from multiple studies over a wide range of geometries and operating conditions. Additionally, all of the CFD ejector models that have been developed and discussed here have used CO₂ as the working fluid. It may be interesting to see in future studies if the models developed for transcritical CO₂ ejectors can be applied to subcritical ejectors with low-pressure refrigerants. However, regardless of the working fluid used, experimental validation of the complicated, turbulent two-phase flow inside the individual

components of an ejector still remains the major hurdle in the process of making multi-dimensional prediction tools more reliable and trustworthy. The obvious advantage of using a multi-dimensional CFD model as opposed to a zero-dimensional model of an ejector is that all ejector dimensions and operating conditions can be accounted for by an accurate CFD model; however, this comes at the cost of far greater computational requirements. The zero-dimensional modeling methods presented by Liu and Groll (2013) [29] and Lucas et al. (2013) [31] provide interesting opportunities to accurately account for different operating conditions and ejector geometries without requiring the computational complexity of multi-dimensional CFD models. Expanding the procedures of these studies to account for additional ejector dimensions and wider ranges of operating conditions could be a focus of future studies and may allow zero-dimensional modeling to be of similar accuracy and applicability as multi-dimensional CFD modeling.

3.2 Objectives of the research

The experimental data proposed in the previous chapter and obtained with the test facility presented in section 2.3 have been also used to evaluate the mass flow rate through ejectors by using semi-empirical correlations provided by the current literature. Besides, a new semi-empirical correlation was developed and evaluated by means of a comparison between the literature correlations and the experimental data. Finally, an original correlation is proposed, based on the hypotheses of isentropic and choked two-phase flow.

3.3 Experimental results: primary mass flow rate and ejector parameters

The multi-ejector pack performance was explored in a wide range of operating condition: at fixed operating conditions, the influence of the ejector internal geometry on the ejector performance parameters has been analysed. Tests with different combinations of active ejectors have been carried out (tests from 1 to 8 in Table 5 of the previous chapter). During the tests, the operating conditions were kept constant. The ejector internal geometry was expressed as ratio between the effective cross section and the total cross section, evaluated at the motive nozzle throat. Table 6 of the previous chapter shows the investigated area ratios. Increasing the ejector cross section, the gas cooler pressure decreases and the evaporator pressure increases as well as the pressure lift ratio. Moreover, the enthalpy variation between inlet and outlet of the gas cooler and the compressor decreases. As a consequence, the primary mass flow rate increases due to higher intake

pressure and lower compression ratio, with a percentage increment equal to 39.3% (for an area percentage increment equal to 161.8%), as shown in Figure 14a. A more detailed analysis on the ejector parameters is showed in Figure 14b: the entrainment ratio decreases from 0.51 to 0.37 as the overall cross section increases, with a percentage variation of -26.9%. Instead, the pressure lift ratio increases from 1.06 to 1.13 with a percentage increment equal to 6.6%. This result is consistent with the experimental results shown in [20]: lower values of the entrainment ratio correspond to higher pressure lift ratios and vice versa. Figure 15 shows the influence of the ejector internal geometry on the ejector efficiency at the investigated operation conditions. The ejector efficiency reaches a maximum value equal to 17.7% at an overall cross section of 73.4%. The optimal ejector configuration that maximizes the heating COP system does not correspond to the ejector configuration that maximizes ejector efficiency.

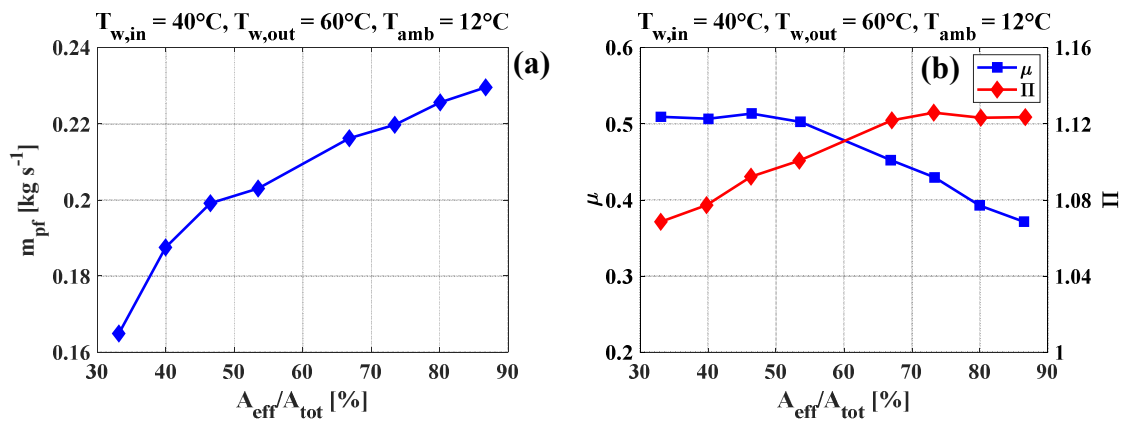


Figure 14. Performance variations as a function of the overall ejectors cross section. (a) Primary mass flow rate; (b) entrainment ratio (left) and pressure lift ratio (right).

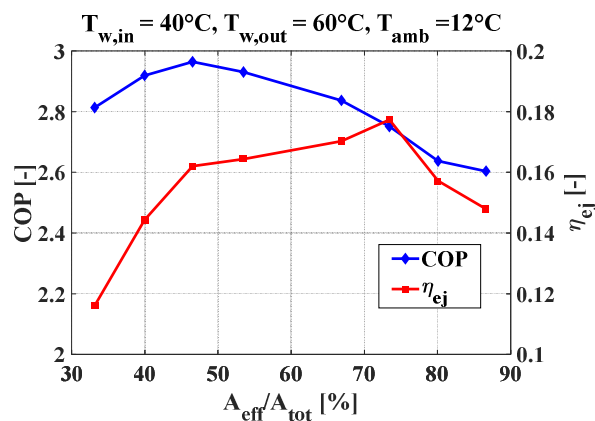


Figure 15. Performance variations as a function of the overall ejectors cross section. COP (left) and ejector efficiency (right).

3.4 Experimental investigation on predictive models for motive flow

In a CO₂ heat pump, the ejectors typically operate with inlet pressures higher than critical value (73.77 bar); moreover, the outlet pressures depend on the evaporator pressure and are usually lower than 40 bar. In this situation, it is reasonable to suppose that the motive flow is choked, as reported by Lucas et al. [31] and Martin et al. [43]; consequently, the ejector throat pressure is equal to the sonic (choked) flow conditions and the mass flow rate only depends on the input conditions. The accurate prediction of the two-phase mass flow rate in sonic condition is very difficult due to incomplete knowledge of the complex thermal-fluid dynamic phenomena that occur between the two phases. In particular, the sound velocity in two-phase flow can change quickly with the vapor quality [44]. Its calculation is still a matter of discussion M.-S. Chung et al. [45]. Moreover, specific behaviors, issues as metastable conditions and large slip ratio should be taken into account. The equation for calculating the dischargeable mass flow rate \dot{m} through a throttling device having a geometric seat area A is usually defined as:

$$\dot{m} = k_d G_t A \quad (3.1)$$

where G_t is the theoretical mass flux in an ideal (isentropic) nozzle and k_d is the two-phase discharge coefficient. Reliable methods for the calculation of mass flow rate when the inlet conditions are supercritical are not available in the literature. This essentially depends on the fact that the available methods use physical quantities related to the vapor state, which are not present in supercritical conditions; e.g., the ISO method [46], derived from the previous HEM [47], [48] method, is not recommended when the input pressure is greater than 50% of the critical thermodynamic pressure of the fluid. In the open literature there are only a few semiempirical correlations based on experimental data to calculate the mass flow rate for CO₂ in supercritical inlet conditions. Lucas et al. [31] propose a method based on the data of an experimental campaign on a multi-ejector heat pump using carbon dioxide as refrigerant. Lucas method assumes that the expansion in the converging driving nozzle is isentropic and, consequently, the driving mass flow rate can be calculated by the following equations:

$$u_{th} = \sqrt{2(h_{in} - h_{th})} \quad (3.2)$$

$$\dot{m}_{in} = A_{in} \rho_{in} u_{th} \quad (3.3)$$

The density and the enthalpy at the throat can be estimated knowing the throat entropy (equal to the inlet entropy for isentropic flow) and the pressure at the throat. Correlating experimental data with eq. (3.2) and (3.3) with an iterative method, Lucas suggests calculating the ratio η_c between the throat pressure and the inlet pressure with the next equation:

$$\eta_c = \frac{p_{th}}{p_{in}} = 0.0871942 \left(\frac{p_{in}}{p_{cr}} \right)^{0.9519907} \left(\frac{\rho_{in}}{\rho_{cr}} \right)^{2.348013} + 0.39387 \quad (3.4)$$

For the kind of data set used by Lucas (e.g. inlet pressure supercritical, evaporation pressure lower than 40 bar, inlet temperature equal or higher than the CO₂ critical temperature (30.98 °C)), p_{th} corresponds to the choked pressure [43].

Banasiak et al [49] investigated the performance of a multi-ejector for R744 vapor compression units too; they proposed the following correlation for calculation of mass flow rate

$$\dot{m} = \frac{\pi}{4} d_{th}^2 \left[A \rho_{in}^2 + B \rho_{in} + C \left(\frac{p_{in}}{p_{cr}} \right)^2 + D \frac{p_{in}}{p_{cr}} + E \right] \quad (3.5)$$

where A, B, C, D, E are coefficients adjusted according to the specific ejector geometry. For example, for a $d_{th} = 0.7$ mm, these coefficients are [49]: A=1.71938 10⁻¹ m⁴ kg⁻¹ s⁻¹, B = -6.06326 10¹ m s⁻¹, C= 4.55787 10³ kg m⁻² s⁻¹, D= 4.98027 10⁴ m⁻² kg s⁻¹, and E= -5.46798 10⁴ m⁻² kg s⁻¹.

Martin et al. [43] conducted an experimental investigation on short tube orifices used as expansion devices in CO₂ refrigerant systems; they suggested a model with dimensionless numbers:

$$\dot{m} = d^2 \sqrt{\rho_{in} p_{in}} \left[A \left(\frac{L}{d} \right)^B \left(\frac{p_{in}}{p_{cr}} \right)^C \left(\frac{T_{in}}{T_{cr}} \right)^D \left(\frac{d}{d_{ch}} \right)^E \right] \quad (3.6)$$

where A, B, C, D, E are parameters optimized to reach a minimal deviation between measurement and calculation. In the article the values of the coefficients obtained from experimental tests for a short tube are reported, with $d=1$ mm and $L=20$ mm: A= 0.41, B=-0.015, C=0.9, D=-5, E=0.36.

The aim of this analysis is to find a new semi-empirical correlation to obtain better mass flow rate predictions, using the experimental data available. In particular, in addition to dimensionless parameters already used in the previous correlations, a new geometric parameter was introduced to take into account the ejector geometries.

$$\dot{m} = kd^2 \frac{\pi}{4} \left[A \left(\frac{p_{in}}{p_{cr}} \right)^B \left(\frac{T_{in}}{T_{cr}} \right)^C \left(\frac{\rho_{in}}{\rho_{cr}} \right)^D \left(\frac{L}{d} \right)^E + F \right] \quad (3.7)$$

A, B, C, D, E and F are calculated by a mathematical solver that reach the minimum MSE value and $k=10^5$ is a constant used to optimize the solver process. Another correlation is proposed, considering that the saturation pressure, calculated with the isentropic expansion hypothesis from the input conditions, could be an indicator of the ejector output conditions. In fact:

- during the expansion at pressures lower than 40 bar in the convergent of the motive nozzle, saturation conditions are often reached [43];
- it can be assumed that, in these situations, the sonic velocity is reached at low vapor quality [45];
- the flow through orifices and nozzles can be assumed isentropic.

The pressure thus calculated, called p_{ise} and defined as the critical pressure corresponding to the choked flow, has been correlated to the measured flow rate; the investigations have allowed the identification of a simple correlation expressing the mass flow rate as function of the parameter $\eta_{ise}=p_{ise}/p_{in}$ and the ejector diameter d_{ej} :

$$\dot{m} = d_{ej}^2 \frac{\pi}{4} [a + b\eta_{ise}] \quad (3.8)$$

Where a and b are function of d_{ej} and are determined by experimental data.

$$a = (A + Bd_{ej} + Cd_{ej}^2) \quad (3.9)$$

$$b = (D + Ed_{ej} + Fd_{ej}^2) \quad (3.10)$$

3.4.1 Results and discussion

Table 7 shows the motive nozzle throat section diameters and the available experimental data subdivided by the inlet temperature range. All tests are with inlet

pressure higher than critical. The outlet pressures are between 20÷40 bar for all the tests and they are determined by typical operating conditions of heat pumps in heating applications. Figure 16 shows the tests input conditions in the T - s diagram. Most of the ejector 4 tests have $T > T_{cr}$, while the ejectors 2 and 3 tests are almost all with $T < T_{cr}$.

Table 7. Motive nozzle throat sections diameters and experimental test distribution.

Ejector [#]	Nozzle throat diameter [mm]	Test		TOT
		$T_{in} < T_{cr}$	$T_{in} > T_{cr}$	
1	0.7	-	-	-
2	1.0	18	0	18
3	1.4	15	4	19
4	2.0	7	12	19

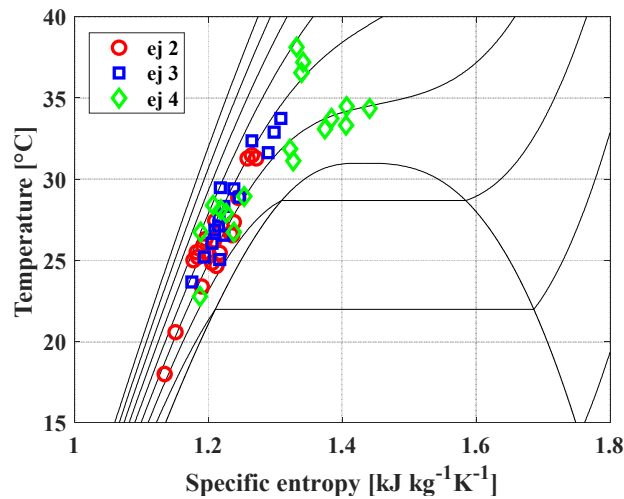


Figure 16. Test input conditions for the three ejectors in the T - s diagram.

The mass flow rate calculated applying correlation of Lucas (3.2), (3.3), (3.4) with the coefficients proposed in [20] for p_{th} calculation and showed in Figure 17a, are affected by high errors ($MSE = 37.5 \cdot 10^{-5}$). Using the solver to optimize coefficients of (3.4) with respect to experimental data, predictions are improving, but maintaining a high value of $MSE = 21.18 \cdot 10^{-5}$. The recalculated coefficients in (3.4) are: 0.86535, -0.50933, -0.26973 and the constant term is 0. Figure 17b shows mass flow rate percentual errors as a function of the ejector pressure inlet p_{in} : predictions are almost always underestimated, but for ejector 4 are closest to the optimal values in comparison with the predictions for the other ejectors.

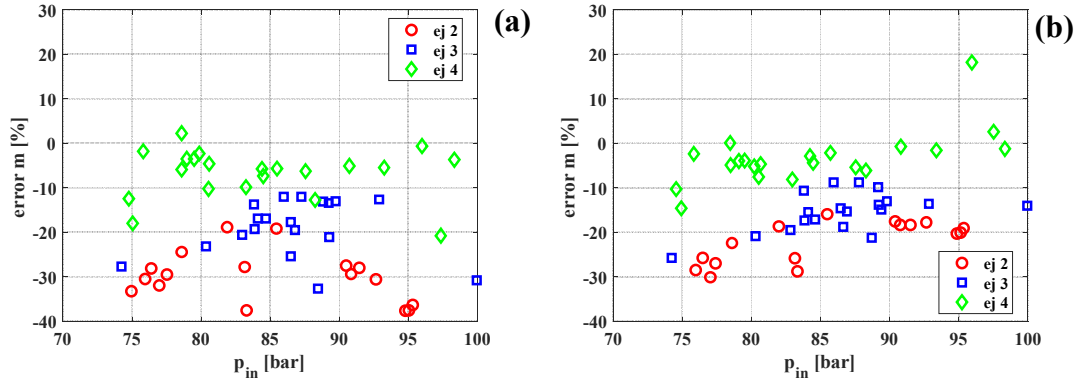


Figure 17. Percentage error in mass flow rate calculation using Lucas correlation (3.2), (3.3), (3.4): (a) original version; (b) coefficient recalculated by solver.

Figure 18a depicts the percentage errors for Banasiak correlation (3.5) optimized with new experimental data ($A=0.07561 \text{ m}^4 \text{ kg}^{-1} \text{ s}^{-1}$, $B=30.66 \text{ m s}^{-1}$, $C=-3468.23 \text{ kg m}^{-2}\text{s}^{-1}$, $D=47016.37 \text{ m}^{-2}\text{kg s}^{-1}$, $E=-53737.9 \text{ m}^{-2}\text{kg s}^{-1}$); MSE improves to $13.11 \cdot 10^{-5}$ and error values are between -20 and 20%. The three ejector predictions are almost parallels and errors increase by passing from ejector 2 to ejector 4, remarking an uncaptured effect of the size of the system in this type of correlation. To understand these results we would like to point out that, in the spirit of this study, we have tried to use this correlation for the three ejectors simultaneously while the author has suggested that the coefficients for each geometry should be defined. Indeed, using the correlation individually for each ejector, as indicated by Banasiak, the obtained MSE for ejectors 2 and 3 are good, about 2 and $4 \cdot 10^{-6}$ respectively, and the calculated coefficients are close together. Instead, prediction for ejector 4 showed a relatively high MSE, $9.8 \cdot 10^{-5}$ and very different coefficients.

In the correlation of Martin (3.6), developed for short tubes, there are two terms related to geometry. To fit the ejector geometry, the term d/d_{ch} , related to E coefficient, was excluded and the other, L/d , was calculated by setting L =nozzle length and d =average nozzle diameter. Correlation of Martin predictions are good with $\text{MSE} = 4.83 \cdot 10^{-5}$ with $A=1.04901$, $B=0.72643$, $C=1.50484$, $D=-1.11549$; E was not calculated. Almost all errors are between -10 and 10% and there are no particular differences for the three ejectors as shown in Figure 18b.

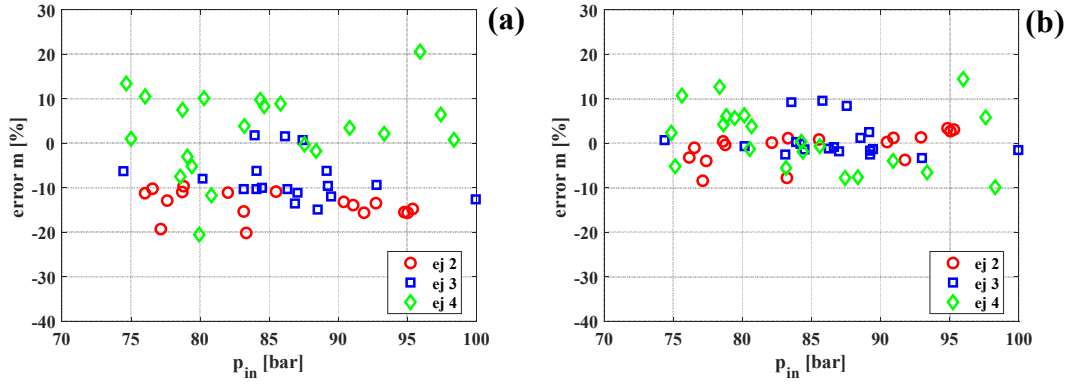


Figure 18. Percentage error in mass flow rate calculation with coefficient recalculated by solver: (a) Banasiak correlation (3.5); (b) Martin correlation (3.6).

Figure 19a depicts the predictions of the new correlation (3.7) where the parameter L/d is the same introduced for correlation of Martin and coefficient are: $A=2.7415$, $B=0.4084$, $C=0.0590$, $D=0.05048$, $E=-0.2360$ and $F=-2.3640$. MSE value is $4.08 \cdot 10^{-5}$ and most errors are between -7% and 6% and do not seem to be particularly affected by the ejector geometry. Figure 19b shows the relationship between the specific mass flow rate G and the parameter η_{ise} for the three ejectors with the relative linear fit function. By interpolating the terms of the three linear functions, we obtained the coefficients $A=-60017$, $B=329680$, $C=-112530$, $D=203090$, $E=-473400$, $F=155440$ to be inserted into (3.9) and (3.10) to complete the correlation (3.8), that expresses the flow rate according to the η_{ise} and the ejector diameters. Figure 20a depicts the G errors of this method as function of p_{in} for the three ejectors. The $MSE=4.02 \cdot 10^{-5}$ is almost equal to that of the previous correlation. Most of the errors are between -5% and 11% and do not seem to be particularly affected by the ejector geometry.

With reference to Eq. (3.1), calculations have shown how correlations without a parameter related to ejector geometry have worse predictions. The correlations analysed, except for (3.8), use the transcritical conditions (p_{cr} , ρ_{cr} , T_{cr}) to look for representative parameters of the mass flow rate or to compute η_c (3.4). Also, the reliability of calculation method (3.8) depends on input conditions because they may affect the validity of its initial hypotheses. In these situations, different input conditions, even considering that expansion is exiting from the transcritical zone, may be a reason for the different reliability of correlations.

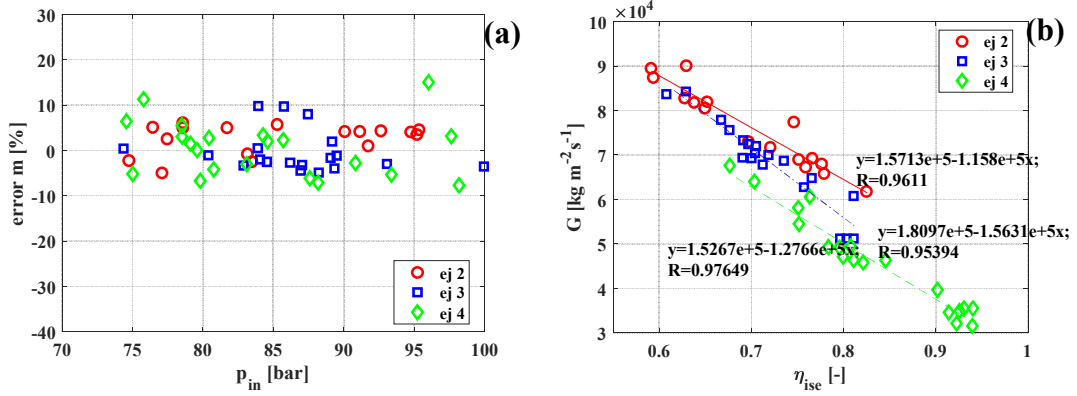


Figure 19. Percentage error in mass flow rate calculation: (a) new correlation (3.6) with coefficient calculated by solvers; (b) specific mass flow rate as function of the parameter η_{ise} .

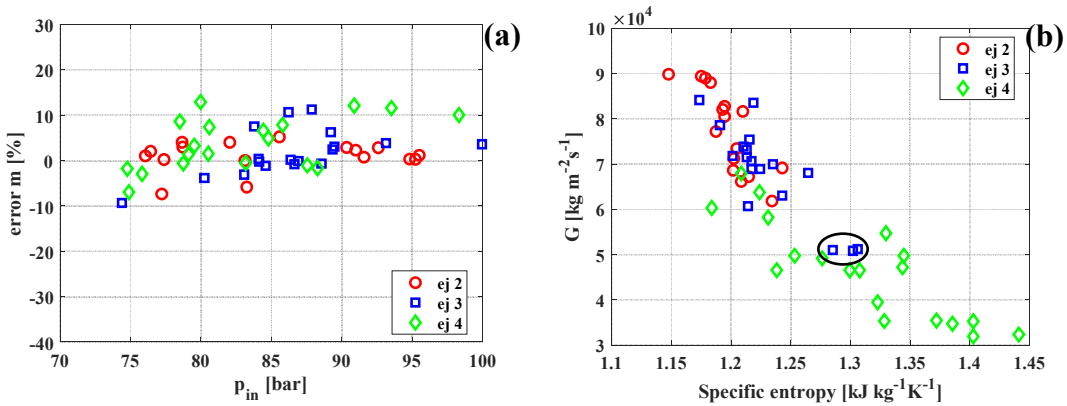


Figure 20. Percentage error in mass flow rate calculation: (a) new method with coefficient calculated by solvers; (b) specific mass flow rate as function of entropy at ejector inlet.

By going to check the test input conditions (Figure 16 and Figure 20b) it is noticed that almost all the tests performed with the ejector 4 were characterized by different values of some physical inlet quantities compared to the other ejectors; most of experimental points relative to ejectors 2 and 3 are almost in the same range of entropy ($1.16 \div 1.28 \text{ kJ kg}^{-1} \text{K}^{-1}$) and temperature ($23 \div 32 \text{ }^\circ\text{C}$) while tests of ejector 4 have $s_{in} = 1.2 \div 1.43 \text{ kJ kg}^{-1} \text{K}^{-1}$ and $T_{in} = 23 \div 43 \text{ }^\circ\text{C}$. This could be explained with these considerations:

- the correlation (3.5), used individually for each ejector, has good predictions for ejectors 2 and 3 and the calculated coefficients are close together while its reliability is much worse for ejector 4.
- the three tests circled in the Figure 20b, have worse predictions for that geometry (ejector 3) with every correlation.

3.5 Main outcomes of the chapter

The experimental data related to a transcritical ejector using carbon dioxide was compared to motive mass flow rate prediction methods. Also, a new semi-empirical correlation was obtained. The main outcomes are summarized as follow:

- According to the analysis of the state of the art, various methods and modeling to estimate the two-phase ejector performance exist. The easier approach consists in 0-D model which considers constant ejector sections efficiencies. Meanwhile, models CFD based are able to take into account the influence of operating conditions and ejector geometry on ejector sections efficiencies as well as local flow characteristics. The main drawback is related to the uncertainty in the evaluation of the speed sound in a two-phase flow.
- The experimental results showed that the primary mass flow rate increases with the ratio between the effective cross section and the total cross section of the multi-ejector pack. The same trend was found for the pressure lift; the entrainment ratio assumes the opposite trend.
- Among the investigated predictive methods, the correlation proposed by Lucas (equations (3.2), (3.3), (3.4)) predicts the experimental data with a MSE of $37.5 \cdot 10^{-5}$. The constant of each method are recalculated by using the experimental data: in this case, the correlation of Martin (3.6) gives the best fitting with a MSE of $4.83 \cdot 10^{-5}$.
- A semi empirical correlation for the primary mass flow rate evaluation was proposed. Although the correlation coefficient was calibrated as function of the ejector geometry, the errors in the evaluation of the mass flow rate are ranging between -5% and 11% similar to the existing methods.

4 Heat driven ejector systems: thermo-economic analysis and two-phase heat transfer

This chapter is focused on the use of three thermal source cooling systems in which the thermodynamic cycle can be powered by using waste heat or renewable sources. In this technical solution, the ejector works with motive and secondary flow both in saturated or superheated vapor condition, with remarkable simplification in the ejector modelling. The aim of this chapter consists to place the waste heat recovery hybrid ejector cycle (WHRHEC) in the actual cost/performance scenario, comparing the ejector technology to the conventional heat driven cooling systems, such as absorption and combined Organic Rankine Cycle/Vapor Compression Cycle, for which the corresponding state of the art are proposed. Furthermore, a thermo-economic analysis is proposed to investigate the possible economic convenience in the use of a WHRHEC with respect to a conventional vapor compression cycle. Finally, an experimental activity focused on the flow boiling of refrigerants at high saturation temperature is described, in order to collect two-phase heat transfer experimental data that are lacking in the current literature.

4.1 Heat driven systems state of the art

4.1.1 Absorption systems

Absorption systems can be used to produce the cooling effect and take advantage of waste heat from industrial large-scale processes. Within this technology, single effect chillers using LiBr-Water as working pair represent a solid and commercially developed solution. Henning [50] gave an overview of solar assisted air conditioning systems for the buildings, highlighting that the 59% of the cooling systems in Europe using solar collectors for air conditioning are absorption systems. Market available absorption cooling technologies can span from 50 to 200 kW with COP values in the range 0.3 to 1.2, as reported by Baniyounes et al. [51]. When single effect systems are considered, the coefficient of performance is ranging between 0.3 and 0.8 with heat source temperatures varying between 80°C and 120°C. Higher COP values (up to 1.3) can be obtained using double effect systems and higher heat source temperatures (up to 180 °C). Guido et al. [52] showed the performance on field of 27 small and medium scale absorption systems (30-160 kW cooling load) equipped with a control algorithm able to optimize the system performance. In most of the investigated conditions, they obtained COP values ranging

between 0.7 and 0.8. Typical COP values in this case might reach 0.6-0.8 (up to 0.9-1.3 in case of double effect systems) after a careful optimization of the entire system for big size plants for the air-conditioning sector [53]. For the industrial field, absorption systems using Water/Ammonia as working pair can be considered, although in this case lower COP are expected (0.25-0.5) [53]. However, these cooling systems have some drawbacks: LiBr-Water absorption chillers give low performances when the generation temperature is lower than 90°C, although these systems in the most of the case is not able to operate at generation temperature lower than 80°C due to the vanishing of the concentration difference between strong and weak solutions. Moreover, serious corrosion problems occur at generation temperatures higher than 200 °C, as reported by Hassan and Mohamad [54]. In addition, single-effect and double-effect H₂O-LiBr cooling cycles cannot operate at heat condensation temperatures of 50 °C due to the crystallization limit at low water concentrations [55]. Furthermore, the cooling temperature should reach 5°C at high condensing temperatures due to the risk of crystallization of the working fluid [56].

4.1.2 Combined ORC/VCC systems

A heat driven feasible alternatives to the absorption chillers is represented by thermo-mechanical cooling systems in which the waste heat is converted into mechanical work by an Organic Rankine Cycle (ORC) coupled with a Vapor Compression Cycle (VCC). These systems have received a growing interest due to their advantages, since they carry beneficial effects by converting waste heat or heat from renewable sources into electricity enabling a better use of primary energy for cold production. The work of Aphornratana and Sriveerakul [57] presented a theoretical analysis of a heat-powered combined Organic Rankine Cycle coupled with a Vapor Compression refrigeration cycle. The combined system is able to work when supplied by low grade thermal energy at 60 °C, producing cooling temperature as low as -10 °C. The authors analysed the effects of the operating temperatures on the combined system performance, varying the generator temperature between 60 and 90 °C, the condenser temperature between 30 and 50 °C, and the evaporator temperature between -10 and 10 °C. COP values between 0.1 and 0.6 was found.

Nasir and Kim [58] studied the influence of different combinations of working fluids in the Organic Rankine Cycle (ORC) powered Vapor Compression Cycle (VCC), for domestic air conditioning. Seven working fluids (R245fa, R123, R134a, R1234yf, R1234ze (E), Butane and Isobutane) were considered and a total of forty-nine candidates were

analysed. The results showed that Isobutane gave the best performance in the standalone VCC meanwhile R134a was found to be the best candidate for the ORC by considering the system thermal efficiency, cycle pressure ratios, mass flow rates and expander outlet volumetric flow rates as evaluation criteria. Furthermore, R134a for the power sub-cycle and Isobutane for VCC was the best combination. By optimizing the system parameters, such as condenser temperature and subcooling for the VCC cycle and ORC condenser pressure, the authors found a maximum COP of 0.219, with dry air at the VCC evaporator inlet and 0.281, with 50% relative humidity air at the VCC evaporator inlet.

Wang et al. [59] developed a system using waste heat from stationary and mobile engine cycles to generate cooling for building and vehicles air conditioning. The power subsystem is a standard Organic Rankine Cycle with internal heat exchanger using R245fa as working fluid; a waste heat at temperature near 200 °C was obtained by using a hot oil loop. The cooling side is a standard vapor compression cycle with 5 kW of cooling capacity. Instead of using an electrical motor to drive the compressor, it was directly coupled to the expander. The working fluid R134a was used as the refrigerant. In order to maintain high system performance while reducing size and weight for portable applications, microchannel based heat transfer components and scroll based expansion and compression were used. Although the system was tested off of its design point, it performed well achieving 4.4 kW of cooling load at a measured heat activated COP of 0.48. Wang et al. [60] presented a systematic design study in order to investigate the effects of various cycle configurations of a combined cycle couples an ORC (organic Rankine cycle) and a VCC (vapor compression cycle) on the overall COP. With both subcooling and cooling recovery in the vapor compression cycle, the overall cycle COP reached 0.66 at extreme military conditions with outdoor temperature of 48.9 °C. A parametric trade-off study was conducted afterwards in terms of performance and weight, in order to find the most critical design parameters for the cycle configuration with both subcooling and cooling recovery. Five most important design parameters were selected, including expander isentropic efficiency, condensing and evaporating temperatures, pump/boiling pressure and internal heat exchanger effectiveness. Among the considered parameters, the increasing of the expander isentropic efficiency shows the most positive outcomes on the system performance.

Due to the recent regulations related environmental aspects [9], working fluids such as R134a not be considered as potential candidate for these systems. Several authors investigated the use of eco-friendly working fluids. Li et al. [61] investigated the use of natural fluids (hydrocarbons) as alternative refrigerants to the conventional ones (HFC). In this paper, the hydrocarbons including propane, butane, isobutane and propylene as working fluids used in an organic Rankine cycle powered by a vapor compression cycle (ORC/VCC) system are analyzed and evaluated. With the overall COP and working fluid mass flow rate per kW of cooling capacity as key performance indicators, the results indicate that butane is the best refrigerant for the ORC/VCC system as the boiler exit temperature is between 60 and 90 °C, the condensation temperature varies from 30 to 55 °C and the evaporation temperature ranges from -15 to 15 °C. When the boiler exit temperature reaches 90 °C and the other input parameters are in typical values, the overall COP of the butane case reaches 0.470. Molés et al. [62] theoretically studied a combined organic Rankine cycle and vapor compression cycle system activated by low temperature heat sources. Two low GWP refrigerants were considered as working fluids for the VCC and two different low GWP fluids for the ORC. The influence of different operating conditions on the system performance was investigated through computational modeling. The system performance was evaluated for four different combinations of working fluids in the ORC (R1336mzz(Z) or R1233zd(E)) and in the VCC (R1234yf or R1234ze(E)). The results showed that the thermal COP of the ORC/VCC system varied between 0.30 and 1.10 over the range of operating conditions studied; it increased with the ORC and VCC evaporating temperatures and the ORC/VCC internal heat exchanger effectiveness and decreased with the condensing temperature. Furthermore, the authors consider as performance indicator the electrical COP, defined as the ratio of the cooling load and the ORC pump power consumption, obtaining values in a range between 15 and 110. The choice of VCC working fluid had only a limited influence on system thermal or electrical efficiency, with R1234ze(E) presenting slightly better results. The use of R1336mzz(Z) as the ORC working fluid resulted in slightly higher system thermal efficiencies and significantly higher system electrical efficiencies throughout the range of operating conditions studied.

4.1.3 Heat driven ejector systems

There has been significant attention given toward the selection of an appropriate working fluid for ejector refrigeration since the earliest studies. Dorantes and Lallemand [63] proposed to use zeotropic mixtures and investigated an ejector refrigeration system for air conditioning using conventional refrigerants (R11, R22, R114), pure and cleaner refrigerants, such as R123, R133a, R134a, R141b, R142b, R152a and RC318; and zeotropic mixtures. From their results, it is possible to deduce that with variable heat sink and source temperatures (evaporation temperature $T_e=10-20$ °C and vapor generator temperature $T_g=90-130$ °C), COP and entrainment ratio are mainly dependent on the working fluid and the mixture composition: R123 (COP=0.20), R141b (COP=0.21), and RC318 (COP=0.20) showed the best performance. A comparison of the performance of various working fluids was also obtained by Sun [64] based on a thermodynamic model and testing eleven fluids (water, several halocarbon compounds, an organic fluid and an azeotropic R500). The best results were obtained with R152a (COP=0.09-0.50) and R500 (COP=0.09-0.47), and the steam jet systems had low performance (COP=0-0.35). The COP variation range for several working fluids is similar to the entrainment ratio range. Cizungu et al. [65] compared R123, R134a, R152a and R717. The data obtained by the authors suggested a strong dependence of COP and entrainment ratio on the ejector geometry and compression ratio at different values of generator temperature. Furthermore, it was observed that the working fluids R134a and R152a are appropriate for heat sources at 70-80 °C and R717 is appropriate for temperatures higher than 90 °C; R134a had the highest COP of 0.1-0.45. Similar results were shown by Selvaraju and Mani [66], who compared ejector refrigeration cycle performance using R134a, R152a, R290, R600 and R717. Even in this study, R134a provided the highest COP (0.12-0.40) and critical entrainment ratio (0.20-0.45).

Recently, Kasperski and Gil [67] presented a theoretical analysis based on a 1D model developed by Huang et al. [68]. Nine heavier hydrocarbons were tested and the optimal temperature range of vapor generation for each fluid was calculated: each hydrocarbon has its own maximum entrainment ratio at its unique optimal temperature. Moreover, the optimal vapor generation temperature and maximum values of entrainment ratio increase according to the hydrocarbon heaviness; peak values of COP, however, do not follow the same trend. The highest COP, equal to 0.32, was achieved for R600a at a temperature of 102 °C and a COP of 0.28 was obtained for R601 at 165 °C. Chen et al. [69] studied the

ejector operating characteristics, investigating possible general interactions and relationships of the external parameters ($T_g=75-125$ °C, $T_e=0-16$ °C, $T_c=27-43$ °C and primary and secondary flow superheating $\Delta T=0-10$ K) and the internal parameters (efficiencies of ejector components 0.7-0.98). The ejector performance is influenced by all internal, external and geometric parameters, as characterized by COP, entrainment ratio and ejector internal entropy production. In particular, COP and entrainment ratio increase with increasing vapor generator and evaporator temperature, but decrease with increasing condensation one. Although a higher vapor generator temperature increases the COP value, an excessively high values may decrease the ideal efficiency. Thus, an optimal vapor generator temperature is observed for the maximum ideal efficiency (100 °C for R141b, 95 °C for R245fa and 110 °C for R600a), whereas a higher evaporator temperature and a lower condensation temperature reduce the irreversibility into the ejector. Moreover, the system COP and the ejector behavior are influenced by component efficiencies and the type of refrigerant used; R141b provided the largest COP. An influence of the primary or secondary flow superheat is observed on ejector and system performance when wet working fluids (with positive slope of the saturated vapor curve in the $T-s$ diagram) are used, regardless of whether this is an evident advantage for R141b, R245fa and R600a. In an investigation by Chen et al. [70], wet fluids (R134a, R152a, R290 and R430A) and dry fluids with negative slope of the saturated vapor curve in the $T-s$ diagram (R245fa, R600, R600a and R1234ze) and an isentropic fluid (R436B) were analyzed in a numerical model to compare their performance capabilities and applicability in an ejector refrigeration system. To avoid droplet formation inside the ejector when working with wet fluids, the primary flow should be superheated before the ejector nozzle inlet. In some cases, superheating may also be desirable for dry fluids and isentropic fluids. The authors also proposed a numerical approach for determining the minimum superheat before the ejector nozzle inlet, which is not known a priori. For a wet fluid, the ideal amount of superheat is the minimum amount that eliminates droplet formation, i.e., when the flow exiting the ejector nozzle ends is at saturation. This optimal superheat relies on both the generator saturation temperature and the nozzle efficiency; over-superheating of the primary flow has a limited effect on μ and no effect on COP. However, excessive superheat leads to a decrease in ideal efficiency. Using the same methodology for dry and isentropic fluids, the need for superheat can be avoided as long as fluids are not operating at the high temperatures adjacent to their critical values. Accordingly, R600 appears to be a viable

option for ejector refrigeration systems considering system performance and environmental aspects; flammability has not yet been addressed. Gil and Kaspergi [71] tested different working fluids (acetone, benzene, cyclopentane, cyclohexane, toluene, R236ea, R236fa, R245ca, R245fa, R365mfc and RC318) for high temperature heat sources ($T_g=70\text{--}200\text{ }^\circ\text{C}$, $T_e=10\text{ }^\circ\text{C}$, $T_c=40\text{ }^\circ\text{C}$). They found no one working fluid could accommodate the entire operating range, and each working fluid had its own maximum entrainment ratio and COP at a certain optimal T_g . For the low vapor generator temperature range, R236ea, R236fa and RC318, performed better than the other working fluids considered. A maximum COP of 0.23 was found for R236fa ($T_g=95\text{ }^\circ\text{C}$). For vapor generator temperature values from $105\text{ }^\circ\text{C}$ to $125\text{ }^\circ\text{C}$, the highest COP values were obtained for R236ea (COP=0.21). Above a T_g of $125\text{ }^\circ\text{C}$, the best fluid was found to be R123. The use of organic solvents may be applied for T_g higher than $120\text{ }^\circ\text{C}$. A value of COP above 0.35 was observed only for cyclopentane ($T_g>190\text{ }^\circ\text{C}$). The worst results were obtained for toluene: a COP lower than 0.2 was found across the entire operating range.

In addition to studies focused on working fluids, an increasing number of studies have focused on the dependence of system performance on ejector geometry and operating conditions. In this section, a selection of these studies is presented. The experimental and theoretical analysis presented by Sun [72] highlighted the limits of the use of fixed-geometry ejector in refrigeration cycles for low COP (approximately 0.2-0.3) and the difficulty in obtaining high performance under several operating conditions. From this study, the necessity of variable ejector geometry used in refrigeration cycles is evident, as variable geometry would increase performance across variable operating conditions and maintaining improved constant cooling system capacity. Such characteristics would allow ejector-refrigeration systems to obtain better performance with respect to conventional ejector systems making them comparable with conventional refrigeration and air-conditioning systems.

Concerning the nozzle shape and position, Aphornratana and Eames [73] found an apparent link between primary nozzle position and ejector performance based on COP, cooling capacity and critical condenser pressure for a refrigerator with an ejector. Cooling capacity and COP increase when retracting the nozzle into the mixing chamber. According to the authors, a specific nozzle position was necessary for each ejector and was not possible to find a unique optimum nozzle position for all operating conditions. Chunnanond and

Aphornratana [74] analyzed static pressure trends through the ejector with variable operating temperatures ($T_g=120-140$ °C, $T_e=5-15$ °C and $T_e=22-36$ °C), and varied superheated level of the primary flow (heat input of 0-100 W) along with different geometry and positions of the nozzle. This work found that the primary flow decreases and the secondary flow increases, i.e., a decrease in the boiler pressure, increased the COP (0.25-0.48). Furthermore, an increase in evaporator pressure (sacrificing the desired cooling temperature) led to the increase in the total mass flow and consequently increased COP (COP=0.28-0.48). The cycle performance was not influenced by the superheating level of the motive fluid before entering the nozzle. Another experimental analysis was presented by Eames et al. [75]. They described and evaluated the design of a jet-pump refrigerator. Performance maps were used to evaluate the use of R245fa and the effect of the operational parameters. They found that entrainment ratio and COP strongly depend on the nozzle geometry and position. The values varied up to 40% by changing the nozzle exit position.

Concerning the operating conditions (on-design and off-design), among the different studies, the one by Aidoun and Ouzzane [76] conducted a simulation of an ejector-based system via a thermodynamic model considering different ejector operation characteristics. The fluid mixing conditions, related to the mixing chamber geometry, the fluid type and the inlet and outlet conditions, can lead the ejector to work in off-design conditions with a decrease in performance. Moreover, in off-design conditions the increase of the internal superheat generation, due to inefficient mixing and normal shock waves, becomes relevant. The authors concluded that to prevent internal condensation, an inlet superheat of approximately 5 °C is necessary. A larger superheat limits the condenser efficiency. A numerical analysis conducted by Boumaraf and Lallemand [77] evaluated performance and operating cycle characteristics of the ejector refrigeration systems using R142b and R600a. Results found by the authors suggest that for an ejector operating at critical mode, for a given geometry and T_e , COP decreases if the T_g exceeds the design point ($T_g=120-135$ °C). Therefore, designing the ejector at the highest possible temperature is preferred, guaranteeing a better performance at a lower source temperature. Furthermore, if an ejector refrigeration system designed for working with R142b and R600a at a defined temperature operates with the fluid R142b, the system COP increases by approximately 70%. Shestopalov et al. [78], [79] studied (numerically and experimentally) the design and off-design operating conditions of an ejector refrigeration system. At first, a lumped parameter

model for design and off-design operations is developed and a screening of working fluids is performed, suggesting R145fa. Then, an experimental setup was built and results were used for validating the model. Furthermore, NXP and the shape of the mixing chamber of system performance were investigated. The problem of the optimum operating condition has been addressed by Sadaghi et al. [80] proposing an energy, exergy and exergo-economic analysis and optimizing the refrigeration system by means of an algorithm. On the other hand, ejector behavior can also be predicted by means of maps: Zegenhagen and Ziegler [81] experimentally investigated a R134a cooling system to develop three dimensional maps of the ejector operating conditions.

4.2 Objectives of the research

Among the heat driven cooling systems, the absorption solution represents a well know technology: therefore, in this study no further analysis will be done regarding this system. Regarding the combined ORC/VCC system, some drawbacks characterise especially the Organic Rankine Cycle. The design of the expander able to work with high efficiency represents one of the most technical issues due to the low expansion ratio. Furthermore, the growing interest of the international community on global warming phenomenon leads to the introduction on the market of new eco-friendly working fluids. The choice of the proper working fluid represents an actual challenge. Also, in order to obtain good performance of the ORC system, an accurate design of the heat exchangers is required: in particular, a high temperature heat exchanger working with high efficiency could lead to reducing size and therefore costs and lower input heat power. According this consideration, experimental data on evaporation at high saturation temperature are needed. Differently from the ORC systems, vapor compression cycles represent a well know technologies but the recent international regulation will impose the use of new eco-friendly refrigerants. Their performance, especially in terms of heat transfer coefficient, are unknown. Therefore, in order to obtain a proper design of the heat exchangers, experimental data of flow boiling at low temperature are needed.

In case of small-scale applications, waste heat recovery hybrid ejector cycles (WHRHEC) can represent an attractive solution especially for domestic end-users in which solar energy could be employed to produce the cooling effect. However, according the current state of the art, economic data for WHRHEC technology are not available. Therefore, a comparison in terms of cost/performance with conventional heat driven

systems already established on the market is not feasible at the moment. In order to correctly evaluate the investment costs of the WHRHEC, appropriate heat transfer correlations were used to estimate the heat transfer surface of each heat exchanger. However, there is a lack of flow boiling data at high saturation temperature.

The aim of the analysis is two-fold:

1. To determine the expected performances and costs for the typical operating conditions of a waste heat recovery hybrid ejector cycle (WHRHEC). These results will be then compared to other waste heat recovery systems. Also, an analysis on the required conditions to obtain an economical convenience for a waste heat recovery hybrid ejector cycle (WHRHEC) integrated to a conventional vapor compression cycle (VCC) is shown as case study.
2. To collect experimental data of flow boiling heat transfer coefficient for R1233zd and Propane (R290) flowing in a 6.0 mm internal diameter tube, exploring a wide range of operating conditions and analysing the effect of mass flux, saturation temperature and imposed heat flux on the heat transfer coefficient.

4.3 Thermo-economic analysis of heat driven ejector cycle

Hot water from renewable source was used as the low-grade waste heat source to simulate the ejector cooling system. A schematic representation of the layout is shown in Figure 21a. The working fluid in saturated liquid condition is driven by an electric pump that pushes the refrigerant (point 1) in a counterflow internal heat exchanger, that uses the outlet ejector flow (point 5) to pre-heat the subcooled liquid before entering the vapor generator (point 1R), in which a condition of superheated vapor is reached (point 2). The high-pressure vapor from the generator, called primary flow, expands into the motive nozzle. The pressure at the motive nozzle outlet, being lower than the evaporator pressure, allows the entrainment of the low-pressure vapor from the evaporator, called secondary flow. The mixed flow at the outlet of the ejector is firstly cooled into the internal heat exchanger and then flows into the condenser. The saturated liquid at the outlet of the condenser is divided into two parts. The first part goes through the expansion device (reaching point 3) and then it evaporates (point 4) producing the cooling effect. The remaining part is pumped to the generator pressure. The transformation occurring inside

the ejector are described in detail in the following section. An example of the corresponding thermodynamic cycle on the T-s diagram is reported in Figure 21b. The thermo-physical properties are evaluated by using Refprop 9.1 software developed by NIST [24].

The enthalpy of the mixed flow at the ejector outlet (point 5 in Figure 21b) is calculated by an energy balance on the ejector, once the ejector entrainment ratio is known by solving the ejector model described in more detail in the following paragraph.

$$h_5 = \frac{h_2 + \mu h_4}{1 + \mu} \quad (4.1)$$

The system performance is evaluated with the coefficient of performance (COP) expressed as follows with referring to the numeration in Figure 21. The electrical power required by the pump was neglected.

$$COP = \frac{\dot{Q}_{ev}}{\dot{Q}_g} = \mu \frac{h_4 - h_3}{h_2 - h_{1R}} \quad (4.2)$$

Where \dot{Q}_{ev} and \dot{Q}_g are the heat power (kW) at the evaporator and the generator, respectively, μ is the entrainment ratio (defined in the following section) and h is the refrigerant specific enthalpy (kJ kg^{-1}).

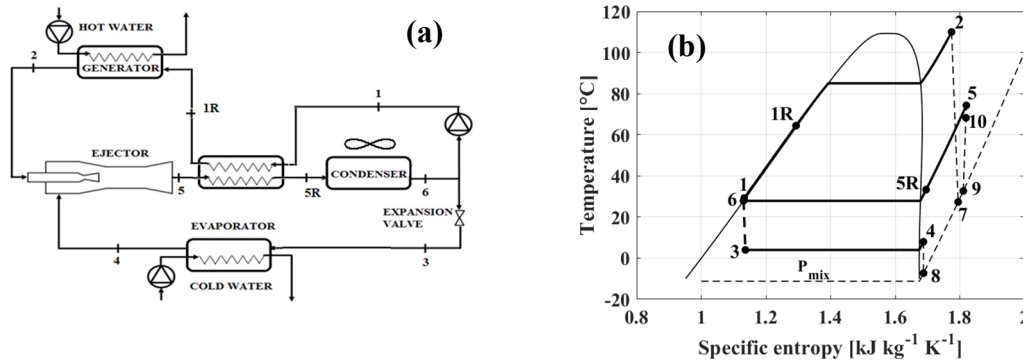


Figure 21. (a) Schematic lay-out (b) Example of an ejector cooling cycle on T-s diagram for the fluid R1234ze.

4.3.1 Ejector model

Differently from the ejector employed in heat pumps, both primary and secondary flows are in vapor conditions, as well as the mixing flow at the outlet of the ejector. Three different operation modes of the vapor ejector can be defined (critical, subcritical and

backflow) depending on the value of the condensing pressure, once the low and high evaporation temperatures are fixed. The operation modes are depicted in Figure 22. In the critical mode (on-design conditions), both the primary flow and secondary flows are choked and the entrainment ratio is constant; the condensing pressure is lower than the critical condensing pressure (P_{cc}). In the subcritical mode (off-design conditions), the condensing pressure is between the critical condensing pressure and the breakdown pressure (P_{cb}). In this mode, the entrainment ratio reduces as the condensing pressure increases until it reaches zero at the ejector breakdown pressure. Beyond the ejector breakdown pressure, there is backflow and the ejector malfunctions.

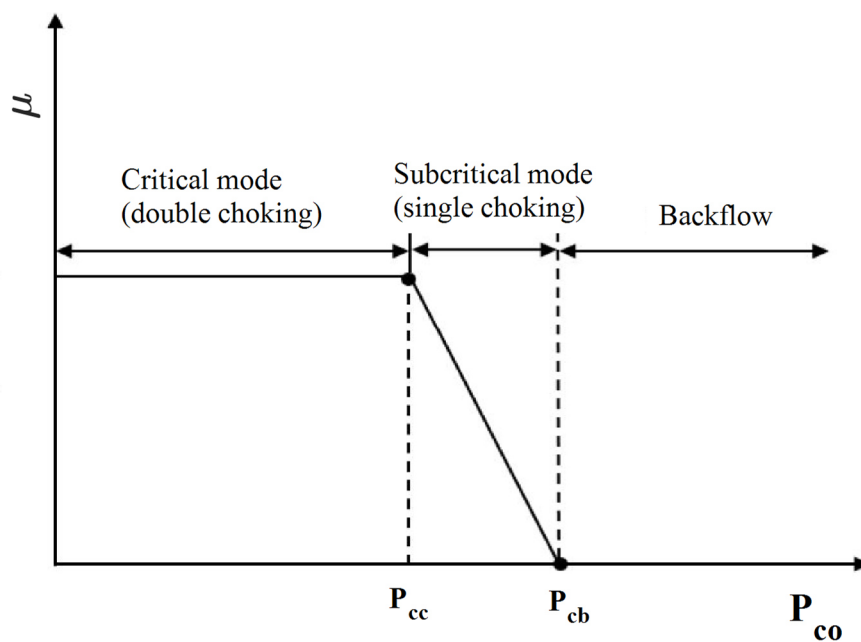


Figure 22. Operation modes of an ejector.

In order to simulate the ejector performance at critical mode operation, the one-dimensional model presented in the theoretical work of Chen et al. [82] is employed in the current optimization process. In this model, the mixing process of the flows is considered occurring at constant pressure, lower than the evaporation level, by taking into account shock process inside the ejector. The modeling of the thermodynamic processes occurring inside the ejector is simplified by the assumption of ideal gas behavior. Considering the numbering of Figure 23, once the conditions at the inlet of the primary (point 2) and secondary (point 4) flows and the ejector outlet pressure (point 5) are given, the model calculates the optimum entrainment ratio μ and the corresponding area ratio A_r .

The employed model considers some assumption to simplify the analysis:

- The flow inside the ejector is studied in steady-state conditions and one-dimensional. The ejector walls are adiabatic through the surrounding.
- The primary and the secondary flow are superheated vapor in order to avoid droplet condensation during the expansion process. Moreover, their velocities are negligible before entering the ejector (states 2 and 4 in Figure 24 respectively). The velocity of the mixed flow leaving the ejector (at state 5) is also neglected.
- Isentropic efficiencies in the nozzle (η_N), in the diffuser (η_D), as well as in the mixing chamber (η_M) are considered to take into account the flow losses.

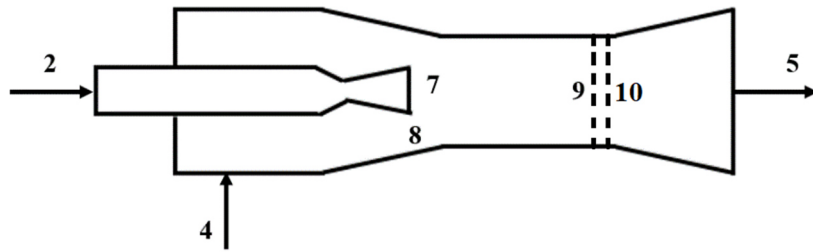


Figure 23. Schematic ejector representation.

According to these assumptions, the thermodynamic processes occurring inside the ejector are shown on T-s diagram in Figure 24. The line 2-7 represents the expansion of the flow inside the motive nozzle taking into account the nozzle efficiency; similarly, point 8 represents the end point of the expansion of the secondary flow. The conditions 9 and 5 represent the end points of the real process inside the mixing chamber and the diffuser, respectively. The pressure at the points 7, 8 and 9 is the mixing pressure (indicated in the following as P_{mix}), which is lower than the secondary flow pressure. The process inside the diffuser include a shock wave phenomenon (9→10) and a further pressure recovery (10→5) due to the divergent shape of the diffuser. The total losses occurring in the total pressure recovery process (9→5) are summarized through the diffuser efficiency η_D as described in Eq. (4.21).

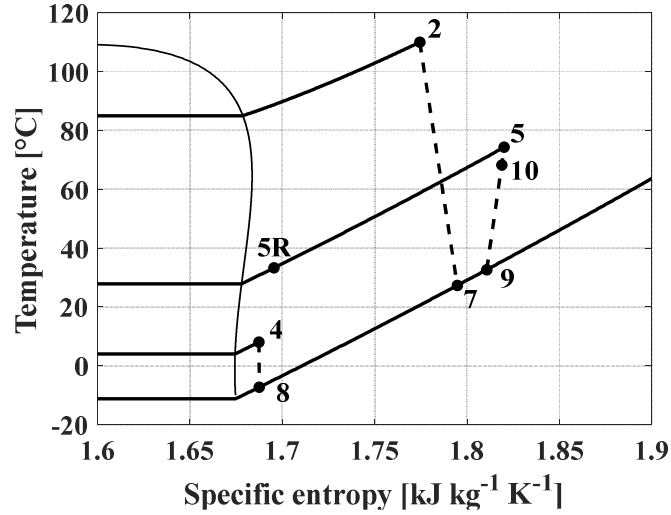


Figure 24. Ejector working processes on T-s diagram.

Governing equations

Below, the thermodynamic model (equations from (4.3) to (4.26)) of the ejector presented in the work of Chen et al. [82] is described, assuming ideal gas behaviour. According to the above assumptions, the velocity of the primary flow at the nozzle exit (u_7) is evaluated by the conservation of energy on the motive nozzle:

$$u_7 = \sqrt{2\eta_N (h_2 - h_{7s})} \quad (4.3)$$

$$h_{7s} = f(p_{mix}, s_2) \quad (4.4)$$

where the isentropic efficiency in the nozzle η_N is defined as:

$$\eta_N = \frac{h_2 - h_7}{h_2 - h_{7s}} \quad (4.5)$$

The expansion process of the primary flow in the nozzle can be written also in terms of Mach number at state 7 by assuming ideal gas behaviour, as reported in [83], [84].

$$M_{g7} = \sqrt{\frac{2\eta_N}{k-1} \left[\left(\frac{p_2}{p_{mix}} \right)^{\frac{k-1}{k}} - 1 \right]} \quad (4.6)$$

The velocity u_8 of the secondary flow after the expansion to the mixing pressure p_{mix} can be evaluated as below by using the energy conversation principle, considering this process to be isentropic due to low velocity of the flow giving very small losses [82].

$$u_8 = \sqrt{2(h_4 - h_8)} \quad (4.7)$$

$$h_8 = f(p_{mix}, s_4) \quad (4.8)$$

Similarly to the primary flow, the Mach number of the secondary flow at state 7 (assuming ideal gas) is given by the following equation, as demonstrated in [83].

$$M_{e7} = \sqrt{\frac{2}{k-1} \left[\left(\frac{p_4}{p_{mix}} \right)^{\frac{k-1}{k}} - 1 \right]} \quad (4.9)$$

The mixing of the primary and the secondary are totally completed before the occurring of shock wave in the mixing chamber. The balance of the momentum of the ideal mixing process (7 & 8 \rightarrow 9) can be expressed as:

$$u_{9s} = \frac{u_7 + \mu \cdot u_8}{1 + \mu} \quad (4.10)$$

where μ is the entrainment ratio of the ejector, defined as the ratio between the mass flow rates of the secondary flow to the primary flow. Using the mixing efficiency η_M definition, as Yu et al. [85] and reported in Eq. (4.11), the velocity u_9 and enthalpy h_9 for the real mixing process are obtained by Eqs. (4.12) and (4.13).

$$\eta_M = \frac{u_9^2}{u_{9s}^2} \quad (4.11)$$

$$u_9 = u_{9s} \sqrt{\eta_M} = \frac{u_7 + \mu \cdot u_8}{1 + \mu} \sqrt{\eta_M} \quad (4.12)$$

$$h_9 = \frac{h_7 + \mu \cdot h_8}{1 + \mu} - \frac{u_9^2}{2} \quad (4.13)$$

$$s_9 = f(p_{mix}, h_9) \quad (4.14)$$

The critical Mach number at condition 9 in terms of the critical Mach number of the primary flow and the secondary flow at the state 7 is then obtained by considering the mixing efficiency η_M :

$$M_9^* = \sqrt{\eta_N} \frac{M_{g7}^* + \mu M_{e7}^* \sqrt{T_4/T_2}}{\sqrt{(1+\mu)(1+\mu T_4/T_2)}} \quad (4.15)$$

The relationship between the Mach number M and the critical Mach number M^* at any point inside the ejector is given as [83]:

$$M^* = \sqrt{\frac{M^2(k+1)}{M^2(k-1)+2}} \quad (4.16)$$

The Mach number at point 9 is then transferred as:

$$M_9 = \sqrt{\frac{2M_9^{*2}}{(k+1)-M_9^{*2}(k-1)}} \quad (4.17)$$

Since the velocity of the mixed flow leaving the ejector (at condition 5), is neglected the enthalpy at the ejector outlet (h_5) is obtained by using energy conservation [85]:

$$h_5 = h_9 + \frac{u_9^2}{2} \quad (4.18)$$

$$h_5 = h_9 + \frac{h_{5s} - h_9}{\eta_D} \quad (4.19)$$

$$h_5 = f(p_5, s_9) \quad (4.20)$$

where the definition of diffuser efficiency η_D is given a

$$\eta_D = \frac{h_{5s} - h_9}{h_5 - h_9} \quad (4.21)$$

Rewriting Eq. (4.12) using Eqs (4.3), (4.7), (4.18) and (4.21) the entrainment ratio can be found:

$$\mu = \frac{\dot{m}_{sf}}{\dot{m}_{pf}} = \frac{\sqrt{2\eta_N(h_2 - h_{7s})} - \sqrt{2(h_{5s} - h_9)/(\eta_D\eta_M)}}{\sqrt{2(h_{5s} - h_9)/(\eta_D\eta_M)} - \sqrt{2(h_4 - h_8)}} \quad (4.22)$$

As a consequence of the normal shock wave (9→10), the velocity decreases and the pressure increases. Again, assuming ideal gas behaviour, the Mach number of the mixed flow and pressure increase after the shock at point 10 are written as [84]:

$$M_{10} = \sqrt{\frac{M_9^2 + 2/(k-1)}{2kM_9^2/(k-1) - 1}} \quad (4.23)$$

$$\frac{p_{10}}{p_9} = \frac{1 + kM_9^2}{1 + kM_{10}^2} \quad (4.24)$$

Moreover, the further pressure recovery in the diffuser up to the outlet (10→5) follows the relationship below:

$$\frac{p_5}{p_{10}} = \left[\frac{k-1}{2} M_{10}^2 + 1 \right]^{\frac{k}{k-1}} \quad (4.25)$$

It should be noted that p_5 in Eq. (4.25) is the calculated pressure at the ejector outlet, which should be compared with the defined ejector outlet pressure, e.g. the condenser pressure. Two iterative processes are therefore needed in the calculation program to achieve the ejector outlet pressure p_5 and the entrainment ratio μ .

The area ratio A_r is defined as the ratio of the constant area section of the mixing chamber (A_{mix}) to the nozzle throat area (A_{th}), and it is expressed by the following equation, as indicated by Chen et al. [82].

$$A_r = \frac{A_{mix}}{A_{th}} = \frac{p_2 (1 + \mu)^{0.5} (1 + \mu T_4/T_2)^{0.5} (2/(k+1))^{1/(k-1)} (1 - 2/(k+1))^{0.5}}{p_c (p_9/p_5)^{1/k} (1 - (p_9/p_5)^{(k-1)/k})^{0.5}} \quad (4.26)$$

The mass flow rate of the primary flow through the nozzle is determined by Eq. (4.27) [86] considering choked conditions at the nozzle throat, where R represents the specific gas constant, A_{th} is the nozzle throat cross section, k is the heat capacity ratio, and η_N is the nozzle efficiency defined previously. Once the primary flow rate is known, the nozzle throat section can be evaluated by using Eq. (4.27).

$$\dot{m}_{pf} = p_2 \frac{A_{th}}{\sqrt{T_2}} \sqrt{\frac{k}{R} \left(\frac{2}{k+1} \right)^{(k+1)/(k-1)}} \sqrt{\eta_N} \quad (4.27)$$

The following two parameters are considered to describe the ejector performance in refrigeration cycle: the pressure lift Π is defined as the ratio between the pressure at the outlet of the ejector and the pressure of the secondary flow rate, whereas β is the ratio between the pressure of the primary flow and the pressure at the ejector outlet.

$$\Pi = \frac{p_5}{p_4} = \frac{p_{co}}{p_{ev}}; \quad \beta = \frac{p_2}{p_5} = \frac{p_g}{p_{co}}$$

Computational procedure

A computational procedure with two iteration processes is needed to find the ejector performance at given operating conditions. The solving algorithm is written using Matlab [23] and the refrigerant properties are calculated by using Refprop 9.1 [24]. The following steps are included in the solving procedure:

1. The working fluid and operating conditions (T_2, p_2, T_4, p_4, p_5) are selected. The isentropic ejector efficiencies (η_N, η_M, η_D) and the heat capacity ratio (k) are given as input.
2. An initial value for the pressure at the nozzle exit (p_{mix}) is estimated. Eqs. (4.2)-(4.5) are solved to obtain u_7 , while Eqs. (4.7) and (4.8) is used to calculate u_8 .
3. A guess value of μ is set initially. Eqs. (4.10)-(4.14) and (4.18)-(4.21) are used to calculate h_9, u_9 , and h_5 respectively. Then, the new value of entrainment ratio μ can be obtained from the Eq. (4.22).
4. The calculated μ is compared to the guess value. If the difference between those two values is lower than an acceptable tolerance (10^{-2} for the present thesis), the program will continue or a new μ value will be assumed and the previous step (3) is repeated.
5. The pressure at the ejector outlet p_5 is calculated by combining the Eqs. (4.6) and (4.9) and (4.15)-(4.17) and (4.23)-(4.25). This calculated value is compared to the input condenser pressure. A new value for p_5 is estimated and the previous steps are repeated until the desired value is reached.
6. The parameters μ and p_{mix} are stored as the converged solution. The area ratio A_r is can be calculated by Eq. (4.26).

4.3.2 Heat exchanger modelling

Proper heat transfer correlations are considered for each heat exchanger to estimate their heat transfer surface. According to the selected fluids properties, the high-pressure evaporator and the regenerative heat exchanger are designed to work in a range of pressures that are suitable for the use of plate heat exchangers, which are preferred to shell-and-tube configuration because of their compactness. Considering the lower pressure levels, a one pass shell and tube heat exchanger is chosen for the low temperature evaporator. In this way, boiling takes place at the outer surface of the tube bundle and large pressure drops are

therefore avoided. A fin and tube heat exchanger is chosen for the condenser, in which air is used as secondary fluid.

The overall heat transfer coefficient U ($\text{W m}^{-2}\text{K}^{-1}$) cannot be considered constant during the heat transfer process, especially in the single phase/two phase transition. For this reason, different sections for single-phase and two-phase were considered with appropriate heat transfer correlations. Each heat exchanger is divided into discrete elements having an elementary area dA , corresponding to an elementary length dz and equal to 5 mm. With the assumption of heat exchanger adiabaticity through its surroundings, the heat transfer differential equation reads as:

$$\delta\dot{Q}(z) = U(z)dA \cdot [T_{hot}(z) - T_{cold}(z)] \quad (4.28)$$

The temperature of the refrigerant T (K), was calculated with Refprop 9.1 developed by NIST [24] using both the pressure and the enthalpy local value; the same process was used for the secondary fluid (water or air). The local enthalpies are integrated from the inlet of each heat exchanger, according to the energy balance reported in Eqs. (4.29) and (4.30):

$$h_{ref}(z+1) = h_{ref}(z) - \frac{d\dot{Q}}{\dot{m}_{ref}} \quad (4.29)$$

$$h_f(z+1) = h_f(z) - \frac{d\dot{Q}}{\dot{m}_f} \quad (4.30)$$

where the subscripts *ref* and *f* refer to the refrigerant and the secondary fluid side, respectively. The overall heat transfer coefficient U is computed with Eq. (4.31), where δ is the thickness (m) of the tube or the plate and κ_{mat} is the material thermal conductivity ($\text{W m}^{-1}\text{K}^{-1}$). The convective heat transfer coefficient α ($\text{W m}^{-2}\text{K}^{-1}$) for both fluids can be evaluated with Eq. (4.32), where κ_{fluid} is the fluid thermal conductivity ($\text{W m}^{-1}\text{K}^{-1}$).

$$U = \frac{1}{\frac{1}{\alpha_{ref}} + \frac{\delta}{\kappa_{mat}} + \frac{1}{\alpha_f}} \quad (4.31)$$

$$\alpha = \frac{Nu \cdot \kappa_{fluid}}{D_h} \quad (4.32)$$

For the pool boiling occurring in the shell and tube heat exchanger low pressure evaporator, the correlation of Cooper [88] is chosen, which is the benchmark reference and recognized to work well (at least for smooth tubes and not GEWA type) in a very wide range of reduced pressures. For the plate heat exchangers, there is no comprehensive data for flow boiling for each considered fluid in scientific literature, as it can be seen from the review of Amalfi et al. [89]. In this review, the reported correlation of Park and Kim [90] is suggested. Although this method was validated by using experimental data related to a large number of working fluids, unfortunately Propane and R1233zd were investigated in operating conditions different with respect to those occurring in the simulations described in this chapter. These two fluids are not considered for high temperature applications; furthermore, R1233zd is a relatively recent substance on the market and hence experimental studies on flow boiling heat transfer coefficient are not present in scientific literature. With the aim to validate the use of Park and Kim correlation [90] in the operating conditions analyzed in this chapter, an experimental validation in similar conditions will be described in the following section. This method is sufficiently solid since, although developed for a single fluid (R134a), it takes into account the passage from laminar to turbulent flow and the effect of the reduced pressure by means of the equivalent Reynolds number (that includes the density ratio). The same considerations are effective for the Shah correlation [91] that we used for condensation heat transfer inside tubes, since the effect of the reduced pressure is explicitly provided in the authors' expression. The summary of the correlations for the Nusselt number Nu or the convective heat transfer coefficient for each heat exchanger geometry and for single-phase and two-phase heat transfer are reported in Table 8. The geometric elementary details are fixed for all the permuted solutions and are defined for each heat exchanger type in Appendix B.

An algorithm was developed and implemented in a Matlab [23] code to obtain the surface of each heat exchanger (the geometrical parameters fixed and to be calculated for each type of heat exchanger are specified in Appendix B). The following steps are included in the solving procedure:

1. The thermodynamic and geometric parameters are fixed as input for the model.
2. At the first elementary section ($z=1$), the local temperature of the working fluid is set equal to the temperature in points 2, 3 and 5 for the generator, evaporator and condenser respectively.

3. The overall heat transfer coefficient U for each elementary volume is evaluated by Eqs. (4.31) and (4.32) by using the mentioned prediction methods as shown in Table 8.
4. The elementary heat power is obtained from Eq. (4.28).
5. By considering the heat exchanger adiabatic through its surroundings, the energy balances from Eq. (4.29) and (4.30) allow the calculation of the specific enthalpies (and temperatures) for the subsequent integration steps ($z+1$).
6. By using the thermodynamic properties evaluated in the previous step, the procedure (from step 3 to 5) is repeated until the heat exchangers surface balances the required heat power.

Finally, the total heat transfer surface A is then obtained for each investigated geometric configuration and boundary condition.

Table 8. Single phase and two-phase heat transfer correlations.

Single-phase	Two-phase
Plate heat exchanger	
Correlation of Martin [92] $Nu = 0.205 Pr^{1/3} \left(\frac{\mu_m}{\mu_w} \right)^{1/6} (f Re^2 \sin(2\beta))^{0.374}$	Boiling heat transfer correlation of Park and Kim [90] $Nu = 12.47 Re_{eq}^{0.33} Pr_1^{1/3}$
Shell and tube heat exchanger– shell side	
Correlation of McAdams [93] $Nu = 0.36 \left(\frac{D_e G_s}{\mu} \right)^{0.55} \left(\frac{c_p \mu}{k} \right)^{1/3} \left(\frac{\mu}{\mu_w} \right)^{0.14}$	Pool boiling correlation of Cooper [88] $\alpha_{nb} = 55 \cdot pr^{0.12} (-0.4343 \log(pr))^{-0.55} M^{-0.5} q^{0.67}$
Shell and tube heat exchanger– tube side	
Correlation of Dittus-Boelter [94] $Nu = 0.023 Re^{0.8} Pr^{0.4}$	
Fin and tube heat exchanger	
Wang et al. [95] $J = 0.096 \cdot Re_{air}^{P3} \cdot N_R^{P4} \cdot \left(\frac{P_{fin}}{D_c} \right)^{P5} \cdot \left(\frac{P_{fin}}{D_h} \right)^{P6} \cdot \left(\frac{P_{fin}}{P_t} \right)^{-0.93}$ $\alpha_{air} = J \cdot \rho_{air} \cdot u_{air,max} \cdot c_{p,air} \cdot Pr_{air}^{-2/3}$	Condensation inside tubes, correlation of Shah [91] $Nu = 0.023 Re^{0.8} Pr^{0.4} \left[(1-x)^{0.8} + \frac{3.8x^{0.76} \cdot (1-x)^{0.04}}{pr^{0.38}} \right]$

4.3.3 Working fluids

The properties of the working fluid influence the performance of the vapor compression cooling systems. An appropriate refrigerant can not only provide good system performance and therefore energy saving, but also involves less environmental issues. Basic considerations require eco-friendly working fluids (low OPD and GWP), safety issues, low cost and availability. Furthermore, as reported in the work of Varga et al. [87], more specific prescriptions should be taken into account when choosing a working fluid for ejector cooling systems:

- high latent heat value in the evaporator and generator temperature range to minimize the mass flow rate per unit of heat power;
- relatively high critical temperature to make the system feasible in a wide range of generator temperatures;
- not too high saturation pressure in the generator and not too low in the evaporator.

Also, the slope of saturated vapor line should be considered. The use of dry refrigerant is recommended in order to avoid the development of droplets inside the ejector, which may block the effective area. In this analysis water is excluded, since water has a rather low COP according to [87]. HFCs are also excluded due to their high GWP. Therefore, hydrocarbons as Butane (R600), Isobutane (R600a) and Propane (R290) and new HFO refrigerants R1234ze and R1233zd are considered. Although Ammonia (R717) is affected by several issue related to their high toxicity, it was considered in this analysis due to its favorable thermodynamic properties. Finally, the conventional refrigerant R134a was also considered, although the F-gas regulation [9] limits their use due to the high GWP value. The main thermophysical and environmental properties of the selected working fluids are listed in Table 9. The corresponding saturation curves are reported in Figure 25.

Table 9. Characteristics of the selected working fluids.

Fluids	T_{cr} [°C]	p_{cr} [bar]	ASHRAE classification	GWP	ODP
R1234ze	109.4	36.4	A2L	6	0
Ammonia (R717)	132.3	113.0	B2L	0	0
R1233zd(E)	165.6	37.7	A1	1	0
Isobutane (R600a)	134.7	36.4	A3	3	0
R134a	101.1	40.7	A1	1430	0

Butane (R600)	152.0	38.0	A3	4	0
Propane (R290)	96.7	42.5	A3	3	0

4.3.4 Cost function

The set-up costs are calculated by considering the single cost of each component (working fluid pump, high-pressure evaporator, condenser, low-pressure evaporator, regenerative heat exchanger and ejector), for which a cost correlation is used, as listed in Table 10. Specifically, an exponential expression [96] as a function of the sole nominal power is chosen for the pump price. The investment costs of the plate heat exchangers (high pressure evaporator and regenerative heat exchanger) and of the fin and tube condenser are obtained as a linear function of the total heat transfer surface, as suggested by [96] and [97].

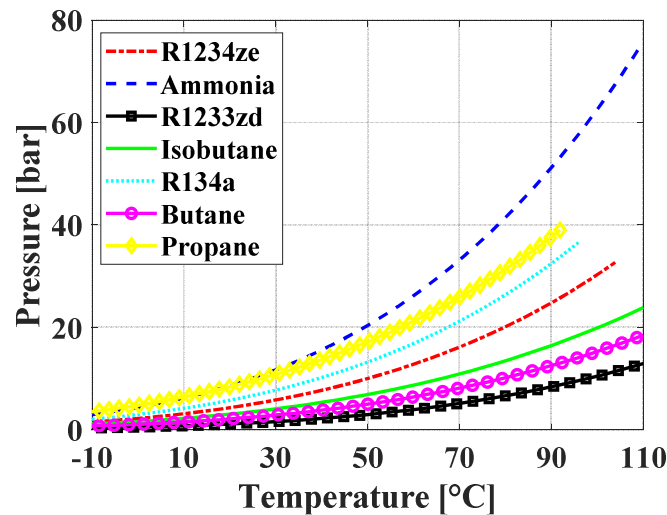


Figure 25. Saturation curves in pressure-temperature diagram for the selected working fluids.

The shell and tube low-pressure evaporator cost is taken from the work of Wildi-Tremblay and Grosselin [98] related to the total heat transfer surface with a power function. Since the ejector has to be designed ad-hoc for the specific application and cannot be treated as a commercial item, in this analysis the ejector cost is estimated as a linear function of the minimum required volume of a brass block from which the final ejector geometry is obtained through material removal processes (considering density of the brass ρ_{brass} of 8.73 kg cm^{-3} and specific cost c_{brass} of 4.85 € kg^{-1}). When using flammable working fluids, additional safety issues must be taken into account for electronic components: in this case

an increasing of investment costs of +20% is considered for the condenser (due to the presence of Atex fan type required in case of hazardous fluids) and pump. In addition, a corrective enhancement factor of 1.30 is instead considered when using ammonia (R717), in order to take into account both toxicity and flammability issues.

4.3.5 Performance analysis

Using the ejector and the system model previously shown, 42 simulations were carried-out in order to define an entrainment ratio map in terms of pressure lift and β ratio useful to find the influence of several temperature differences at pinch point on the ejector performance for each investigated working fluid.

Table 10. Cost functions for each component.

Components	Dependent variable	Investment costs IC [€]	References
Working fluid pump	Electrical power [W]	$IC_p = 900 \left(\frac{W}{300} \right)^{0.25}$	[96]
High pressure evaporator	Heat exchanger surface [m ²]	$IC_g = 190 + 310 \cdot A$	[96]
Low pressure evaporator	Heat exchanger surface [m ²]	$IC_{ev} = 3.28 \cdot 10^4 \left(\frac{A}{80} \right)^{0.68}$	[98]
Condenser	Heat exchanger surface [m ²]	$IC_{co} = 25 \cdot A$	[97]
Regenerative heat exchanger	Heat exchanger surface [m ²]	$IC_{rhe} = 190 + 310 \cdot A$	[96]
Ejector	Minimum required volume of brass [cm ³]	$IC_{ej} = \rho_{brass} \cdot c_{brass} \cdot V$	

In particular, the hot water at the vapor generator inlet is supplied by considering a solar heating system able to produce hot water at 120°C, as reported in the current literature [99], [100]. For a given heat load, a too low temperature variation of the secondary flow at the vapor generator would require higher mass flow rates for the secondary fluid (and thus higher pumping costs) and also a lower refrigerant superheat, which could be too small to be plausibly controlled. On the contrary, a too high temperature variation would lead to low refrigerant saturation temperatures, strongly penalizing the thermodynamic cycle efficiency. Due to this fact, in this analysis an outlet temperature of the secondary fluid of 80 °C was chosen in order to taking into account these two competing aspects. Furthermore, the power consumption of the auxiliary components such as pumps and fans of the heat

exchanger have been not considered in this analysis. The data used are listed in Table 11. The simulated pinch points values are listed in legend in the following figures. The low-pressure evaporating temperature is directly obtained from the chilled water temperature and the given pinch point value, whereas the evaluation of the remaining saturated conditions (condenser and high-pressure evaporator) are obtained with an iterative process seeking for the exact pinch point provided. In a first step, the high temperature evaporation and condensation pressures are fixed at guess values and the thermodynamic cycle is constructed. Then, the pinch point (occurring at saturated vapor and liquid for the condenser and the generator, respectively) is calculated and the pressures are accordingly changed, adjusting the guess values in order to obtain the design temperature difference. For instance, if the pinch point value is lower than the arranged one, the condenser/evaporator pressure has to be accordingly increased/decreased. All the thermodynamic and transport properties of refrigerants are evaluated through the software Refprop 9.1, developed by NIST [24].

Table 11. Specification of the simulated boundary conditions.

Cooling load [kW]	20	Working fluid temperature at vapor generator outlet [°C]	110
Water temperature at the vapor generator (inlet/outlet) [°C]	120/80	ΔT superheating at evaporator outlet [K]	4
Air temperature at the condenser (inlet/outlet) [°C]	20/25	Regenerative heat exchanger efficiency	0.90
Water temperature at the evaporator (inlet/outlet) [°C]	12/7	Pump efficiency	0.70
Quality at condenser outlet	0.0		

Figure 26 shows the entrainment ratio μ map as function of the β ratio and pressure lift II . The main objective of the following figures is to present the general trends as a function of the operating conditions indicated in the corresponding legends. Considering the working fluid R134a, the configuration with 1 K of pinch point for all heat exchangers was excluded since the temperature exceeded the critical value of 101.1 °C. The refrigerant R1233zd is characterized by higher values of II and β due to low saturation pressure at fixed temperature with respect to the other investigated fluids. As it can be seen, when the lower value of the temperature difference at the pinch point is considered for all heat exchanger, the maximum entrainment ratio is obtained for all refrigerants, reaching a value of 0.438 for R1233zd. The results shown in Figure 26 can be useful to identify the influence of the variation of each temperature difference at pinch point keeping constant the other

two. Assuming as reference the configuration with all temperature differences at pinch point of 5 K for R1233zd, by increasing the pinch point from 5 K to 10 K, lower values of the entrainment ratio are obtained. In particular, the highest reduction is obtained when the variation of the temperature different at pinch point occurs at the condenser with the entrainment ratio passing from 0.210 to 0.097. In this case, the increase of the pinch point at the condenser negatively affects the β ratio, while increases the pressure lift: both the effects contribute to a drop of the entrainment ratio. Instead, when the pinch point at the vapor generator (or the evaporator) increases from 5 K to 10 K, the entrainment ratio μ decreases from 0.210 to 0.151 (to 0.13 for the low-pressure evaporator).

Figure 27 shows the system COP as function of β and Π with a very similar trend with respect to the previous Figure 26. The system COP is in fact strictly related to the entrainment ratio due to its definition as reported in Eq. (4.2) and, with enthalpy variation ratio at the low and high pressure evaporators from 0.8 to 1.25, μ and COP assume almost the same value. When the entrainment ratio is lower than 0.1, the system performance suffers an abrupt decrease, due to high primary mass flow rates \dot{m}_{pf} (at the vapor generator) to satisfy the required low-pressure evaporator mass flow rate \dot{m}_{ev} . The detailed results of the thermodynamic analysis are reported in Appendix A for each refrigerant and all the simulated conditions.

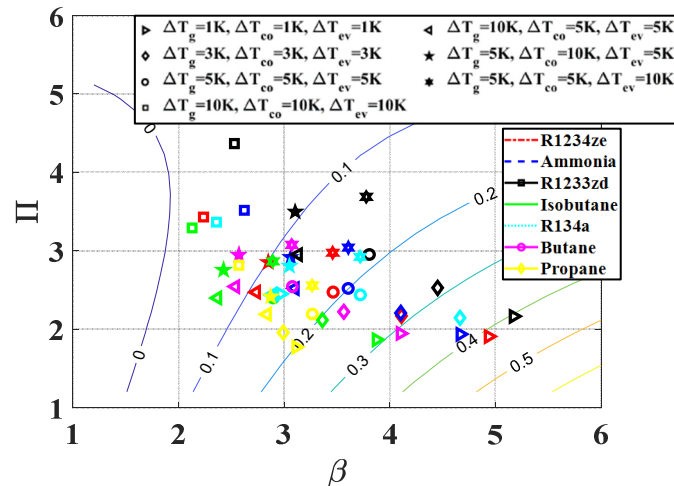


Figure 26. Entrainment ratio as function of pressure ratio and pressure lift for different pinch point values at the heat exchangers.

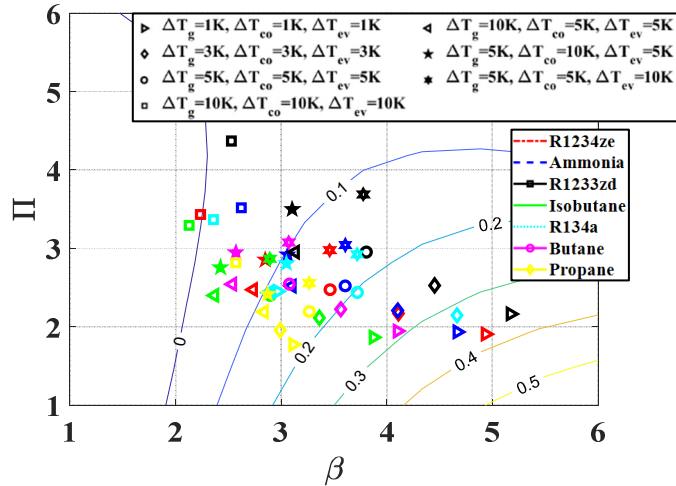


Figure 27. System COP as function of pressure ratio and pressure lift for different pinch point values at the heat exchangers.

4.4 Thermo-economic optimization

The same boundary conditions concerning the cooling load, the secondary fluids temperatures and the refrigerant thermodynamic constraints from Table 11 are still used for the thermo-economic analysis. The list of permuted parameters is instead provided in Table 12, by obtaining a total amount of 1500 simulations run. The complete set of solutions in terms of COP versus specific investment costs is shown in Figure 28. Each color refers to a working fluid, whereas the bigger markers correspond to the subset of solutions presented in the thermodynamic analysis (empty and full markers respectively for a regenerative heat exchanger efficiency of 0.90 and 0.50). Their shape is recalled in the legend and is related to specific pinch point values. All the remaining intermediate combinations are drawn with x-shaped markers.

By increasing the pinch point values, the performance decreases as already shown in the thermodynamic analysis. The effect of a different minimum temperature difference on the specific investment costs is, however, not univocal. From one side, higher pinch point values lead to lower heat exchanger efficiency that are therefore more compact (and cheaper). From the other side, the entrainment ratio μ decreases dramatically with an increasing pinch point (see Figure 26), leading to a lower entrained mass flow rate and therefore higher thermal loads at the high-pressure evaporator and condenser in order to satisfy the required cooling load, resulting in increased heat transfer surfaces and costs.

Table 12. Operating conditions used for the thermo-economic analysis.

Parameter	Range
Pinch points for the heat exchangers [K]	1; 3; 5; 7 ; 10
Fluids	R1234ze, Ammonia (R717), R1233zd(E), Isobutane (R600a), R134a, Butane (R600), Propane (R290)
Regenerative heat exchanger efficiency	0.50; 0.90

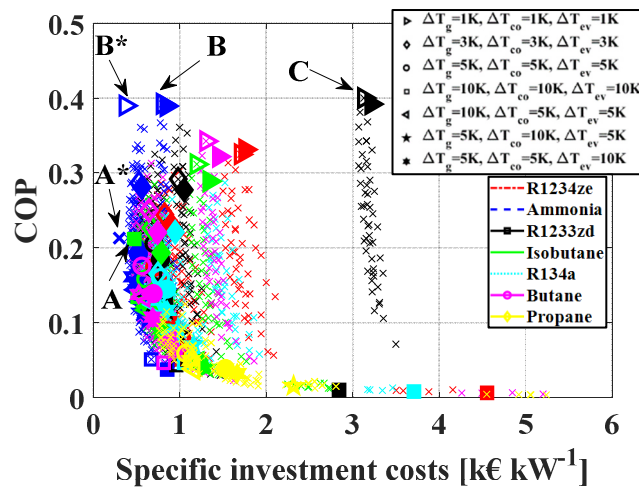


Figure 28. COP versus specific investment costs for all the chosen combinations. The highlighted markers refer to the solutions investigated for the thermodynamic analysis and each color is related to a specific working fluid.

As regards the refrigerant effect, although economically penalized by toxicity and flammability issues, the investigated solutions using ammonia (R717) as working fluid are those falling in the lowest specific investment cost region, due to a very high latent heat and its particularly favorable thermodynamic and transport properties for two-phase heat transfer. The opposite situation is observed for the synthetic refrigerant R1233zd(E), that presents higher specific set-up costs with respect to other refrigerants when the same boundary conditions are applied. For the present analysis, three singular solutions (namely A, B and C), chosen as possible “optimum” cases, are extracted from the total set of simulations and the related main parameters are summarized in Table 13. The share of the total investment costs for these configurations is specified in Figure 29.

Table 13. Summary of the three configurations chosen as possible optimum case. The asterisk solutions refer to the use of a plate heat exchanger instead of a shell and tube heat exchanger for the low-pressure evaporator.

	Fluid	ΔT_g [°C]	ΔT_{co} [°C]	ΔT_{ev} [°C]	ϵ_{RHE} [-]	T_g [°C]	P_g [bar]	T_{co} [°C]	P_{co} [bar]	T_{ev} [°C]	P_{ev} [bar]	μ [-]	Π [-]	β [-]	COP	ic [k€ kW ⁻¹]
A/A*	R717	7	1	10	0.50	80.2	41.6	25.8	10.3	-3.0	3.8	0.227	2.69	4.04	0.21	0.40/0.30*
B/B*	R717	1	1	1	0.50	88.3	49.4	25.9	10.3	6.0	5.3	0.407	1.93	4.79	0.39	0.80/0.37*
C	R1233zd	1	1	1	0.50	87.9	7.93	25.6	1.32	6.0	0.62	0.497	2.13	5.99	0.40	3.13

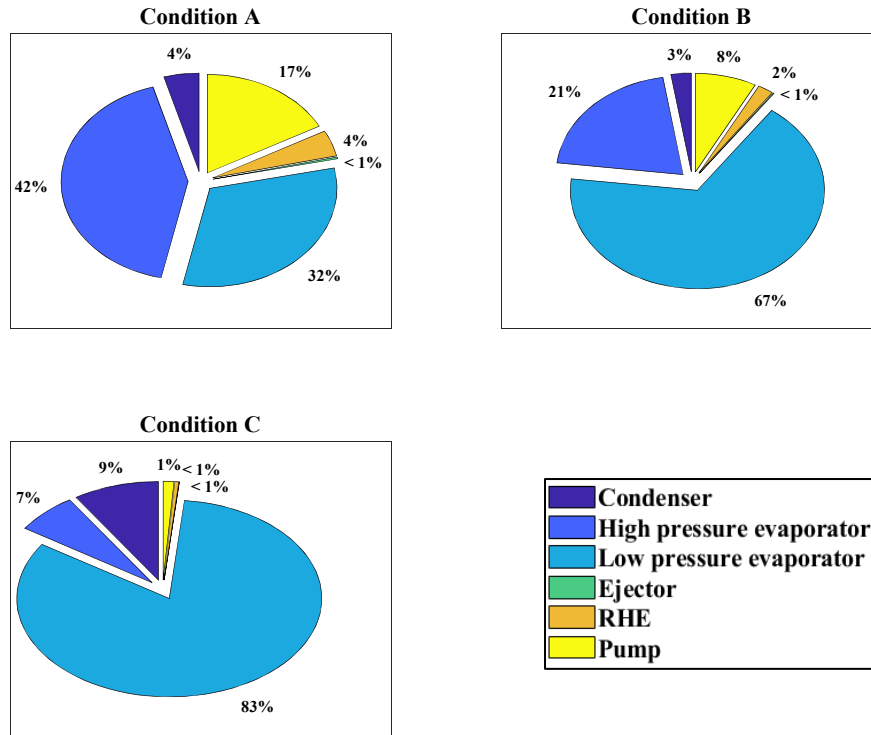


Figure 29. Share of the total investment costs for the hybrid ejector plant.

Specifically, solution A provides the plant configuration with the lowest specific investment cost of 0.40 k€ per kW of cooling load. Almost half of the entire cost (42%) is related to the high-pressure evaporator, followed by the low-pressure evaporator (32%), the electric pump (17%) and the fin and tube condenser (4%). This configuration uses ammonia (R717) as refrigerant, with a pinch point of 1 °C at the condenser, with a minimum temperature difference of 7 °C and 10 °C in high and low-pressure evaporator respectively and an efficiency of the regenerative heat exchanger of 0.50. The related COP is however low (0.21) caused by a reduced entrainment ratio of 0.227. From another perspective, solution C maximizes the system performance, with a COP of 0.40, using R1233zd(E) as

refrigerant, all the minimum temperature differences set to 1 °C and the internal heat exchanger efficiency of 0.50. In contrast, the specific set-up cost is very high (3.13 k€ kW⁻¹), due to the penalized heat transfer efficiency for this low reduced-pressure fluid, that leads to large required heat transfer surfaces. In fact, approximately 99% of the total specific costs are attributed to the heat exchangers (see Figure 29). Solution B represents the reasonable trade-off between low investment costs and high system performance. The corresponding set-up cost is 0.80 k€ kW⁻¹, significantly lower than that of solution C, with only a slight penalization on the COP value, equal to 0.39. For this configuration, ammonia (R717) is the working fluid and all the pinch point values are set to 1 °C, with an efficiency of the internal plate heat exchanger equal to 0.50. It is worth highlighting that the same heat exchanger typologies were selected for all fluids to preserve the analysis consistency. However, the higher evaporating pressures obtained for fluids having a high p-t saturation curve (as ammonia (R717)) may allow the use of a plate heat exchanger as low-pressure evaporator instead of a shell and tube heat exchanger. This would strongly reduce the set-up costs associated to this component (up to 80%) and increase the system compactness as well. Solutions A* and B* in Figure 28 and in Table 13 therefore refer to the corresponding simulations A and B, in which the low pressure evaporator is replaced by a less expensive plate heat exchanger. It is important to remark that the best design option is a matter of choice, once the desired criterion and potential further constraints are established (minimum cost – maximum performance – avoiding toxic and/or flammable refrigerants, etc.). The discussion regarding the rationale used to define the best configuration is therefore case-sensitive and is not included in the scope of this study.

The investment cost-performance map obtained in Figure 28 is placed together with the corresponding maps of existing waste heat driven technologies for cooling purposes in Figure 30. It is shown that the WHRHEC systems provide similar thermodynamic COP values and lower set-up costs with respect to ORC/VCC combined plants. As regards the comparison with single-effect absorption chillers, WHRHEC systems provide lower COP at the same costs. It is worth noting, however, that the declared performances of the consolidated technologies (as shown in the introductory section), even if falling in the same operative ranges of Table 11, are related to large plant sizes and cooling loads (> 100 kW), whereas the set-up costs of WHRHEC systems are likely not to be influenced by size effects.

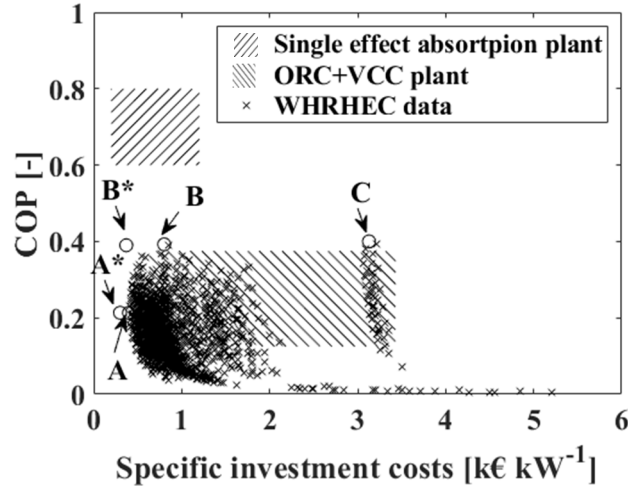


Figure 30. System performance and specific investment costs range of ORC+VCC and single effect absorption plant. Highlighted solutions: A (minimum cost), C (maximum performance) and B (best compromise between cost and COP). Asterisk solutions A* and B* refer to plate heat exchanger type at the low-pressure evaporator instead of a shell and tube heat exchanger.

4.4.1 Case study analysis

In this paragraph the result of the thermo-economic optimization is used to analyze the economic advantage of a waste heat recovery hybrid ejector cycle (WHRHEC) with respect to a typical vapor compression cycle (VCC). In particular, the analysis is focused on an end user with a required cooling load $\dot{Q}_{ev,user}$, supplied by having both WHRHEC (size $\dot{Q}_{ev,WHR}$ and designed according to Condition B) and a VCC (size $\dot{Q}_{ev,VCC}$) working in parallel, as shown in the schematic example of Figure 31. The aim of this economic analysis is to define a method able to establish the required life-time of the combined WHR/VCC system that leads to an economic convenience, once design and contingent parameters, such as the availability of the waste heat source, the specific cost of electric energy and the size of the WHR plant, are fixed.

The total costs TC of the integrated WHR/VCC plant for its entire life-time $\Delta\theta_{LIFE}$ include the investment costs of both systems and the running costs of the VCC plant due to the electrical energy consumption E_{el} . No running costs are here considered for the WHRHEC system, by keeping the hypothesis of free-of-charge availability of the waste heat.

$$TC = \dot{Q}_{ev,WHR} k_{WHR} + \dot{Q}_{ev,VCC} k_{VCC} + E_{el} k_{ee} \quad (4.33)$$

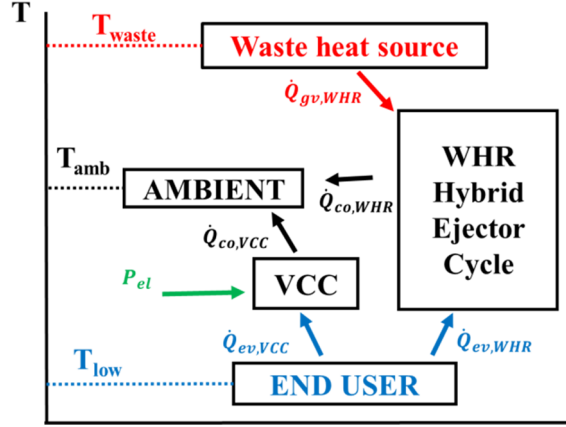


Figure 31. Schematic diagram of a combined WHRHEC/VCC system to supply the end user cooling load.

In Eq. (4.33), k_{WHR} and k_{VCC} are the set-up specific costs (k€ kW^{-1}) of the WHR and the VCC plant, respectively. Particularly, k_{WHR} refers to the optimal solution B of the previous section and is therefore considered equal to 0.80 k€ kW^{-1} in the present analysis. $\dot{Q}_{ev,WHR}$ and $\dot{Q}_{ev,VCC}$ are the cooling capacities of the two systems, whereas k_{ee} is the specific cost of electric energy (k€ kWh^{-1}). The VCC plant is most likely designed to fulfil the entire cooling load, in order to satisfy the user requirements also when the waste heat recovery mode is not available. The parameter X_{WHR} defines instead the fraction of the cooling load covered by the WHR plant.

$$\dot{Q}_{ev,VCC} = \dot{Q}_{ev,user} \quad (4.34)$$

$$X_{WHR} = \frac{\dot{Q}_{ev,WHR}}{\dot{Q}_{ev,user}} \quad (4.35)$$

The electric energy consumption E_{el} in the system life-time $\Delta\theta_{LIFE}$ is then required only when the waste heat recovery system is not used and is a function of the seasonal COP ($SCOP$) of the VCC cycle. By defining $\Delta\theta_{WHR}$ as the period of the lifetime in which the waste heat source is available, the electric consumption reads as:

$$E_{el} = \frac{Q_{ev,VCC}}{SCOP} = \frac{Q_{ev,user} - Q_{ev,WHR}}{SCOP} = \frac{\dot{Q}_{ev,user} \Delta\theta_{LIFE} - \dot{Q}_{ev,user} X_{WHR} \Delta\theta_{WHR}}{SCOP} \quad (4.36)$$

The total specific costs per unit of cooling load tc (k€ kW^{-1}) can be therefore expressed by Eq. (4.37), in which Y is the fraction of the total life-time period when the waste heat source is available, as for Eq. (4.38).

$$tc = \frac{TC}{\dot{Q}_{ev,user}} = X_{WHR}k_{WHR} + k_{VCC} + \frac{\Delta\theta_{LIFE}}{SCOP}(1 - X_{WHR}Y)k_{ee} \quad (4.37)$$

$$Y = \frac{\Delta\theta_{WHR}}{\Delta\theta_{LIFE}} \quad (4.38)$$

Eq. (4.39) provides the specific cost savings with respect to a simple configuration in which the WHRHEC is not considered and only the VCC plant fulfills the cooling load requirements ($X_{WHR} = 0$):

$$\Delta tc = X_{WHR} \left(\frac{\Delta\theta_{LIFE}}{SCOP} \cdot Y \cdot k_{ee} - k_{WHR} \right) \quad (4.39)$$

Figure 32(a) shows the cost savings Δtc as a function of the total lifetime of the combined system for different values of the parameter X_{WHR} . The fraction of the waste heat availability Y is fixed at 80%, whereas the Italian cost of the electric energy [101] and a $SCOP$ value of 2.5 are considered. It is worth noting that the size of the WHR plant does not influence the even point (zero-saving), approximately reached after almost 2 years (by considering 4000 hours of operation per year) within these hypotheses. A higher X_{WHR} leads however to higher savings after the even point and to higher losses for plants dismantled before the zero-saving time is reached. The effect of the waste heat availability Y for a fixed size of the WHR plant ($X_{WHR} = 0.5$) is shown in Figure 32(b). The economic convenience is more and more anticipated for higher waste heat availabilities. However, when Y is too low (e.g. 20%), the even point can be never reached in a reasonable lifetime (10 years).

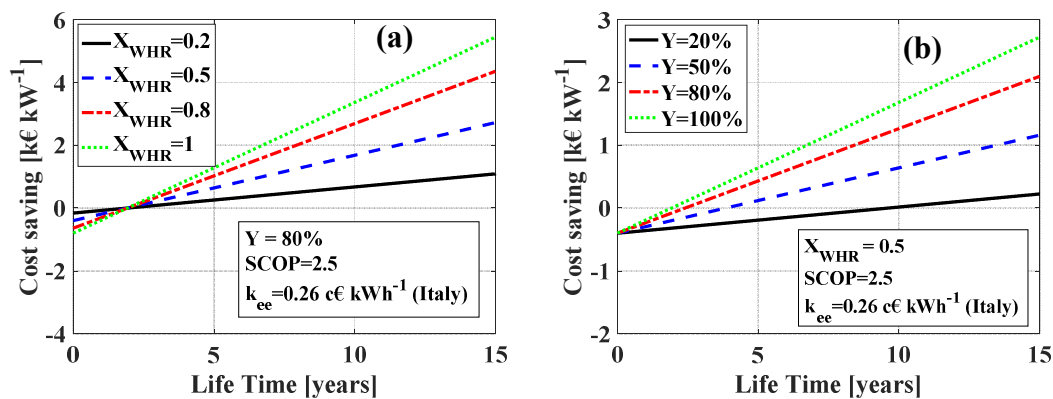


Figure 32. Specific cost savings as a function of the operating time of the combined plant (4000 working hours per year are considered). $SCOP$ and k_{ee} are respectively fixed to 2.5 and 0.14 c€ kWh⁻¹ (Italian market [101]). a) Effect of the WHR plant size for $Y = 0.80$; b) Effect of the waste heat availability for $X_{WHR} = 0.5$.

Figure 33 shows the required operating time to reach the even point ($\Delta tc = 0$) as a function of the waste heat utilization Y , with each curve referring to a different specific cost of energy k_{ee} [101]. For the Italian market, by considering a realistic lifetime of 7 years, the use of a WHRHEC/VCC integrated system would be economically convenient only if the availability of the heat source overcomes 28% (approximately 7800 hours) of the entire operating period. Higher values of Y are instead required in countries where the electric energy is cheaper (as France, with k_{ee} equal to 0.18 c€ kWh⁻¹).

Figure 34 presents the WHR size (X_{WHR}) – waste heat availability (Y) for the Italian market and an operating overall lifetime of 7 years, highlighting both loss and saving regions. As shown, the even point is reached for Y equal to 28% at any size of the WHR plant. For higher waste heat utilizations, the blue curves provide the specific savings, increasing with both WHR size and Y . Similarly, in the left zone the red curves show the specific losses, increasing with greater WHR size and lower waste heat availability.

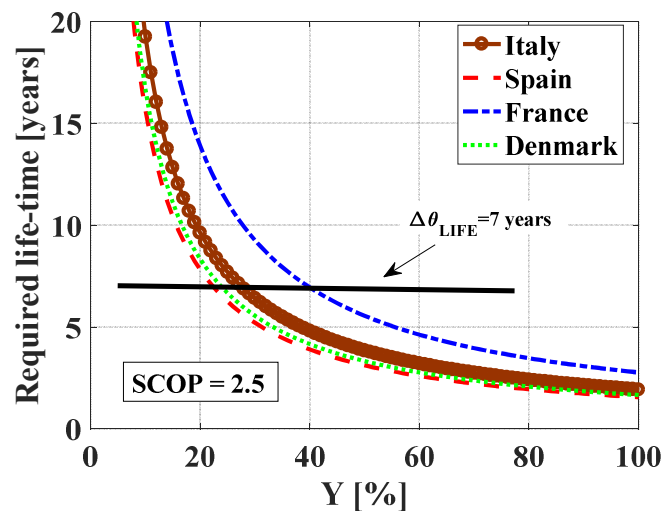


Figure 33. Required life-time ($\Delta tc = 0$) as a function of the waste heat availability Y , for different countries according to their specific cost of the electric energy. The horizontal line refers to a realistic operating time of 7 years.

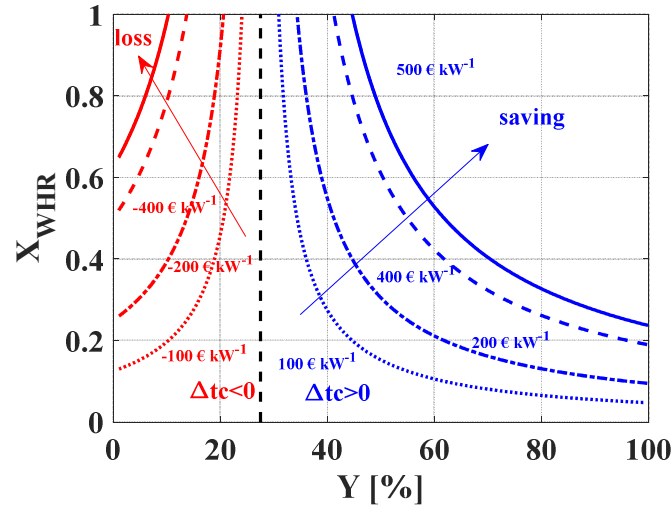


Figure 34. X_{WHR} - Y map developed for the Italian cost of the electric energy, by considering a total operating time of 7 years and a SCOP of the VCC plant equal to 2.5. The curves refer to either specific cost savings (in blue) or losses (in red).

4.5 Focus on two-phase heat transfer at high temperature for low GWP refrigerants

The temperature ranges of the low-temperature evaporator and condenser considered in the thermo-economic analysis showed in the previous paragraph are those typical of cooling systems. Therefore, the conventional correlations both for single and two-phase heat transfer considered for the heat transfer surface estimation are developed within these investigated ranges for the ejector cooling system. For this reason, no further investigation is needed. Differently, there is a lack of flow boiling data at high saturation temperature, as deeply investigated by Charnay [102].

According to the results showed in [102], new experimental data for two-phase flow especially for low GWP refrigerants are collected in this thesis. The thermo-economic analysis on WHRHEC showed that ammonia (R717), R1233zd(E), R1234ze, butane (R600) and propane (R290) are the best option as working fluids. Due to safety issues related to ammonia, experimental study on this fluid is not possible in our laboratory. The working fluid R1234ze was already studied in previous publications meanwhile butane is not available on the market. Therefore, R1233zd(E) and propane (R290) were investigated.

This paragraph shows the results from the experimental investigation on saturated flow boiling heat transfer of refrigerants R1233zd(E) and Propane (R290) in a stainless-steel

horizontal tube of 6.0 mm internal diameter are presented. The flow boiling two phase experiments were performed in a test facility already built in the Refrigeration Laboratory at the University of Naples “Federico II”. The details of the experimental apparatus, the data reduction and the experimental procedure are described in the following sections.

4.5.1 Test facility

The experimental setup [103] consists in a closed refrigerant loop shown in Figure 35 as a black line. The sub-cooled fluid is pumped to a preheating section, whose heat capacity is approximately 3.60 kW. The desired heat load is provided by four fiberglass heating tapes wrapped on the copper tube external surface, ensuring the evaporation of the fluid that enters into the test section with a specific and controlled vapor quality.

Before the measurement section, a suitable (> 60 diameters) horizontal adiabatic length is provided to let the fluid develop before the pressure drop and heat transfer coefficient measurements. The saturated flow is condensed in a plate heat exchanger and sub-cooled in a tube-in-tube heat exchanger before closing the loop. The control of the saturation temperature is assigned to a thermostatic bath and a demineralized water flow that feeds both the condenser and the sub-cooler by means of a secondary loop, which is displayed in blue in Figure 35.

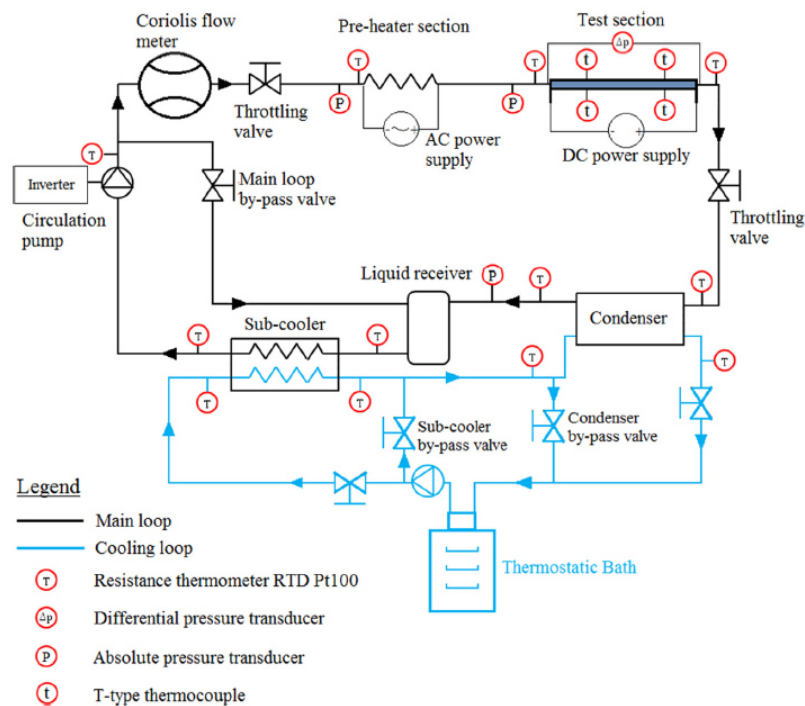


Figure 35. Representation of the test facility.

The main pump rotation speed is remotely controlled via inverter in order to adjust the refrigerant mass flow rate, which can be also varied by manipulating the throttling valves or by activating the main by-pass circuit, that recirculates part of the subcooled flow in a liquid receiver, thus avoiding the completion of the refrigerant loop. Other by-pass circuits are placed in the secondary loop to independently control the demineralized water flow in both heat exchangers. The whole test bench is covered by several layers of synthetic foam to minimize the heat transfer to/from the environment. Further details on the test facility are also available in previously published publications [104], [105], [106].

Test section

The test section (Figure 36) is a horizontal smooth stainless steel tube (AISI SS316) having an internal diameter d of 6.0 ± 0.05 mm and an outer diameter D of 8.0 ± 0.05 mm. The same tube has also been used for other published works [107].

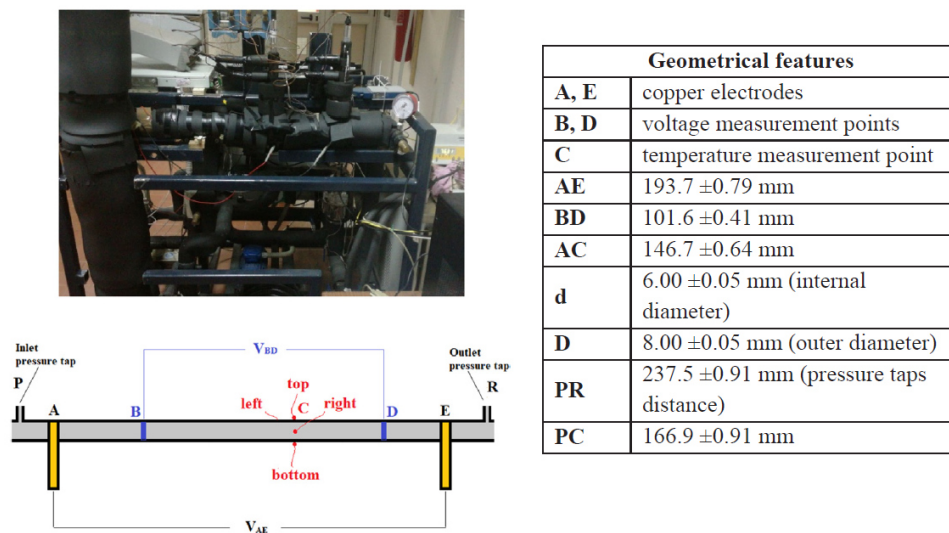


Figure 36. Test section illustration and its main characteristics.

The heat flux for the two-phase refrigerant flowing inside the tube is supplied by electrical heating of the tube itself, by means of a DC power generator (up to 8.0 V and 300 A) and two copper electrodes welded on the tube surface at a distance of 193.7 ± 0.79 mm. Two wires are then clamped inside the heated length (at positions B and D in Figure 36) for the evaluation of the imposed heat flux. The two-phase heat transfer coefficient is measured at a distance of 146.7 ± 0.64 mm from the first copper electrode (point C in Figure 36) by using 4 T-type thermocouples equidistantly glued on the external tube surface for a

fair estimation of the outer tube temperature distribution. A thin layer of epoxy resin at high thermal conductivity guarantees the contact between the four sensors and the tube, with the latter being previously covered with an adhesive Kapton layer for electrical insulation purposes. Two pressure taps are provided right outside the heated length (P and R in Figure 36, at a distance of 237.5 ± 0.91 mm) for the measurement of the pressure drop across the test section and the evaluation of the inlet absolute pressure.

Measurement instrumentation

Different RTDs are placed throughout the main and secondary loops for the measurement of the fluid temperature, carrying an overall uncertainty of ± 0.180 °C. The wall temperature measurements for the evaluation of the heat transfer coefficients are instead obtained with four T-type thermocouples, calibrated in-situ with two resistance thermometers and a thermostatic bath. The overall estimated uncertainty for these sensors, by taking into account also the residual errors of the calibration curve, is assumed to be ± 0.1 °C. The absolute pressure at the test section inlet is measured with an absolute pressure transducer having a measuring range of 0-35 bar and an overall uncertainty of $\pm 0.5\%$ of the read value. The pressure drop is instead estimated with a differential pressure transducer, calibrated in-situ with a water liquid column and a yardstick. The instrumental uncertainty is estimated to be ± 0.06 kPa. The mass flow rate is measured by means of a Coriolis flow meter, calibrated up to 2% of the full scale, with a maximum uncertainty of $\pm 1\%$ of the measurement. A digital wattmeter provides the heat applied to the preheater section, by separately measuring the voltage (100 mV-500 V) and current (1 mA-16 A). Its uncertainty is $\pm 1.0\%$ of the reading, as provided by the manufacturer. The heat flux applied to the test section requires the measurement of the DC voltage (electrical voltage transducer within 0-5 V and an uncertainty of $\pm 0.03\%$ of the reading) and the DC current (directly measured by the DC power unit within 0-300 A and an uncertainty of $\pm 1.0\%$).

Experimental procedure

The operating parameters in terms of mass flux, saturation temperature and heat flux are fixed at the beginning of each experiment, which starts from the onset of boiling and proceeds with increasing vapor quality up to the occurrence of dry-out, by means of the AC voltage applied to the fiberglass heating tapes of the preheater section. The test is stopped once the dry-out heat transfer is established (as soon as the heat transfer coefficient drops more than 25% from its previous value) and the wide wall temperature fluctuations would

not guarantee high-quality experimental data. The thermostatic bath control defines the saturation temperature of the system, whereas the inverter frequency of the electrical motor coupled with the magnetic gear pump changes the mass flow rate, which can be furtherly controlled by using the bypass circuit and/or the throttling valves on the liquid and vapor lines. The heat flux is imposed by setting the desired voltage of the DC power supply unit. All the data are obtained in steady state conditions (with the exception of the dry-out points in which the phenomenon itself is time-dependent), with a recording frequency of 1.0 Hz. The nominal values of each sample are the arithmetic average of the measured quantities over a recording time of 90 s. The system is considered stabilized when the calculated deviation of the main parameters is sufficiently low ($\pm 2\%$ for the mass velocity, ± 0.1 °C for the saturation temperature).

4.5.2 Experimental method

Data reduction

The local heat transfer coefficient and the imposed heat flux are evaluated as follows:

$$\alpha = \frac{q}{T_{wall} - T_{sat}} \quad (4.40)$$

$$q = \frac{V_{BD} \cdot I}{\pi d BD} \quad (4.41)$$

where the subscripts *wall* and *sat* refer to the inner wall temperature and the local saturation temperature, respectively. V_{BD} is the voltage applied in the section BD, I is the DC current flowing in the test tube and d is the channel internal diameter. The fluid saturation temperature at the measurement point is obtained by considering a linear pressure drop profile from the tube inlet. The wall temperature is instead evaluated from the measured wall outer temperature T_{th} by considering 1-D heat transfer and uniform generation in the metal tube having κ_{tube} ($16.26 \text{ W m}^{-1} \text{ K}^{-1}$) as thermal conductivity and D as external diameter:

$$T_{wall} = T_{th} + \frac{V_{BD} \cdot I}{4\pi\kappa_{tube} BD} \cdot \frac{\left(\frac{D}{d}\right)^2 \cdot \left(1 - \ln\left(\left(\frac{D}{d}\right)^2\right)\right) - 1}{\left(\frac{D}{d}\right)^2 - 1} \quad (4.42)$$

The cross-sectional average heat transfer coefficient shown in the results section is obtained by considering the average wall temperature from the four thermocouple measurements. The local vapor quality at the measurement point requires the knowledge of the local enthalpy, which is computable with an energy balance applied to the test section:

$$h = h_{in} + \frac{4 \cdot \overline{AC} \cdot q}{G \cdot d} \quad (4.43)$$

where G is the refrigerant mass flux and h_{in} is the test section inlet enthalpy, whose value is obtained from an energy balance applied to the preheater section, in which $h_{in,preh}$ is the preheater inlet enthalpy of the sub-cooled liquid, \dot{Q}_{preh} is the preheater load and \dot{m} is the refrigerant measured mass flow rate.

$$h_{in} = h_{in,preh} + \frac{\dot{Q}_{preh}}{\dot{m}} \quad (4.44)$$

All refrigerant thermodynamic properties are evaluated with the software Refprop 9.1 [24], whereas the whole data reduction is carried out with MATLAB software [23].

Uncertainty analysis and validation

The instrumental B-type uncertainties are composed to the standard deviation evaluated in the recording time for all the measured parameters. The uncertainty analysis of the derived results is then carried out by using the law of propagation of errors [25]. The maximum uncertainties are typically detected at the dry-out occurrence due to the higher fluctuations of the measured parameters. Lower uncertainty values are instead recorded during stable boiling. Table 14 shows the maximum and the average recorded uncertainty for the main operating parameters and results.

Table 14. Summary of uncertainty analysis.

Parameter	Average uncertainty		Maximum uncertainty	
	R290	R1233zd(E)	R290	R1233zd(E)
Saturation temperature T_{sat}	±0.04°C	±0.13°C	±0.08°C	±0.18°C
Mass flux G	±1.4%	±2.1%	±2.6%	±2.8%
Heat flux q	±0.68%	±0.70%	±0.71%	±0.74%
Vapor quality x	±0.03	±0.02	±0.11	±0.05
Mean heat transfer coefficient α_{mean}	±9.0%	±9.7%	±13%	±16%

The preheater and test section insulation and the correct functioning of the whole experimental apparatus have been checked with liquid single-phase experiments by using refrigerant R134a. The electrical power (from 220 to 1460 W in the preheater section and from 10 to 150 W in the test section) is compared to the heat absorbed by the sub-cooled refrigerant by means of two energy balances performed in the heated sections. In all tests, the wall and ambient temperatures reached similar values than those obtained during the flow boiling experiments. The liquid single-phase heat transfer coefficients for refrigerant R134a are also evaluated and compared to the well-known Dittus-Boelter prediction method [94]. Further detailed information on the validation procedure and results can be obtained from a previous work of the same authors with the same test facility [107].

4.5.3 Experimental results: effect of operating conditions on heat transfer coefficient

The experiments using propane (R290) are performed by changing the mass flux from 150 to 500 kg m⁻²s⁻¹, the heat flux from 2.5 to 40.0 kW m⁻² and the saturation temperature, which has been fixed to 25, 30 and 35 °C. In case of R1233zd(E), have been performed by varying the mass flux from 147 to 300 kg m⁻²s⁻¹, the heat flux from 2.4 to 40.9 kW m⁻² and the saturation temperature from 24.2 to 65.2 °C.

Tests have been taken from the onset of boiling up to high vapor qualities (0.70-0.90), in which the liquid phase is no longer in contact with the heated wall (dry-out), thus leading to a sharp deterioration of the heat transfer coefficient. The local vapor quality on the x-axis refers to the vapor quality evaluated at the measurement point C (see Figure 36). The error bands are related to the accuracy of the measurement instrumentation employed for the heat transfer evaluation, whereas the values of the operating parameters and their uncertainty shown in legends and titles are intended to be averaged over the represented data.

R1233zd(E)

The effect of the mass flux on the average heat transfer coefficient at a saturation temperature of 35°C, for a heat flux of 20 kW m⁻², is shown in Figure 37. The heat transfer coefficients present a typical convective behavior, with an increasing heat transfer coefficient trend with ongoing evaporation from a vapor quality approximately equal to 0.20 up to the occurrence of dry-out. The heat transfer performance is enhanced with increasing mass flux and for high vapor qualities. In these tests, the dry-out seems to occur

at slightly higher vapor qualities with increasing mass flux. In case of $G = 300 \text{ kg m}^{-2}\text{s}^{-1}$ and $q = 20 \text{ kW m}^{-2}$, the average heat transfer coefficient (see Figure 37) significantly drops right after the onset of dry-out. On the other hand, for the lowest mass velocity of $G = 150 \text{ kg m}^{-2}\text{s}^{-1}$, the drop of the average heat transfer coefficient after the dry-out inception is gentler, since the surface at the top dries at a vapor quality of approximately 0.78, quite earlier than the corresponding bottom part, in which the heat transfer coefficient falls when the vapor quality is about 0.88.

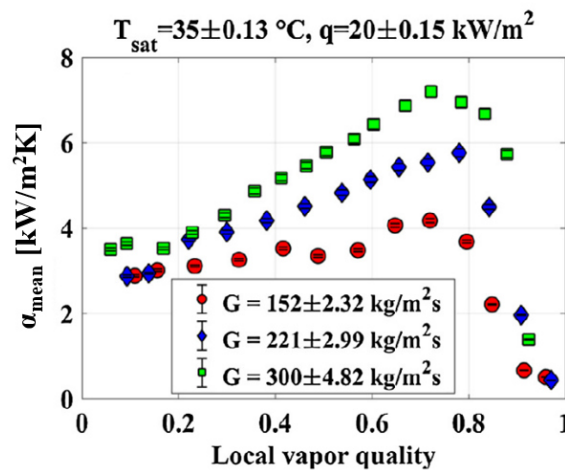


Figure 37. Effect of mass flux on mean heat transfer coefficients. Experiments performed at saturation temperature of 35°C and with an imposed heat flux of 20 kW m^{-2} .

Figure 38 shows the effect of the heat flux for a mass velocity of $300 \text{ kg m}^{-2}\text{s}^{-1}$ and at a fixed saturation temperature of 65°C . For low imposed heat fluxes of 2.5 and 10 kW m^{-2} , the usual convective behavior is observed. The higher imposed heat fluxes (20 and 40 kW m^{-2}), instead, determine a strong enhancement of average heat transfer coefficients, that exhibit also a strong nucleative boiling behavior, with minor influence of the local vapor quality. For the highest heat flux of 40 kW m^{-2} , instead, the effect of vapor quality disappears. As also observed at lower saturation temperatures, the dry-out phenomenon is gradually anticipated with increasing heat flux. The effect of the saturation temperature on the average heat transfer coefficients for a low imposed heat flux of 2.5 kW m^{-2} and medium/large mass fluxes of $220/300 \text{ kg m}^{-2}\text{s}^{-1}$ is negligible in the whole range of vapor quality. A remarkable effect of the saturation temperature at high vapor qualities is observed when the mass flux is $G = 300 \text{ kg m}^{-2}\text{s}^{-1}$ and the imposed heat flux is 10 kW m^{-2} .

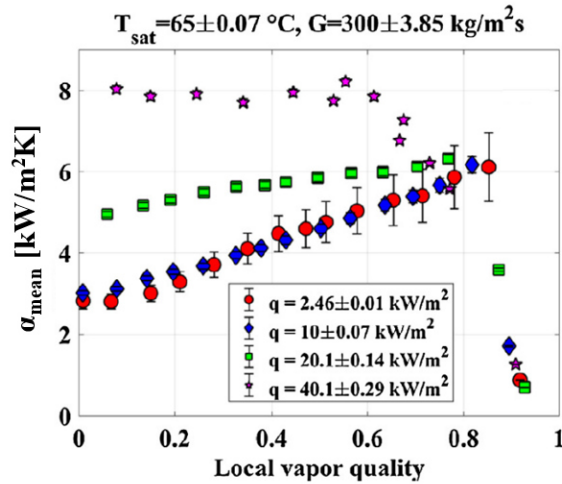


Figure 38. Effect of heat flux on mean heat transfer coefficients. Experiments performed at saturation temperature of 65°C and with a mass flux of 300 kg m⁻²s⁻¹.

The average heat transfer coefficients for saturation temperatures from 24.9 up to 64.8°C are shown in Figure 39: up to a vapor quality of 0.20, with increasing saturation temperature the mean heat transfer coefficient presents a slight enhancement, which is observed at 65 °C. For higher vapor qualities, instead, the heat transfer coefficient is penalized with increasing reduced pressure. By increasing the saturation temperature (i.e. reduced pressure), the most important thermophysical property variation is that of the density, which increases leading to a reduction of the fluid mean velocity for a fixed mass flux. For higher vapor qualities the reduction of the fluid mean velocity prevails thus penalizing the heat transfer coefficient, which is lower for the highest saturation temperature of 65 °C.

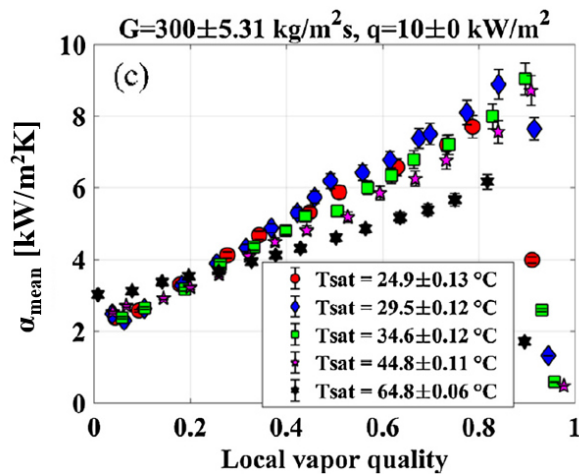


Figure 39. Effect of saturation temperature on mean heat transfer coefficients. Experiments performed at a mass flux of 300 kg m⁻²s⁻¹ and with an imposed heat flux of 10 kW m⁻².

Propane (R290)

Figure 40 shows the effect of the mass flux (from 149 up to 497 kg m⁻²s⁻¹) on the local heat transfer coefficients of propane, for two different saturation temperatures and imposed heat fluxes.

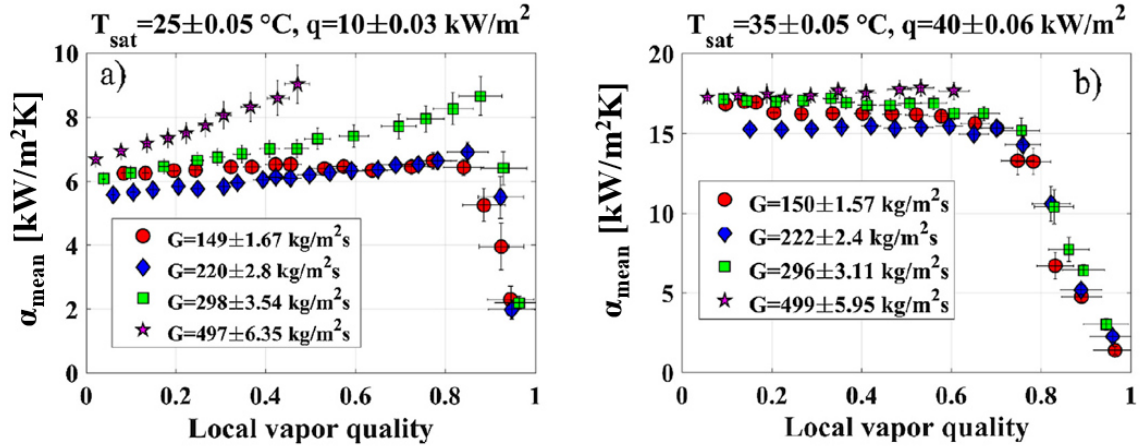


Figure 40. Effect of the mass velocity on the local heat transfer coefficient. (a) $T_{sat} = 25\text{ °C}$ and $q = 10\text{ kW m}^{-2}$. (b) $T_{sat} = 35\text{ °C}$ and $q = 40\text{ kW m}^{-2}$.

At $T_{sat} = 25\text{ °C}$ and $q = 10\text{ kW m}^{-2}$ (see Figure 40a), the heat transfer coefficients present a slightly increasing trend with vapor quality, which is more evident for higher mass fluxes. In case of $G = 149\text{ kg m}^{-2}\text{s}^{-1}$, the heat transfer coefficient remains substantially the same (about $6.2\text{ kW m}^{-2}\text{K}^{-1}$) from low vapor qualities up to the dry-out occurrence. At $G = 298\text{ kg m}^{-2}\text{s}^{-1}$, instead, the heat transfer performance increases from 6.1 up to $8.3\text{ kW m}^{-2}\text{K}^{-1}$, showing an increasing rate higher than +38%. Apart from the change of trend with vapor quality, the influence of mass flux on the overall heat transfer performance is not particularly significant. For a fixed vapor quality of 0.4, the heat transfer coefficients remain in the range $6.2\text{--}7.2\text{ kW m}^{-2}\text{K}^{-1}$ when the mass velocity is changed from 149 to 298 $\text{kg m}^{-2}\text{s}^{-1}$. Higher values (about $8.3\text{ kW m}^{-2}\text{K}^{-1}$) are recorded for the highest mass flux of $497\text{ kg m}^{-2}\text{s}^{-1}$. For a higher saturation temperature of 35 °C and a higher imposed heat flux of 40 kW m^{-2} (see Figure 40b), all the heat transfer coefficients remain the same with ongoing evaporation and they are not significantly affected by a change of mass flux.

Figure 41 shows the effect of the saturation temperature on the local heat transfer coefficient as a function of the vapor quality, for two different operating conditions in terms

of mass flux and heat flux. Specifically, the effect of the saturation temperature at $G = 300$ $\text{kg m}^{-2}\text{s}^{-1}$ and $q = 10$ kW m^{-2} is shown in Figure 41a.

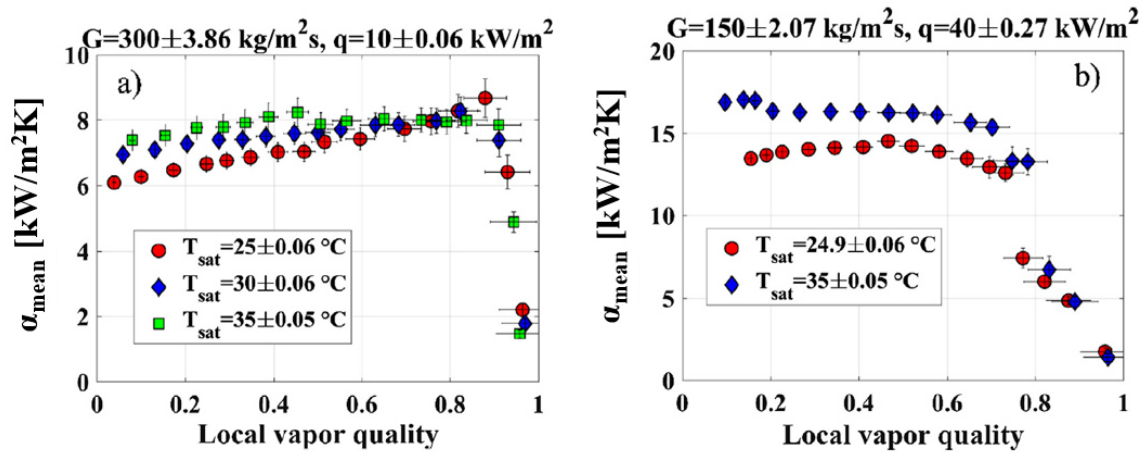


Figure 41. Effect of the saturation temperature on the local heat transfer coefficient. (a) $G = 300$ $\text{kg m}^{-2}\text{s}^{-1}$ and $q = 10$ kW m^{-2} . (b) $G = 150$ $\text{kg m}^{-2}\text{s}^{-1}$ and $q = 40$ kW m^{-2} .

The increasing trend of the heat transfer coefficient with vapor quality is more evident only for the lowest saturation temperature of 25 °C. Moreover, up to a vapor quality of 0.50, the saturation temperature positively changes the heat transfer coefficients, that increase of approximately +20% when passing from 25 to 35 °C. With ongoing evaporation at higher vapor qualities up to the occurrence of dry-out, the different curves blend each other and small differences between heat transfer coefficients at varying saturation temperature fall within the uncertainty bands. The effect of the saturation temperature at low mass flux ($G = 150$ $\text{kg m}^{-2}\text{s}^{-1}$) and high heat flux ($q = 40$ kW m^{-2}) is shown in Figure 41b. In these conditions, the heat transfer coefficients present a constant trend with vapor quality from the onset of boiling up to the dry-out incipience. The curve at 35 °C is higher (approximately +25%), suggesting a stronger influence of the saturation temperature when the operating conditions promote the nucleate boiling mechanism. The heat flux is the operating parameter that mostly affects the heat transfer coefficient experimental results. Its effect is shown in Figure 42 for two different values of the mass flux and the saturation temperature. Particularly, Figure 42a presents the local heat transfer coefficients with a varying heat flux from 2.48 up to 40 kW m^{-2} .

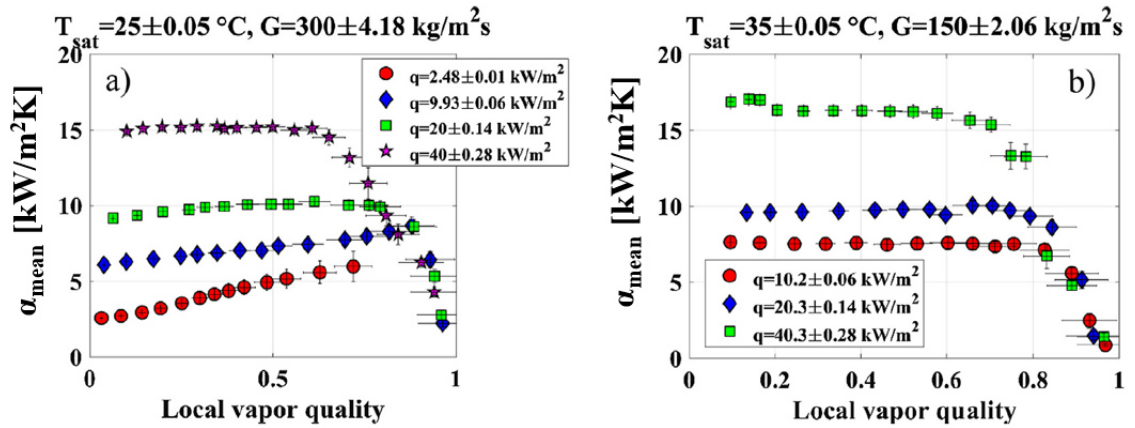


Figure 42. Effect of the heat flux on the local heat transfer coefficient. (a) $T_{sat} = 25\text{ }^{\circ}\text{C}$ and $G = 300\text{ kg m}^{-2}\text{s}^{-1}$. (b) $T_{sat} = 35\text{ }^{\circ}\text{C}$ and $G = 150\text{ kg m}^{-2}\text{s}^{-1}$.

The heat transfer coefficients are strongly enhanced with higher imposed heat fluxes: at a vapor quality of 0.20, the heat transfer performance passes from 2.8 up to 15.1 $\text{kW m}^{-2}\text{K}^{-1}$ (increasing of +440%). In addition, the curves trend with vapor quality changes with increasing heat flux. At $q = 2.48\text{ kW m}^{-2}$ the heat transfer coefficient presents a significant increase with vapor quality, passing from 2.5 $\text{kW m}^{-2}\text{K}^{-1}$ at the onset of boiling up to approximately 6.0 $\text{kW m}^{-2}\text{K}^{-1}$ when dry-out occurs. This increasing rate is more and more suppressed with augmenting the imposed heat flux: at $q = 40.2\text{ kW m}^{-2}$, the heat transfer coefficient does not change anymore up to the dry-out condition, which occurs anyway at a lower vapor quality when compared to the other data in the same diagram. The effect of heat flux at a saturation temperature of 35 °C and a mass flux of $G = 150\text{ kg m}^{-2}\text{s}^{-1}$ is instead presented in Figure 42b. In these conditions the heat transfer coefficient trend is almost constant with ongoing evaporation regardless the value of the local vapor quality. Also, in this case, the heat flux strongly increases the heat transfer coefficients, that pass from approximately 7.5 to 15.7 $\text{kW m}^{-2}\text{K}^{-1}$ when the imposed heat flux goes from 10.2 to 40.3 kW m^{-2} .

4.5.4 Assessment with prediction methods by literature

The collected experimental data were used to evaluate the goodness of the prediction of Park and Kim correlation [90], which has been used in the WHRHEC simulations to estimate the flow boiling heat transfer coefficient in a plate heat exchanger, in operating conditions similar to those occurring in the simulations. In particular, experimental tests characterized by mass flux of $150\text{ kg m}^{-2}\text{s}^{-1}$ and heat flux of 10 kW m^{-2} at the higher

investigated saturation temperature (35°C for the propane and 65°C for the R1233zd(E)) are considered. Although the experimental data are related to smooth circular tube, the correlation of Park and Kim [90], developed for plate heat exchangers, considers the effect of different geometries by using the hydraulic diameter. In the assessment a modified version of the flow pattern based method of Wojtan et al. [108] is also implemented. Figure 43a-b shows the comparison between the experimental trend and the evolution of the heat transfer coefficient with local vapor quality calculated by the chosen correlations, for each investigated fluid. The trends evaluated by Park and Kim correlation [90] are monotonically rising with vapor quality; however it predicts the heat transfer coefficient with a good agreement for both of fluids. High differences with respect to experimental data are observed in the estimation of the vapor quality corresponding to the dry-out condition due to the fact that experimental data are related to horizontal tubes meanwhile in a plate heat exchanger the flow direction is vertical. Considering that the effect of the dry-out is very limited for vertical flows the correlation of Park and Kim [90] was used in the simulations described in the previous paragraphs without any modification.

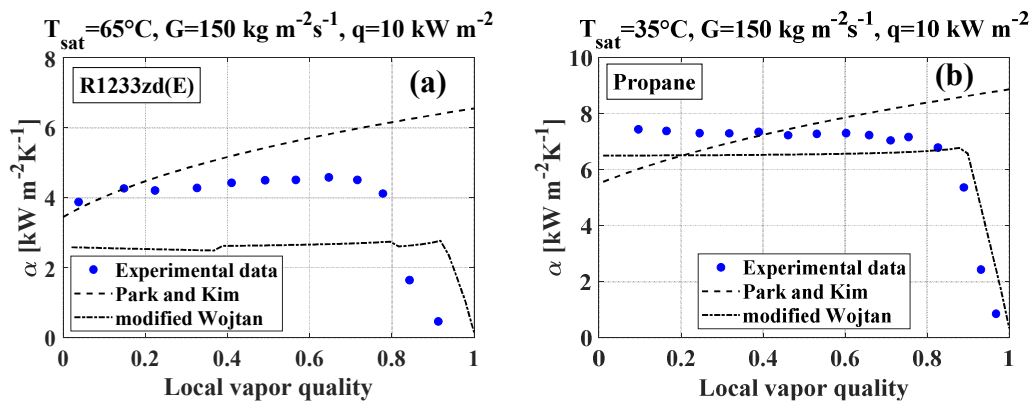


Figure 43. Experimental versus predicted heat transfer coefficient trends with vapor quality. (a) R1233zd(E) at $T_{\text{sat}} = 65^\circ\text{C}$, $G = 150 \text{ kg m}^{-2}\text{s}^{-1}$, $q = 10 \text{ kW m}^{-2}$. (b) Propane at $T_{\text{sat}} = 35^\circ\text{C}$, $G = 150 \text{ kg m}^{-2}\text{s}^{-1}$, $q = 10 \text{ kW m}^{-2}$.

4.6 Main outcomes of the chapter

A thermo-economic analysis of a waste heat recovery hybrid ejector cycle (WHRHEC) for air conditioning purposes was performed in the first part of this chapter, in order to place the WHRHEC systems among the actual heat driven cooling technologies available on the market. Due to the shortage of two-phase heat transfer data of refrigerants at high saturation temperature in open literature, the second part of this chapter presents an experimental in-depth analysis on flow boiling heat transfer of propane (R290) and

R1233zd(E) at 25-65°C, being typical fluids and operating conditions occurring in ejector waste heat driven cooling systems. The main outcomes are summarized here.

4.6.1 Summary of the WHRHEC thermo-economic analysis

The thermodynamic performances and the specific set-up costs for different cycle configurations in terms of working fluids and pinch point values at the heat exchangers were performed. The following economic analysis will give the reader a realistic order of magnitude about the economic convenience in the use of the WHRHEC systems instead of traditional vapor compression cycles, when a certain amount of waste heat is available. The main outcomes of this study may be summarized as follows:

- WHRHEC solutions employing Ammonia (R717) as working provide the best performance and are also economically advantageous, due to the Ammonia high latent heat and favorable thermodynamic and transport properties during two-phase heat transfer. Regarding economic considerations, the higher low-temperature evaporating pressures may allow the use of more compact plate heat exchanger instead of a tube and shell low-temperature evaporator, thus further reducing the set-up costs.
- The cost-performance comparison with existing waste heat driven technologies for cooling purposes shows that the WHRHEC systems provide similar performances and lower investment costs with respect to ORC/VCC combined plants; instead WHRHEC systems give lower COP values at the same costs of single-effect absorption chillers. However, the declared performances of the consolidated technologies are related to large plant sizes and cooling loads (> 100 kW), while costs of WHRHEC systems is not affected by size effects. This could give a major perspective of application of WHRHEC systems in small applications, potentially driven by heat produced by solar energy.
- The economic analysis has shown that a WHRHEC may be a convenient solution to be integrated with a conventional VCC system in a plant according to the specific cost of electric energy and the waste heat time availability. Specifically, for the Italian situation, by considering a total life-time of 28000 hours (7 years and 4000 hours per year of operation), the economical convenience of the WHRHEC system is reached when the waste heat exploitation overcomes approximately 7800 hours (28% of the entire life-time).

Higher (lower) waste-heat availability periods are instead required where the cost of electric energy is lower (higher), as in France (40%) (as in Spain, 24% and Denmark, 26%).

4.6.2 Summary of the experimental results on flow boiling heat transfer at high temperature

Different flow boiling tests were performed with refrigerants R1233zd(E) and propane (R290) by varying mass velocities from 150 to 300 kg m⁻²s⁻¹ (up to 500 kg m⁻²s⁻¹ for R1233zd(E)), saturation temperature from 25 to 35 °C (up to 65 °C for R1233zd(E)) and heat fluxes from 2.5 to 40 kW m⁻². The experimental results showed that:

- In case of Propane (R290), the effect of the mass flux on the experimental heat transfer coefficients is negligible for almost all the experiments performed. A slight influence can be seen at low heat fluxes and saturation temperatures.
- In case of R1233zd(E), the effect of the saturation temperature during convective boiling at large vapor qualities the velocity reduction corresponding to the vapor density increase penalizes the heat transfer performances, when the convective contribution is significant. This behaviour has been observed for the highest investigated mass fluxes ($G=300 \text{ kg m}^{-2}\text{s}^{-1}$). Instead, when considering Propane (R290), the effect of saturation temperature on the heat transfer coefficient is dependent on the operating conditions. At high mass fluxes and low heat fluxes, an increase of the saturation temperature leads to higher heat transfer performances only for low vapor qualities ($x < 0.5$). At low mass fluxes and high heat fluxes, instead, the effect of saturation temperature is remarkable from the onset of boiling up to the occurrence of dry-out.
- In case of Propane (R290), the heat flux has a significant effect on the experimental heat transfer coefficients, at any operating condition investigated. The heat transfer coefficient trend with local vapor quality is also influenced: by increasing the imposed heat flux, the effect of the vapor quality becomes less and less significant. Meanwhile, in case of R1233zd(E) the effect of heat flux: at large saturation temperature (65°C) a strong nucleate boiling contribution seems to be triggered at a mass flux of 300 kg m⁻²s⁻¹ for a heat flux larger than 20 kW m⁻². At these conditions, the heat transfer coefficient trend at

the bottom becomes gradually independent on vapor quality with increasing heat flux.

5 Design of a heat driven ejector cycle prototype

The simulation results on the waste heat recovery hybrid ejector cycles (WHRHEC) described in the previous chapter pointed-out the possible convenience in the use of a heat driven ejector cooling cycle especially for small size applications. However, from the analysis of the current scientific literature showed in the Chapter 4, there are just three experimental works. In order to quantify the performance of heat driven ejector cooling systems, a prototype was designed. In the following sections, the experimental lay-out and the components sizing procedure are explained in detail.

5.1 Experimental rig description

The schematic lay-out of the hybrid ejector cycle is shown in Figure 44. The refrigerant flow path is portrayed in with a black line, meanwhile the water flows into the secondary loop, which is portrayed as a blue line, feeding both the sub-cooler and the condenser. To enable the ejector system to work under operating conditions giving low entrainment ratio, a compressor is employed in parallel to the ejector line. The compressor is equipped by an inverter able to modulate the frequency within a range $10\div 100\%$ with respect to the nominal value. The use of the compressor makes the system feasible to work in three different operating modes, by acting on the solenoid valves across the lay-out: if the compressor is excluded, the prototype works as waste heat ejector cooling cycle (thick green line in Figure 45); when the compressor runs, it is in parallel to the ejector (thick blue line in Figure 45); the high pressure line and the ejector can be excluded and the system is able to work as a conventional vapor compression cycle (thick red line in Figure 45).

Two tanks are used to simulate the thermal load at the low and high-pressure evaporators. The heat power was provided by varying the supplied voltage of cartridge ceramic heaters placed on the bottom side of the tanks. Another tank works as condenser using water in the secondary loop to condense the flow at the exit of the ejector (or the compressor, according to the operation mode). The same water circuit is used to obtain the subcooling after the condenser, through a shell and tube heat exchanger. A volumetric flow meter is used to measure the amount of refrigerant flowing into the circuit. With the aim to measure the total flow rate as well as the flow rate flowing at each evaporator, the flow meter is supplied by two collectors able to manage the three flow rates alternatively, by using several solenoid valves controlled by an algorithm. A refrigerant pump compresses

the primary flow to from the condenser to the vapor generator pressure. In order to obtain a fine regulation of the flow rate, the pump is equipped by an inverter; also, a by-pass circuit with a modulating three-way valve is used.

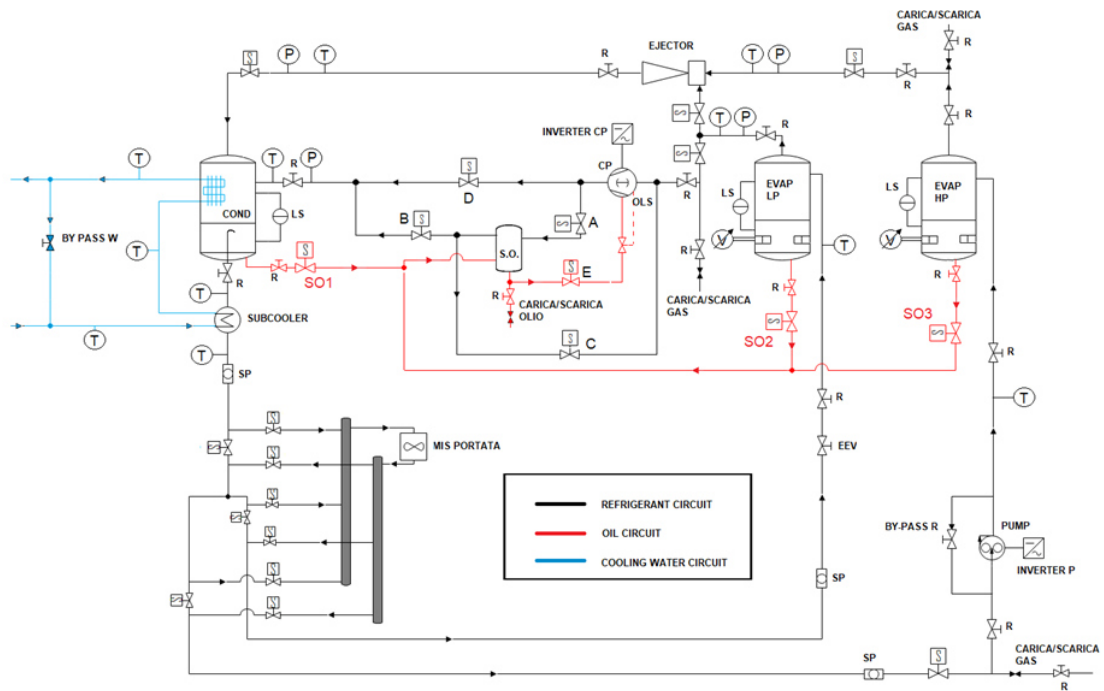


Figure 44. Schematic layout of the hybrid ejector cooling cycle experimental apparatus.

In order to separate the lubricant oil from the refrigerant flow, a dedicated oil circuit is developed, portrayed as a red line in Figure 44. The oil circuit removes the lubricant from the bottom side of each tank which represents the most critical point in terms of oil deposition. Due to the fact that each tank works at a specific pressure, a time regulating algorithm will be implemented: by acting on the opening time of the solenoid valves SO1, SO2 and SO3 (as indicated in the layout in Figure 44) one tank at a time will be in connection with the oil separator. An oil management system is able to electronically control the system with an integrated solenoid valve, which feeds the missing oil directly into the compressor.

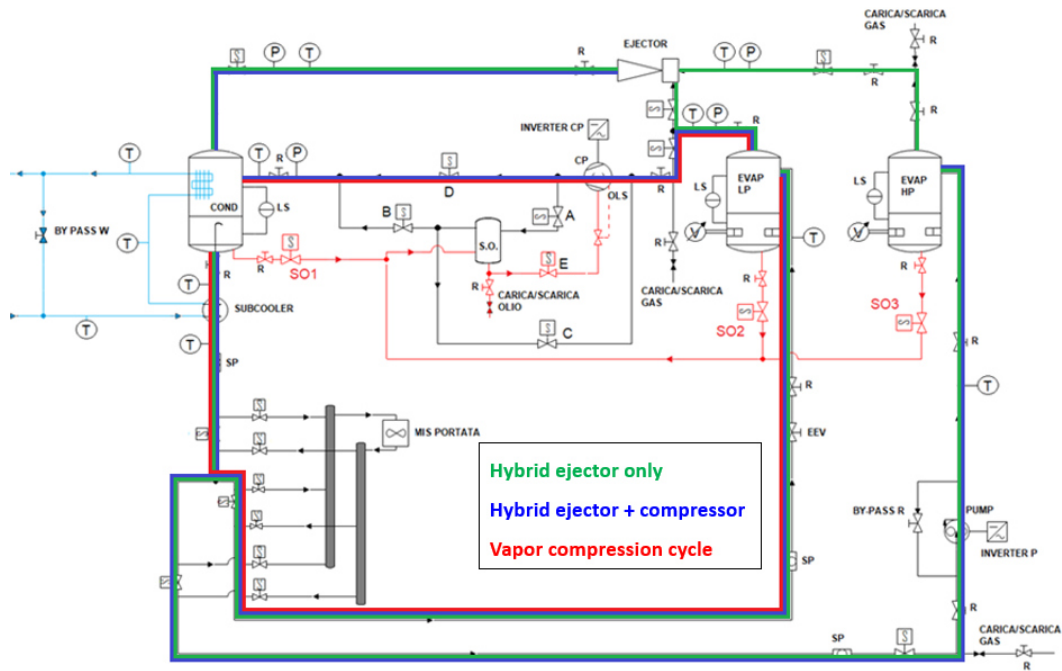


Figure 45. Operating modes of the hybrid ejector cooling cycle experimental apparatus.

5.2 Components selection and sizing

The prototype design process started with the compressor sizing. Once the compressor model was selected, a calibrated model of the component was developed in terms of global efficiency and volumetric flow rate. The operating domain of the other components (liquid pump, expansion valve, low and-high pressure evaporators) are calculated by simulating the hybrid ejector cycle when the compressor runs at minimum and maximum load. The simulations considered R134a, R1233zd(E), R1234ze and R245fa as working fluids, by varying the vapor generator temperature within a range of 50÷130°C and the evaporation temperature within a range of -10÷10°C. A fixed condensing temperature of 20°C was considered, due to the thermal stability of the water flow. Furthermore, to a better functioning of the expansion device, a subcooling of 5 K was considered. To avoid condensation during the expansion process of the secondary flow inside the ejector, a superheating of 5 K was considered. The operating domain was evaluated by fixing the limits in terms of compressor frequency and, hence, volumetric flow rate. The maximum volumetric flow rate corresponds to a compressor frequency of 60 Hz (+20% with respect to the nominal frequency); instead, the minimum value corresponds to 20% of the maximum one (compressor frequency at 12 Hz). These limits are considered in the

following design steps to determine the operating conditions of the other components. The simulated operating conditions are summarized in Table 15.

Table 15. Summary of the operating conditions used for the components sizing.

Fluids	R134a – R1233zd(E) – R1234ze – R245fa
Vapor generator temperature	50÷130 °C
Evaporation temperature	-10÷10 °C
Condenser temperature	20 °C
Subcooling at condenser outlet	5 K
Superheating at evaporator outlet	5 K
Maximum compressor frequency	60 Hz
Minimum compressor frequency	12 Hz

5.2.1 Compressor

To find the compressor size, a nominal heat load at the generator of 5 kW was assumed. According to the state of the art related to waste heat driven ejector cooling system, a COP of 0.5 was considered as reference, leading to a cooling capacity of 2.5 kW. The evaporating and condensing temperature of -5 °C and 20°C were considered as operating conditions, respectively. All the design conditions are listed in Table 16.

Table 16. Compressor operating conditions design.

Heat load at vapor generator	5.0 kW
COP	0.5
Cooling load at evaporator	2.5 kW
Condensing temperature	20 °C
Evaporation temperature	-5 °C
Subcooling at condenser outlet	5 K
Superheating at evaporator outlet	5 K
Fluid	R134a

According to the design conditions as in Table 16, once the thermodynamic properties at the inlet and the outlet of the evaporator (corresponding to the compressor inlet), the mass flow rate can be evaluated by an energy balance on the evaporator, being the cooling load fixed. Finally, the volumetric flow rate required by the compressor (4.25 m³h⁻¹) was obtained.

To avoid large use of lubricant oil, a scroll type compressor was selected; according to the nominal volumetric flow rate, the model ZS13KAE, provided by Copeland, was selected. From the datasheet of the manufactures, a simulation model of the compressor was calibrated in order to simulate the whole operative range to size the other components. The related correlations are reported in Eqs. (5.1), (5.2). Figure 46 shows the global efficiency and the volumetric flow rate trends of the selected component as function of the compression ratio.

$$\eta_g = -2812 \cdot \beta^{8.544} + 0.5493 \quad (5.1)$$

$$\dot{V}_{cp} = -0.0747 \cdot \beta + 5.0902 \quad (5.2)$$

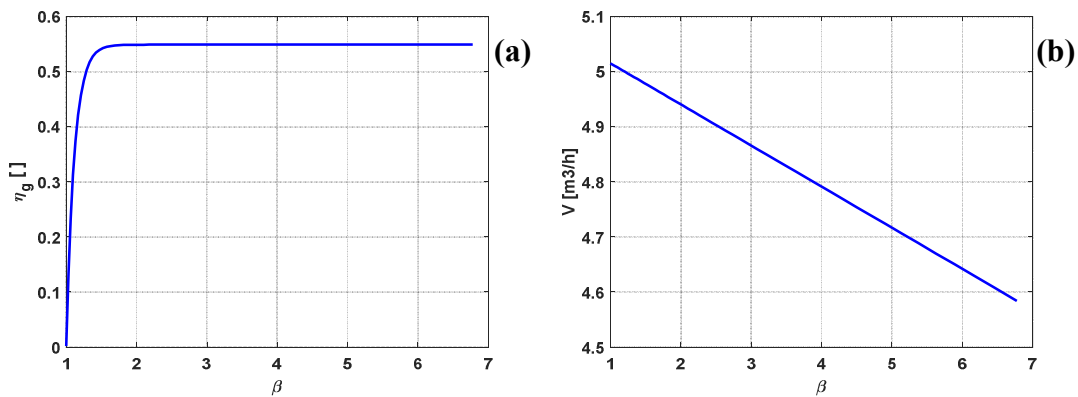


Figure 46. (a) Global efficiency and (b) volumetric flow rate as function of compression ratio.

The whole range of operating conditions reported in Table 15 are then simulated by using the abovementioned model. Figure 47 shows the compressor operating map, for the investigated working fluids and at minimum and maximum frequency. A photograph of the compressor is showed in Figure 48a. Once the size of the compressor is known and, hence, the required oil charge, the oil separator was chosen. A high efficiency oil separator (SO-ISC-ODS 22/OD 33, provided by Frigomec and showed in Figure 48b) was selected; the use of coalescent cartridge with high filtration degree allows the separator to reduce up to 99% the oil pulling. A photograph of the oil management system (TraxOil OM3, provided by Emerson) is showed in Figure 49.

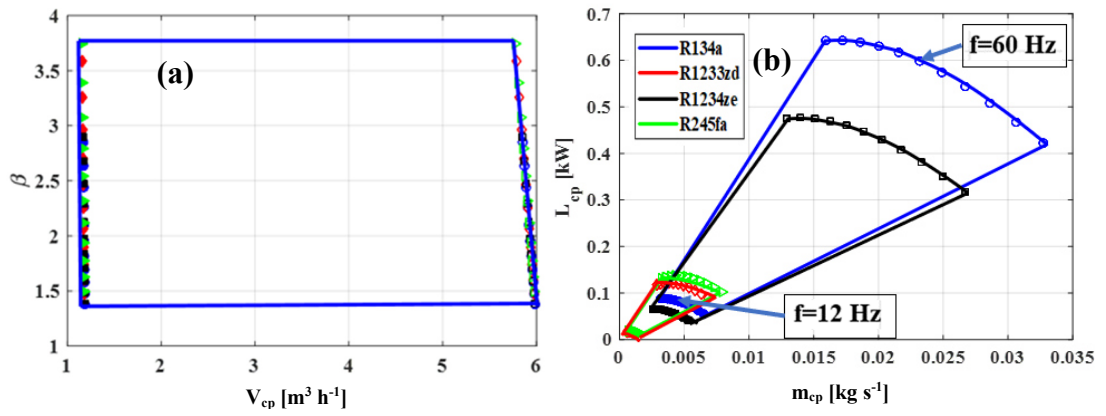


Figure 47. (a) Compressor operating map in terms of compression ratio and volumetric flow rate. (b) Electric power required by the compressor as a function of mass flow rate, at the minimum and maximum compressor frequency.



Figure 48. Copeland scroll compressor ZS13KAE. (b) Oil separator.



Figure 49. Traxoil – oil system management.

5.2.2 Low and high-pressure evaporators

Figure 50 and Figure 51 show the thermal load at the low and high-pressure evaporators as a function of the corresponding temperatures. Due to the high mass flow rate when the compressor runs at frequencies close to the maximum value, the thermal load is high especially for fluids such as R1234ze and R134a. Due to the structural limit of the laboratory, the overall electrical load must be limited to 9 kW. By considering a design COP of 0.5 as reported in Table 16, the limits for the low temperature evaporator and the high temperature evaporator are 3 kW and 6 kW, respectively, as shown in Figure 50 and Figure 51. It is worth noting that R134a and R1234ze require higher thermal load with respect to other fluids, thus limiting their possible operating conditions. The tanks are provided by Klimal and designed ad-hoc for this application and showed in Figure 52.

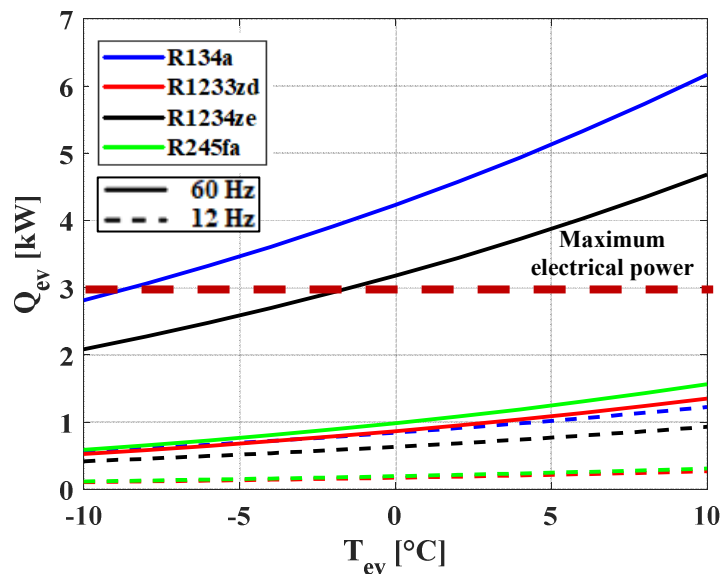


Figure 50. Thermal load at the low-pressure evaporator as function of the evaporation temperature.

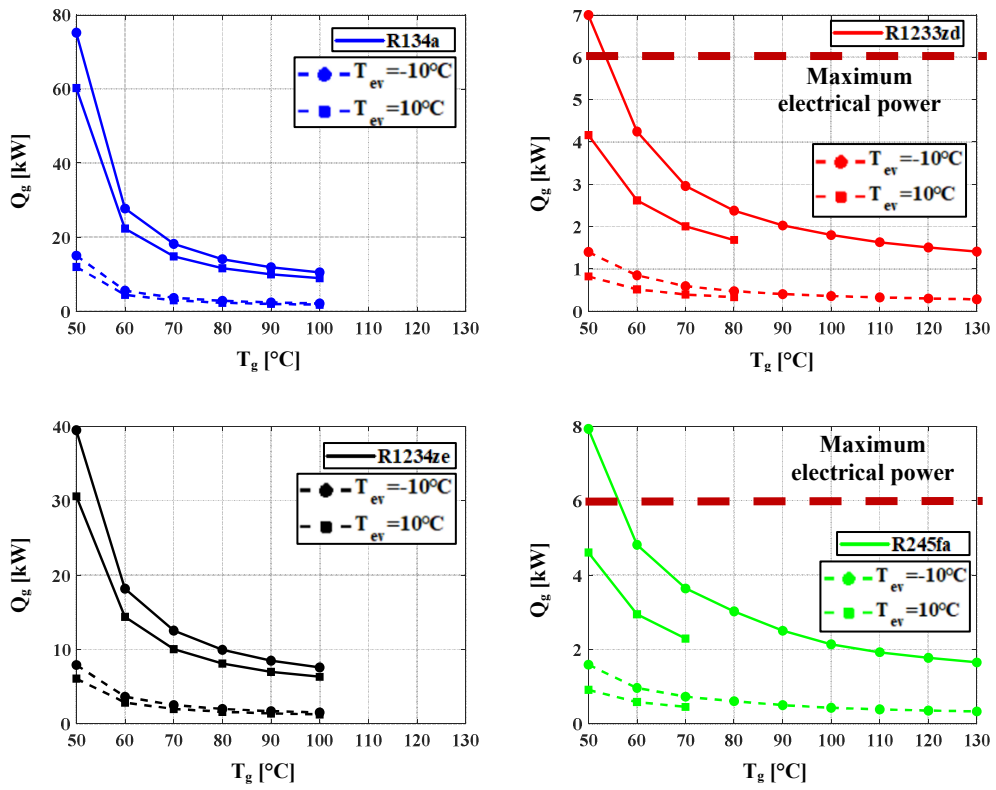


Figure 51. Thermal load at the high-pressure evaporator as function of the vapor generator temperature, for each investigated working fluid.



Figure 52. Photograph of the tank working as evaporator.

5.2.3 Condenser

The condenser was sized considering the design conditions listed in Table 17, considering the refrigerant R1234ze as working fluid. A maximum operating pressure of 25 bar and a thermal load of 10.5 kW were considered. Starting from the design operating conditions, the heat exchanger was sized: a sketch is shown in Figure 53 meanwhile, a photograph of the component is reported in Figure 54.

Table 17. Condenser design conditions.

Parameters	R1234ze (working fluid)	Water (secondary fluid)
inlet temperature	40.7°C	13°C
outlet temperature	20°C (liquid in saturated condition)	15°C
inlet specific enthalpy	417.4 kJ kg ⁻¹	-
maximum pressure	25 bar	
thermal load	10.5 kW	

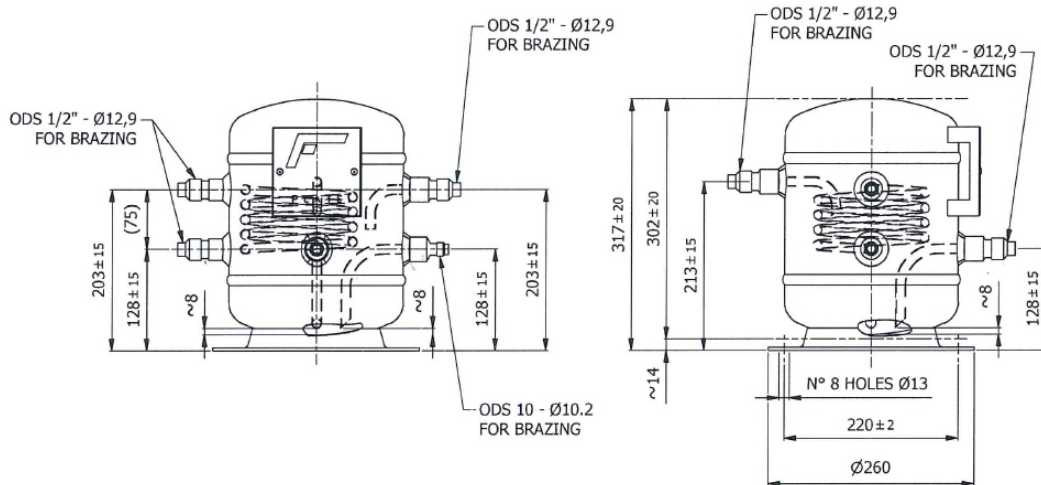


Figure 53. Sketches of the condenser.



Figure 54. Photograph of the tank working as condenser.

5.2.4 Sub-cooler

The shell and tube heat exchanger working as sub-cooler was sized considering the design conditions listed in Table 18, considering the refrigerant R1234ze as working fluid, Starting from the design operating conditions, the heat exchanger was sized: a sketch is shown in Figure 55 meanwhile, a photograph of the component is reported in Figure 56.

Table 18. Shell and tube design conditions.

Parameters	R1234ze (working fluid)	Water (secondary fluid)
mass flow rate	0.21 kg s ⁻¹	0.068 kg s ⁻¹
inlet temperature	20°C (liquid in saturated condition)	13°C
outlet temperature	15°C (liquid in subcooled condition)	18°C

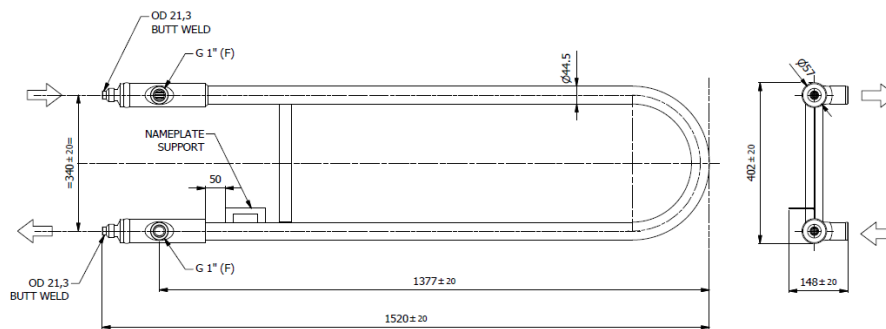


Figure 55. Sketches of the sub-cooler.



Figure 56. Shell and tube heat exchanger – sub-cooler.

5.2.5 Electrical heaters

A schematic representation of the tank working as evaporators is shown in Figure 57. Four cartridge electrical heaters are located into the bottom side of each tank, which is made of carbon steel. For this application, FIREROD Nickel chromium cartridge heaters, each of them with a maximum power of 2 kW, provided by Watlow, are chosen. This device includes a K-type thermocouple to monitor its temperature and possible cut-off the electrical supply in case of undesired overheating. A photograph of the cartridge heaters is shown in Figure 58.

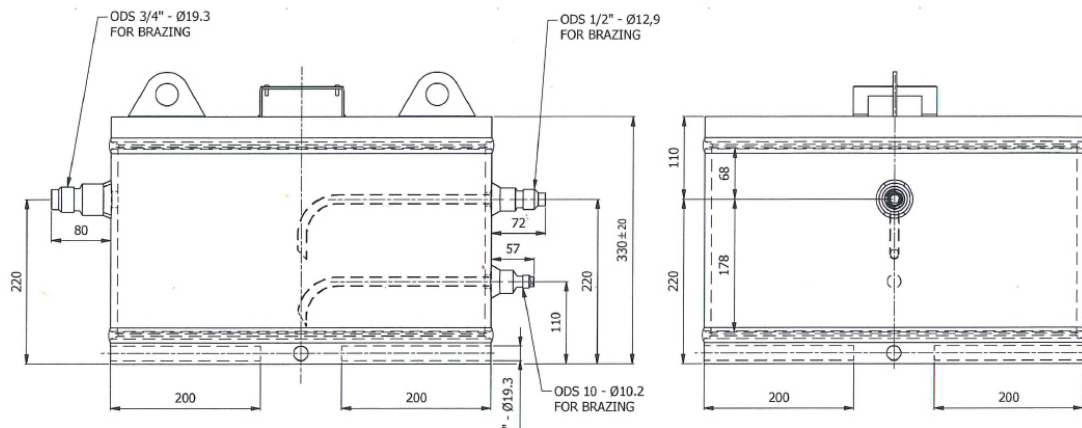


Figure 57. Sketches of the evaporators.

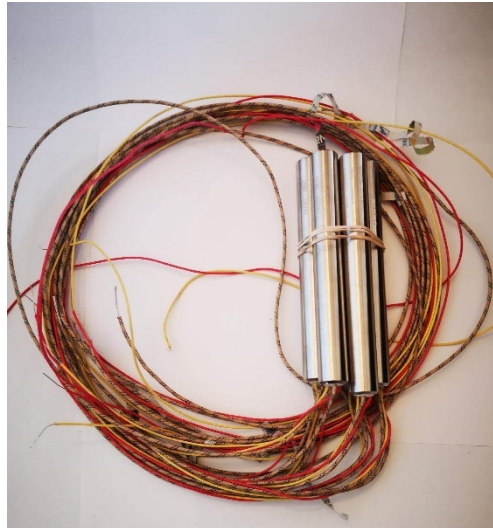


Figure 58. Photograph of the cartridge heaters.

5.2.6 Liquid pump

The operating conditions map for the liquid pump is reported in Figure 59, for all the investigated working fluids. Due to the above-mentioned limits on the electrical power, the volumetric flow rate of the liquid pump must be limited to 4 l min^{-1} . Considering the high discharge and differential pressure, a multi-diaphragm pump was selected (G13XKSJHFEHA, provided by Hydra-Cell). The pump will be coupled with an inverter in order to regulate the flow rate in a range 10-100% with respect to the nominal value (270 l h^{-1} at 50 Hz). The delivery of the component required a long time due to the handmade production. At the time of the writing of the thesis, the component was not delivered yet.

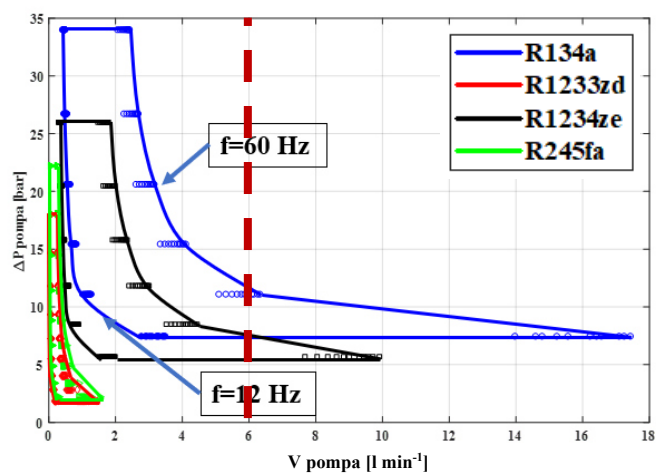


Figure 59. Differential pressure as a function of the pump volumetric flow rate, at the minimum and maximum compressor frequency.

5.2.7 Expansion valve

Figure 60 shows the simulation results exploring the possible operating conditions of the expansion valve. In order to choose the appropriate expansion device, two limit operating conditions are considered: point A, that represents the condition with the minimum differential pressure and the maximum volumetric flow rate and point B, with the maximum pressure drop and the minimum volumetric flow rate. The specific operating conditions related to the points A and B are listed in Table 19.

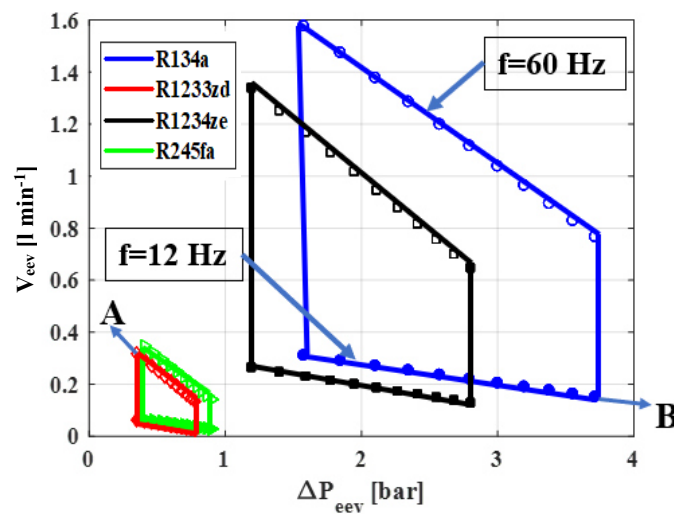


Figure 60. Expansion valve operating map in terms of volumetric flow rate and pressure drop.

Table 19. Expansion valve limit operating conditions.

Fluid	ρ_{valve} [kg m ⁻³]	V_{valve} [l min ⁻¹]	\dot{V}_{valve} [m ³ h ⁻¹]	ΔP_{valve} [bar]	K_v [m ³ h ⁻¹]
A R1233zd(E)	1286.7	0.32	0.019	0.35	0.037
B R134a	1243.8	0.15	0.009	3.71	0.005

The coefficient K_v can be evaluated by the following equation.

$$K_v = \dot{V}_{\text{valve}} \sqrt{\frac{\Delta P_{\text{rif}} \rho_{\text{valve}}}{\Delta P_{\text{valve}} \rho_{\text{rif}}}} \quad (5.3)$$

Where \dot{V}_{valve} e ρ_{valve} are the volumetric flow rate (m³ h⁻¹) and the density (kg m⁻³) at the inlet of the valve, ΔP_{valve} represents the pressure drop (Pa) across the valve. ΔP_{rif} and

ρ_{rif} represent the reference values for the pressure drop and the density, considering water as working fluid ($\Delta P_{rif} = 10^5$ Pa).

In order to guarantee the correct operation of the system in a wide range of operating conditions, two expansion valves (SER-AA and SER-B, provided by Parker) were chosen to work in parallel. A photograph of the component is shown in Figure 61.



Figure 61. Expansion valve.

5.3 Measurement instrumentation and data acquisition system

Several T-type thermocouples (Figure 62a), able to operate in a wide range of temperatures between -200 to 350 °C, will be placed throughout the experimental plant at the inlet and outlet of each component in order to monitor the refrigerant and water conditions during the experiments.

Four absolute pressure transducers (PXM319-070GI and PXM319-020GI, provided by Omega and showed in Figure 62b) measure the refrigerant absolute pressure at different points: on the vapor line at the exit of the high pressure evaporator, on the discharge line of the ejector, on the vapor line at the exit of the low pressure evaporator and on the discharge line of the compressor. Their range of effectiveness are 0-70 bar and 0-20 bar, with a current output signal of 4-20 mA. The accuracy of $\pm 0.25\%$, according to the manufacturer, includes the non-linearity, repeatability and hysteresis effects.

The volumetric flow rate in the experimental apparatus was measured thanks to a turbine volumetric flow rate (FMP 9.0.98.50, provided by Imsystem and showed in Figure 63a) placed after the sub-cooler, having an operative range of $0.025\text{-}3.0\text{ l min}^{-1}$ and giving a maximum uncertainty of $\pm 2\%$ of the reading. The device gives a frequency output signal that is converted into analogic signal $4\text{-}20\text{ mA}$ by a frequency counter (Figure 63b), with an accuracy of 0.01% as indicated by the manufactures.

As explained in the previous sections, the heat power at the evaporators was provided thanks to Joule effect by using AC power supply and a solid-state relay able to modulate the voltage applied to the ceramic cartridge heaters in a range $0\text{-}230\text{ V}$. The imposed heat rate will be measured by means of a digital wattmeter (Sirax BT5400, provided by Camille Bauer and showed in Figure 64a), with an analogic output signal $4\text{-}20\text{ mA}$. The device measures voltage and current separately, within a range of $100\text{-}500\text{ V}$ and $1\text{-}5\text{ A}$, respectively. A wound primary current transformer (Sirax CT110, provided by Camille Bauer, Figure 64b) is used to reduce the current of the electric heaters in a range $1\text{-}5\text{ A}$, falling into the wattmeter measuring range. The current transformer has an accuracy class of 0.5 , as indicated by the manufacture.

The different output signals coming from the transducers were read by a data acquisition system CompactRio, provided by National Instruments, and all the data were finally transferred to a pc desktop and monitored in Labview [109] environment. The data acquisition system is able to remote control for the variation of the pump and compressor frequency and for the variation of the operating mode of the system.

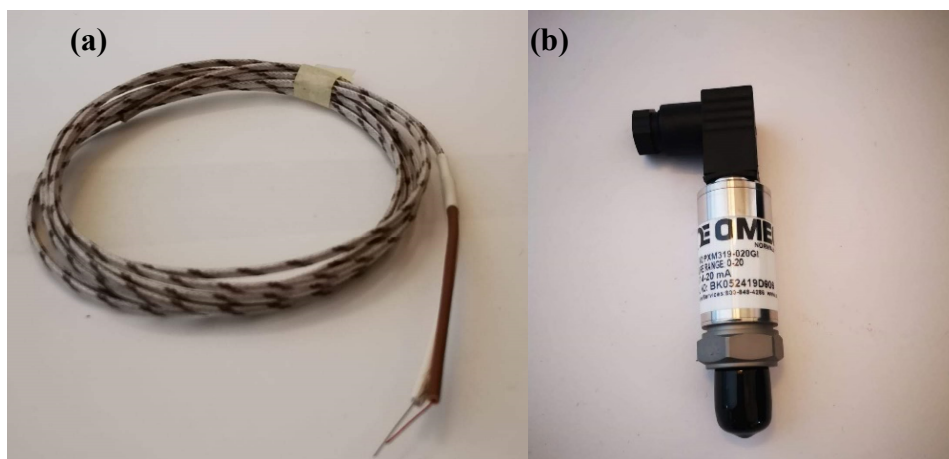


Figure 62. (a) T-type thermocouple. (b) Absolute pressure transducer.

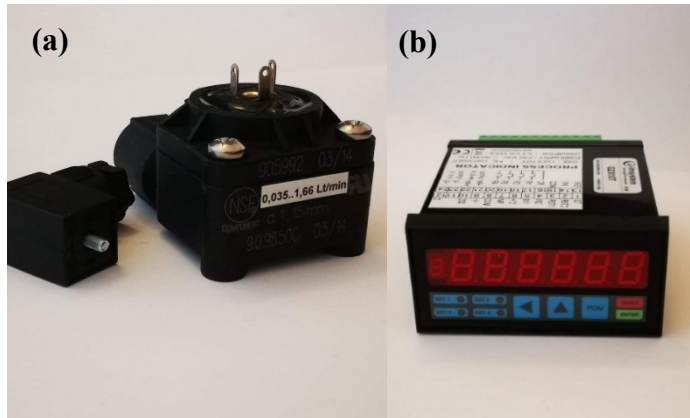


Figure 63. (a) Turbine volumetric flow rate. (b) Frequency counter.

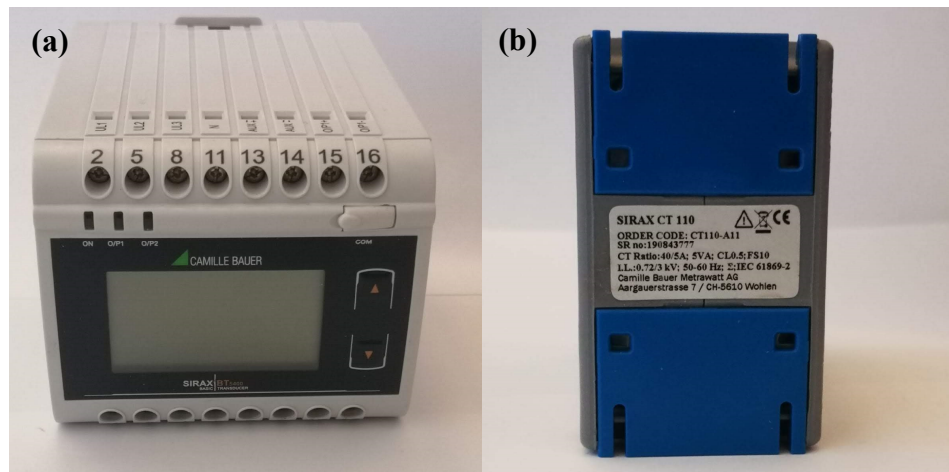


Figure 64. (a) Digital wattmeter. (b) Wound primary current transformer.

5.4 3D lay-out

In this paragraph, a description of the prototype 3-D lay-out (Figure 65 and Figure 66) is presented. At the first level, starting from the floor, the following components are located: compressor, oil separator, liquid pump and the arrangement for the flow rate measurement. At the upper level the three tanks, the ejector and the expansion valves can be found. Considering the axonometric view in Figure 65, the tanks represented in green and yellow are the high-pressure and low-pressure evaporators. The red tank in Figure 65 is the condenser meanwhile the sub-cooler is represented in light blue. Finally, the ejector is portrayed in dark blue. The location of the other main components can be seen in the axonometric view in Figure 66. The expansion valves are represented in light blue. The liquid pump is portrayed in green meanwhile, the compressor and the oil separator are represented in red and blue, respectively. Considering the other components, the solenoid

valves are provided by Danfoss (type EVR10, normally closed and showed in Figure 67a). The modulating three-way valve is provided by Parker and showed in Figure 67b).

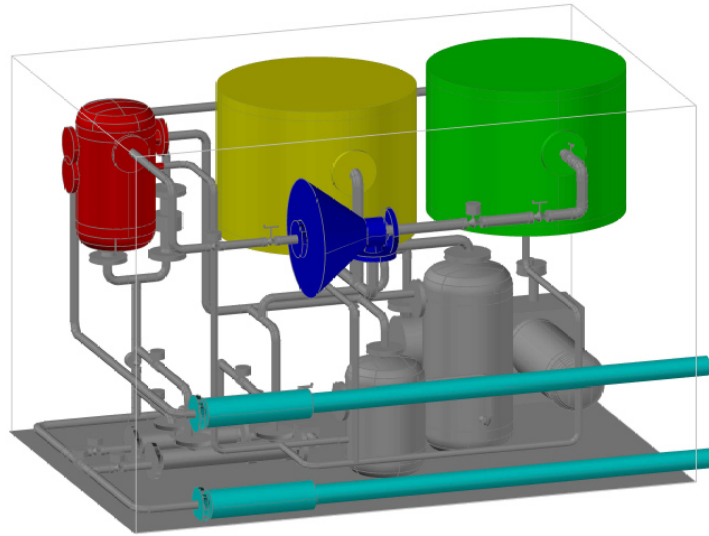


Figure 65. Prototype 3D lay-out, view 1.

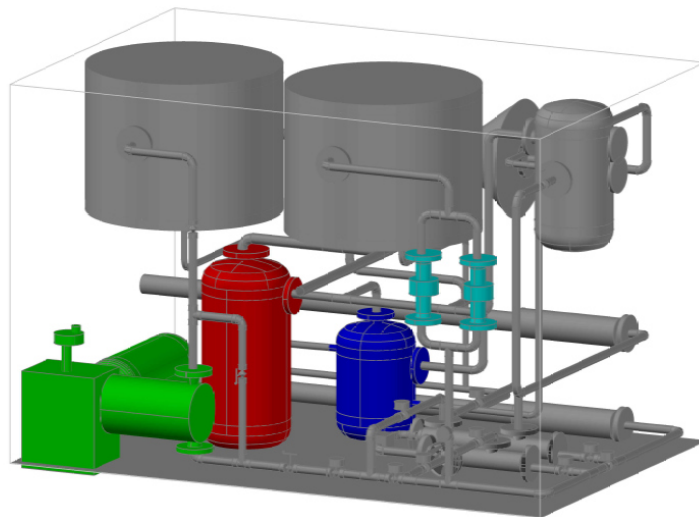


Figure 66. Prototype 3D lay-out, view 2.

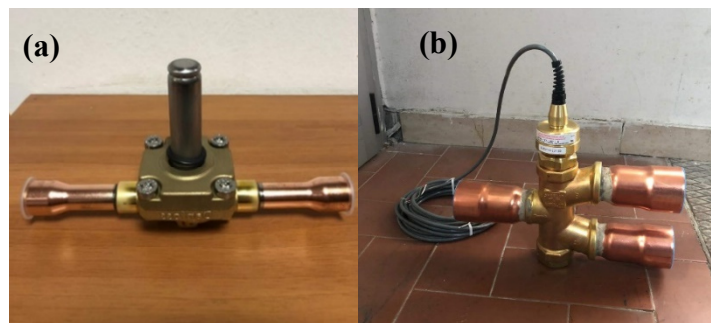


Figure 67. (a) Solenoid valve. (b) Modulating three-way valve.

6 Conclusions

The use of the ejector in vapor compression cycles and heat activated cooling cycle were studied in this thesis, both theoretically and experimentally. The main outcomes of this study are summarized here.

6.1 Summary of the research on two-phase ejector in transcritical vapor compression cycles

A comprehensive literature review on the use of two-phase ejector used in vapor compression cycle as expansion device has been performed, showing that:

- The use of ejector system as expansion device in vapor compression cycles could lead to relevant increment of the system performance (up to 60% with respect to conventional vapor compression cycles) depending on operating conditions.
- Various methods and models to estimate the two-phase ejector performance are currently available. The easier approach consists in 0-D model which considers constant ejector sections efficiencies. Meanwhile, models CFD based are able to take into account the influence of operating conditions and ejector geometry on ejector sections efficiencies as well as local flow characteristics. The main drawback is related to the uncertainty in the evaluation of the speed sound in a two-phase flow.

The experimental activity on a real heat pump working with the CO₂ as refrigerant provided by a multi-ejector system as expanding device instead of a traditional expansion valve provided the following outcomes:

- At fixed operating conditions, the multi-ejector pack configuration can be optimized in order to maximize the system performance. When producing hot water at a temperature of 60 °C, starting from 40 °C, for an ambient temperature of 12 °C, at compressor frequency of 50 Hz, the heating COP reaches a maximum value of 2.93 with a percentage increment equal to 98% with respect to the overall multi-ejector throat section giving the worst performance.
- The experimental results showed that the ejector efficiency reaches a maximum value equal to 17.7% at an overall cross section of 73.4%. However, the optimal

ejector configuration that maximizes the heating COP system does not correspond to the ejector configuration that maximizes the ejector efficiency.

Several prediction methods for the estimation of the mass flow rate flowing into the motive nozzle are available in scientific literature and some of them are compared to the collected data. However, these methods are developed for specific ejector geometry and operating conditions: for this reason, the considered correlations fit the experimental data with not satisfying agreement. Furthermore, a semi empirical correlation for the primary mass flow rate evaluation was proposed. Although the correlation coefficient was calibrated as function of the ejector geometry, the errors in the evaluation of the mass flow rate are similar to the existing methods. The MSE of the proposed correlation is equal to $4.02 \cdot 10^{-5}$ with errors in the prediction of the primary mass flow rate between -5 % and 11%.

6.2 Summary of the research waste heat driven hybrid ejector cycles

A thermo-economic analysis of a waste heat recovery hybrid ejector cycle (WHRHEC) for air conditioning purposes was performed in order to place the WHRHEC systems among the actual heat driven cooling technologies available on the market. An experimental in-depth analysis on flow boiling heat transfer of propane (R290) and R1233zd(E) at 25-65°C, being typical fluids and operating conditions occurring in ejector waste heat driven cooling systems, is showed. The main outcomes are summarized here.

6.2.1 Summary of the WHRHEC thermo-economic analysis

The performance of WHRHEC systems are strictly dependent on the working fluids. Among the investigated solutions, ammonia (R717) results to give the best performance and to be also economically advantageous, meanwhile the refrigerant R1233zd(E) presents higher specific set-up cost. From the total set of simulation, three singular solution (namely A, B and C) are considered as possible optimum configurations. Specifically, solution A provides the plant configuration with the lowest specific investment cost of 0.40 k€ per kW of cooling load and a COP of 0.21, using ammonia as working fluid. Instead, solution C maximizes the system performance, with a COP of 0.40, using R1233zd(E) as refrigerant but the specific set-up cost is very high (3.13 k€ kW⁻¹). Solution B could be the possible trade-off solution between low investment costs and high system performance and it is characterized by a set-up cost of 0.80 k€ kW⁻¹ and a COP equal to 0.39.

Comparing the WHRHEC systems to existing waste heat driven technologies for cooling purposes in terms of cost/performance result that heat driven ejector cooling systems could provide similar performances and lower investment costs with respect to ORC/VCC combined plants. When considering single-effect absorption systems, characterized by COP ranging between 0.6÷0.8, WHRHEC systems give lower COP values at the same costs (lower than 1.0 k€ kW⁻¹).

The economic analysis has shown that a WHRHEC may be a convenient solution to be integrated with a conventional VCC system in a plant according to the specific cost of electric energy and the waste heat time availability. Considering the solution B as design conditions for the WHRHEC system and with reference to the Italian situation, the economical convenience of the WHRHEC system is reached when the waste heat exploitation overcomes approximately 7800 hours (28% of the entire life-time).

A prototype of a heat driven ejector cooling cycle was designed. However, due to a long time for the delivery of the liquid pump required by the ad-hoc production, no experiments were performed.

6.2.2 Summary of the experimental results on flow boiling heat transfer at high temperature

Different flow boiling tests were performed with refrigerants R1233zd(E) and propane (R290). The experimental results showed that the heat flux has a significant effect on the experimental heat transfer coefficients, at any operating condition investigated and when propane (R290) is considered as working fluids. Trend with local vapor quality is also influenced by increasing the imposed heat flux: the effect of the vapor quality on the heat transfer coefficient becomes less and less significant. Analysing the effect of the saturation temperature, at low mass flux ($G = 150 \text{ kg m}^{-2}\text{s}^{-1}$) and high heat flux ($q = 40 \text{ kW m}^{-2}$), the heat transfer coefficients present a constant trend with vapor quality from the onset of boiling up to the dry-out incipience. However, the curve at 35 °C is higher (approximately +25%), suggesting a stronger influence of the saturation temperature when the operating conditions promote the nucleate boiling mechanism.

The experimental results related to the refrigerant R1233zd(E) show that a strong nucleate boiling contribution seems to exist at a large saturation temperature (65°C), a mass flux of 300 kg m⁻²s⁻¹ and for a heat flux larger than 20 kW m⁻². When considering

experiments with mass flux $300 \text{ kg m}^{-2}\text{s}^{-1}$ and imposed heat flux of 10 kW m^{-2} . A remarkable effect of the saturation temperature at high vapor qualities is observed. Up to a vapor quality of 0.20, with increasing saturation temperature the mean heat transfer coefficient presents a slight enhancement, which is observed at $65 \text{ }^\circ\text{C}$. For higher vapor qualities, instead, the heat transfer coefficient is penalized with increasing reduced pressure.

Appendix

A. Thermodynamic analysis results

Table 20. Thermodynamic analysis results for R1234ze.

R1234ze														
ΔT_g	ΔT_{co}	ΔT_{ev}	T_g	P_g	T_{co}	P_{co}	T_{ev}	P_{ev}	μ	Π	β	COP	Q_g	Q_{co}
[°C]	[°C]	[°C]	[°C]	[bar]	[°C]	[bar]	[°C]	[bar]	[-]	[-]	[-]	[-]	[kW]	[kW]
1	1	1	91.1	25.3	25.8	5.1	6	2.7	0.370	1.90	4.95	0.33	60.0	80.9
3	3	3	85.0	22.33	27.9	5.43	4	2.50	0.261	2.17	4.11	0.23	86.6	107.6
5	5	5	79.7	19.95	29.9	5.76	2	2.33	0.173	2.47	3.46	0.15	133.0	154.4
10	5	5	69.0	15.75	29.9	5.76	2	2.33	0.096	2.47	2.73	0.08	237.0	258.7
5	10	5	77.3	18.95	34.9	6.65	2	2.33	0.084	2.85	2.85	0.07	279.7	302.3
5	5	10	79.7	19.94	29.9	5.76	-3	1.94	0.140	2.98	3.46	0.12	168.0	189.7
10	10	10	66.5	14.86	34.8	6.65	-3	1.94	0.008	3.43	2.24	0.01	3168.4	3208.4

Table 21. Thermodynamic analysis results for Ammonia (R717).

Ammonia (R717)														
ΔT_g	ΔT_{co}	ΔT_{ev}	T_g	P_g	T_{co}	P_{co}	T_{ev}	P_{ev}	μ	Π	β	COP	Q_g	Q_{co}
[°C]	[°C]	[°C]	[°C]	[bar]	[°C]	[bar]	[°C]	[bar]	[-]	[-]	[-]	[-]	[kW]	[kW]
1	1	1	87.2	48.3	25.9	10.3	6	5.3	0.397	1.93	4.68	0.39	51.1	71.5
3	3	3	83.9	45.06	28.0	10.98	4	4.97	0.286	2.21	4.10	0.28	71.3	91.8
5	5	5	80.7	42.04	30.0	11.66	2	4.62	0.197	2.52	3.61	0.19	104.1	124.8
10	5	5	73.8	36.13	29.9	11.65	2	4.62	0.132	2.52	3.10	0.13	156.0	176.8
5	10	5	79.9	41.30	34.9	13.49	2	4.62	0.108	2.92	3.06	0.11	189.7	210.8
5	5	10	80.7	42.05	30.0	11.66	-3	3.83	0.159	3.04	3.61	0.15	129.8	150.6
10	10	10	72.9	35.36	34.9	13.48	-3	3.83	0.039	3.52	2.62	0.04	534.4	556.9

Table 22. Thermodynamic analysis results for R1233zd(E).

R1233zd(E)														
ΔT_g	ΔT_{co}	ΔT_{ev}	T_g	P_g	T_{co}	P_{co}	T_{ev}	P_{ev}	μ	Π	β	COP	Q_g	Q_{co}
[°C]	[°C]	[°C]	[°C]	[bar]	[°C]	[bar]	[°C]	[bar]	[-]	[-]	[-]	[-]	[kW]	[kW]
1	1	1	82.2	6.9	25.9	1.3	6	0.6	0.438	2.16	5.19	0.39	50.8	70.9
3	3	3	78.9	6.41	27.9	1.44	4	0.57	0.313	2.53	4.45	0.28	72.0	92.3
5	5	5	75.4	5.87	29.9	1.54	2	0.52	0.210	2.95	3.81	0.18	108.4	128.7
10	5	5	67.8	4.83	29.9	1.54	2	0.52	0.151	2.95	3.13	0.13	150.7	171.0
5	10	5	74.1	5.67	34.9	1.83	2	0.52	0.098	3.50	3.11	0.08	237.2	257.7
5	5	10	75.1	5.83	29.9	1.54	-3	0.42	0.130	3.69	3.78	0.11	178.4	198.8
10	10	10	66.2	4.62	34.9	1.83	-3	0.42	0.012	4.37	2.53	0.01	1957.0	1980.4

Table 23. Thermodynamic analysis results for Isobutane (R600a).

Isobutane (R600a)														
ΔT_g	ΔT_{co}	ΔT_{ev}	T_g	P_g	T_{co}	P_{co}	T_{ev}	P_{ev}	μ	Π	β	COP	Q_g	Q_{co}
[°C]	[°C]	[°C]	[°C]	[bar]	[°C]	[bar]	[°C]	[bar]	[-]	[-]	[-]	[-]	[kW]	[kW]
1	1	1	81.9	14.0	25.9	3.6	6	1.9	0.322	1.86	3.88	0.29	68.8	89.4
3	3	3	77.8	12.83	27.9	3.82	4	1.80	0.218	2.12	3.36	0.19	103.3	124.0
5	5	5	73.4	11.70	29.9	4.04	2	1.68	0.132	2.40	2.90	0.12	173.1	194.1
10	5	5	64.2	9.57	29.9	4.04	2	1.68	0.053	2.40	2.37	0.05	425.3	447.2
5	10	5	71.6	11.25	34.9	4.64	2	1.68	0.046	2.76	2.42	0.04	503.0	525.7
5	5	10	73.4	11.69	29.9	4.04	-3	1.41	0.107	2.87	2.89	0.09	218.4	239.7
10	10	10	65.6	9.88	34.9	4.64	-3	1.41	0.261	3.29	2.13	0.21	94.4	114.8

Table 24. Thermodynamic analysis results for R134a.

R134a														
ΔT_g	ΔT_{co}	ΔT_{ev}	T_g	P_g	T_{co}	P_{co}	T_{ev}	P_{ev}	μ	Π	β	COP	Q_g	Q_{co}
[°C]	[°C]	[°C]	[°C]	[bar]	[°C]	[bar]	[°C]	[bar]	[-]	[-]	[-]	[-]	[kW]	[kW]
1	1	1	82.1	26.3	25.8	6.8	6	3.6		1.88	3.86			
3	3	3	92.0	33.78	27.9	7.24	4	3.38	0.242	2.14	4.66	0.22	90.5	112.1
5	5	5	83.8	28.54	29.9	7.67	2	3.15	0.161	2.44	3.72	0.14	138.0	159.9
10	5	5	71.9	22.08	29.8	7.67	2	3.15	0.095	2.44	2.88	0.09	233.7	255.9
5	10	5	81.1	26.94	34.8	8.83	2	3.15	0.081	2.81	3.05	0.07	280.9	304.5
5	5	10	83.8	28.53	29.9	7.67	-3	2.62	0.132	2.92	3.72	0.12	171.6	194.0
10	10	10	69.3	20.82	34.8	8.83	-3	2.62	0.009	3.37	2.36	0.01	2471.2	2511.9

Table 25. Thermodynamic analysis results for Butane (R600).

Butane (R600)														
ΔT_g	ΔT_{co}	ΔT_{ev}	T_g	P_g	T_{co}	P_{co}	T_{ev}	P_{ev}	μ	Π	β	COP	Q_g	Q_{co}
[°C]	[°C]	[°C]	[°C]	[bar]	[°C]	[bar]	[°C]	[bar]	[-]	[-]	[-]	[-]	[kW]	[kW]
1	1	1	80.7	10.3	26.0	2.5	6	1.3	0.356	1.95	4.10	0.32	62.1	82.5
3	3	3	77.1	9.49	27.9	2.66	4	1.20	0.248	2.22	3.56	0.22	90.6	111.0
5	5	5	73.2	8.71	29.9	2.83	2	1.11	0.158	2.54	3.08	0.14	144.0	164.5
10	5	5	64.9	7.18	30.0	2.83	2	1.11	0.086	2.54	2.54	0.08	262.4	283.2
5	10	5	71.8	8.43	34.9	3.28	2	1.11	0.071	2.95	2.57	0.06	325.7	346.8
5	5	10	73.2	8.69	29.9	2.83	-3	0.92	0.125	3.08	3.07	0.11	186.2	206.9
10	10	10	47.4	4.63	35.9	3.37	-3	0.92	-0.121	3.66	1.37			

Table 26. Thermodynamic analysis results for Propane (R290).

Propane (R290)														
ΔT_g	ΔT_{co}	ΔT_{ev}	T_g	P_g	T_{co}	P_{co}	T_{ev}	P_{ev}	μ	Π	β	COP	Q_g	Q_{co}
[°C]	[°C]	[°C]	[°C]	[bar]	[°C]	[bar]	[°C]	[bar]	[-]	[-]	[-]	[-]	[kW]	[kW]
1	1	1	83.2	31.3	27.2	10.1	6	5.7		1.77	3.11		213.9	237.3
3	3	3	82.5	31.3	28.8	10.5	4	5.4		1.96	2.99		301.7	326.5
5	5	5	87.7	36.1	31.0	11.1	2	5.0	0.073	2.19	3.27	0.06	337.6	364.3
10	5	5	80.0	31.3	30.9	11.0	2	5.0	0.048	2.19	2.84	0.04	520.5	548.7
5	10	5	86.0	35.0	35.0	12.2	2	5.0	0.019	2.42	2.87	0.02	1303.8	1348.2
5	5	10	87.7	36.1	31.0	11.1	-3	4.3	0.062	2.56	3.27	0.05	404.9	432.9
10	10	10	80.0	31.3	35.0	12.2	-3	4.3	0.002	2.82	2.57	0.00	13192.1	13415.8

B. Heat exchangers geometrical data

Table 27. Main sizing parameters of the heat exchangers.

High-pressure evaporator		Condenser		Low-pressure evaporator	
Plate heat exchanger		Plate fin and tube		One pass shell and tube	
Plate height [mm]	to be calculated	tube length [mm]	to be calculated	tube length [mm]	to be calculated
Plate width [mm]	500	fin step [mm]	2.5	tube number	to be calculated
Plate spacing [mm]	1.0	fin thickness [mm]	0.3	Internal tube diameter [mm]	12
Wavelength corrugation [mm]	1.0	Tube step [mm]	33	Tube thickness [mm]	0.5
Chevron angle [°]	80	Rank step [mm]	33	Pitch size [mm]	18
Channel number [#]	10	Tube number [#]	10	Baffle spacing [mm]	160
Plate thickness [mm]	0.2	Tube external diameter [mm]	10	Shell diameter [mm]	180
		tube thickness [mm]	1.0		
		Rank number [#]	5		

Nomenclature

Roman

A	area	[m ²]
A _r	ejector area ratio	[-]
COP	coefficient of performance	[-]
c _p	specific heat at constant pressure	[kJ kg ⁻¹ K ⁻¹]
d	inner diameter	[m]
D	outer diameter	[m]
D _h	hydraulic diameter	[m]
E _{el}	electrical energy consumption	[kWh]
f	frequency	[Hz]
G	mass flux	[kg m ⁻² s ⁻¹]
h	specific enthalpy	[kJ kg ⁻¹]
ic	specific investment costs	[k€ kW ⁻¹]
IC	investment cost	[k€]
k	specific heat ratio	[-]
k _{ee}	electric energy specific cost	[€ kWh ⁻¹]
k _{VCC}	VCC specific set-up cost	[k€ kW ⁻¹]
k _{WHR}	WHR specific set-up cost	[k€ kW ⁻¹]
\dot{m}	mass flow rate	[kg s ⁻¹]
p	pressure	[bar]
q	heat flux	[kW m ⁻²]
\dot{Q}	heat power	[kW]
R	specific gas constant	[kJ kg ⁻¹ K ⁻¹]
s	specific entropy	[kJ kg ⁻¹ K ⁻¹]

SCOP	seasonal coefficient of performance	[-]
T	temperature	[K]
tc	specific total costs	[k€ kW ⁻¹]
TC	total costs	[k€]
u	velocity	[m s ⁻¹]
u _c (x)	combined uncertainty of x	[the same of x]
U	overall heat transfer coefficient	[W m ⁻² K ⁻¹]
V	volume	[m ³]
\dot{V}	volumetric flow rate	[m ³ s ⁻¹]
\dot{W}	power	[kW]
x	local vapor quality	[-]
X _{WHR}	fraction of the cooling load covered by the WHR	[-]
Y	fraction of the total life-time period when the waste heat source is available	[-]

Greek

α	convective heat transfer coefficient	[W m ⁻² K ⁻¹]
β	ejector pressure ratio	[-]
δ	thickness	[m]
Δ	variation	[-]
ε	heat exchanger efficiency	[-]
η	efficiency	[-]
θ_{life}	time life	[h]
κ	thermal conductivity	[W m ⁻¹ K ⁻¹]
μ	entrainment ratio	[-]
Π	pressure lift	[-]

ρ density [kg m⁻³]

Subscripts

amb ambient
co condenser
cold cold fluid side
cp compressor
cr thermodynamic critical point
D diffuser
eff effective
ej ejector
ev evaporator
f secondary fluid side
fluid fluid side
g vapor generator
gc gas cooler
hot hot fluid side
in inlet side
M mixing
mat material
mix mixing section
N motive nozzle
out outlet side
p pump
pf primary flow
preh preheater
ref refrigerant side

rhe	regenerative heat exchanger
s	isentropic state
sat	saturation condition
sf	secondary flow
th	throat section
tot	total
tube	tube
user	end-user side
w	water
wall	wall side

Abbreviations

CP	compressor
EEV	electronic expansion valve
EJEC	ejector
EVAP	evaporator
GWP	global warming potential
IHE	internal heat exchanger
ODP	ozone depletion potential
ORC	organic Rankine Cycle
VCC	vapor compression cycle
WHR	waste heat recovery
WHRHEC	waste heat recovery hybrid ejector cycle

Dimensionless numbers

M	Mach number
---	-------------

M^*	critical Mach number
Nu	Nusselt number
Pr	Prandtl number
Re	Reynolds number

List of Figures

Figure 1. Schematic layout of vapor compression cycle using ejector as expansion device.	6
Figure 2. (a) Climatic chamber at ENEA research center. (b) Prototype of a carbon dioxide heat pump with multi-ejector system as expansion device.	13
Figure 3. Schematic layout of multi ejector expansion CO ₂ vapor compression system.	14
Figure 4. Thermodynamic cycles on (a) T-s and (b) p-h diagram of the multi ejector heat pump at the following operating conditions: T _{amb} of 7°C, T _{w,in} of 40°C, T _{w,out} of 60°C and heating capacity of 11.7 kW.....	15
Figure 5. Gas cooler inlet and outlet water temperatures (a) and climatic chamber temperature (b) variations during the test.	16
Figure 6. Gas cooler and evaporator pressures variations during the test.....	16
Figure 7.(a) p-h diagram and (b) T-s diagram, variation of the thermodynamic cycle varying the overall ejectors cross section.	22
Figure 8. Performance variations as a function of the overall ejectors cross section. (a) Heating capacity (left) and compressor work (right); (b) COP (left) and ejector efficiency (right).	22
Figure 9. (a) p-h diagram and (b) T-s diagram, variation of the thermodynamic cycle varying the climatic chamber temperature.....	23
Figure 10. Pressure levels at (a) T _{w,in} = 30°C and (b) T _{w,in} = 40°C as a function of the climatic chamber temperature.....	23
Figure 11. COP as a function of the climatic chamber temperature.	24
Figure 12.(a) p-h diagram and (b) T-s diagram, variation of the thermodynamic cycle varying the compressor frequency.	25
Figure 13. COP (left) and ejector efficiency (right) as a function of the compressor frequency.....	26

Figure 14. Performance variations as a function of the overall ejectors cross section. (a) Primary mass flow rate; (b) entrainment ratio (left) and pressure lift ratio (right).	35
Figure 15. Performance variations as a function of the overall ejectors cross section. COP (left) and ejector efficiency (right).	35
Figure 16. Test input conditions for the three ejectors in the T-s diagram.	39
Figure 17. Percentage error in mass flow rate calculation using Lucas correlation (3.2), (3.3), (3.4): (a) original version; (b) coefficient recalculated by solver.	40
Figure 18. Percentage error in mass flow rate calculation with coefficient recalculated by solver: (a) Banasiak correlation (3.5); (b) Martin correlation (3.6).	41
Figure 19. Percentage error in mass flow rate calculation: (a) new correlation (3.6) with coefficient calculated by solvers; (b) specific mass flow rate as function of the parameter η_{ise}	42
Figure 20. Percentage error in mass flow rate calculation: (a) new method with coefficient calculated by solvers; (b) specific mass flow rate as function of entropy at ejector inlet.	42
Figure 21. (a) Schematic lay-out (b) Example of an ejector cooling cycle on T-s diagram for the fluid R1234ze.	54
Figure 22. Operation modes of an ejector.	55
Figure 23. Schematic ejector representation.	56
Figure 24. Ejector working processes on T-s diagram.	57
Figure 25. Saturation curves in pressure-temperature diagram for the selected working fluids.	66
Figure 26. Entrainment ratio as function of pressure ratio and pressure lift for different pinch point values at the heat exchangers.	69
Figure 27. System COP as function of pressure ratio and pressure lift for different pinch point values at the heat exchangers.	70

Figure 28. COP versus specific investment costs for all the chosen combinations. The highlighted markers refer to the solutions investigated for the thermodynamic analysis and each color is related to a specific working fluid. 71

Figure 29. Share of the total investment costs for the hybrid ejector plant..... 72

Figure 30. System performance and specific investment costs range of ORC+VCC and single effect absorption plant. Highlighted solutions: A (minimum cost), C (maximum performance) and B (best compromise between cost and COP). Asterisk solutions A* and B* refer to plate heat exchanger type at the low-pressure evaporator instead of a shell and tube heat exchanger..... 74

Figure 31. Schematic diagram of a combined WHRHEC/VCC system to supply the end user cooling load. 75

Figure 32. Specific cost savings as a function of the operating time of the combined plant (4000 working hours per year are considered). SCOP and kee are respectively fixed to 2.5 and 0.14 c€ kWh-1 (Italian market [101]). a) Effect of the WHR plant size for $Y = 0.80$; b) Effect of the waste heat availability for $XWHR = 0.5$ 76

Figure 33. Required life-time ($\Delta tc = 0$) as a function of the waste heat availability Y , for different countries according to their specific cost of the electric energy. The horizontal line refers to a realistic operating time of 7 years..... 77

Figure 34. $XWHR$ - Y map developed for the Italian cost of the electric energy, by considering a total operating time of 7 years and a SCOP of the VCC plant equal to 2.5. The curves refer to either specific cost savings (in blue) or losses (in red)..... 78

Figure 35. Representation of the test facility. 79

Figure 36. Test section illustration and its main characteristics. 80

Figure 37. Effect of mass flux on mean heat transfer coefficients. Experiments performed at saturation temperature of 35°C and with an imposed heat flux of 20 kW m⁻². 85

Figure 38. Effect of heat flux on mean heat transfer coefficients. Experiments performed at saturation temperature of 65°C and with a mass flux of 300 kg m⁻²s⁻¹. 86

Figure 39. Effect of saturation temperature on mean heat transfer coefficients. Experiments performed at a mass flux of $300 \text{ kg m}^{-2}\text{s}^{-1}$ and with an imposed heat flux of 10 kW m^{-2}	86
Figure 40. Effect of the mass velocity on the local heat transfer coefficient. (a) $T_{\text{sat}} = 25 \text{ }^\circ\text{C}$ and $q = 10 \text{ kW m}^{-2}$. (b) $T_{\text{sat}} = 35 \text{ }^\circ\text{C}$ and $q = 40 \text{ kW m}^{-2}$	87
Figure 41. Effect of the saturation temperature on the local heat transfer coefficient. (a) $G = 300 \text{ kg m}^{-2}\text{s}^{-1}$ and $q = 10 \text{ kW m}^{-2}$. (b) $G = 150 \text{ kg m}^{-2}\text{s}^{-1}$ and $q = 40 \text{ kW m}^{-2}$	88
Figure 42. Effect of the heat flux on the local heat transfer coefficient. (a) $T_{\text{sat}} = 25 \text{ }^\circ\text{C}$ and $G = 300 \text{ kg m}^{-2}\text{s}^{-1}$. (b) $T_{\text{sat}} = 35 \text{ }^\circ\text{C}$ and $G = 150 \text{ kg m}^{-2}\text{s}^{-1}$	89
Figure 43. Experimental versus predicted heat transfer coefficient trends with vapor quality. (a) R1233zd(E) at $T_{\text{sat}} = 65 \text{ }^\circ\text{C}$, $G = 150 \text{ kg m}^{-2}\text{s}^{-1}$, $q = 10 \text{ kW m}^{-2}$. (b) Propane at $T_{\text{sat}} = 35 \text{ }^\circ\text{C}$, $G = 150 \text{ kg m}^{-2}\text{s}^{-1}$, $q = 10 \text{ kW m}^{-2}$	90
Figure 44. Schematic layout of the hybrid ejector cooling cycle experimental apparatus.	95
Figure 45. Operating modes of the hybrid ejector cooling cycle experimental apparatus.	96
Figure 46. (a) Global efficiency and (b) volumetric flow rate as function of compression ratio.	98
Figure 47. (a) Compressor operating map in terms of compression ratio and volumetric flow rate. (b) Electric power required by the compressor as a function of mass flow rate, at the minimum and maximum compressor frequency.	99
Figure 48. Copeland scroll compressor ZS13KAE. (b) Oil separator.	99
Figure 49. Traxoil – oil system management.	99
Figure 50. Thermal load at the low-pressure evaporator as function of the evaporation temperature.	100
Figure 51. Thermal load at the high-pressure evaporator as function of the vapor generator temperature, for each investigated working fluid.	101
Figure 52. Photograph of the tank working as evaporator.	101

Figure 53. Sketches of the condenser.....	102
Figure 54. Photograph of the tank working as condenser.....	103
Figure 55. Sketches of the sub-cooler.....	103
Figure 56. Shell and tube heat exchanger – sub-cooler.....	104
Figure 57. Sketches of the evaporators.....	104
Figure 58. Photograph of the cartridge heaters.....	105
Figure 59. Differential pressure as a function of the pump volumetric flow rate, at the minimum and maximum compressor frequency.....	105
Figure 60. Expansion valve operating map in terms of volumetric flow rate and pressure drop.....	106
Figure 61. Expansion valve.....	107
Figure 62. (a) T-type thermocouple. (b) Absolute pressure transducer.....	108
Figure 63. (a) Turbine volumetric flow rate. (b) Frequency counter.....	109
Figure 64. (a) Digital wattmeter. (b) Wound primary current transformer.....	109
Figure 65. Prototype 3D lay-out, view 1.....	110
Figure 66. Prototype 3D lay-out, view 2.....	110
Figure 67. (a) Solenoid valve. (b) Modulating three-way valve.....	110

List of Tables

Table 1. Motive nozzle geometric characteristics.	13
Table 2. Measurement instrumentation and uncertainty.	15
Table 3. Permissible deviations from set values [22].....	16
Table 4. Uncertainty analysis.	19
Table 5. Investigated test conditions.	20
Table 6. Investigated multi-ejector area ratios.	21
Table 7. Motive nozzle throat sections diameters and experimental test distribution.	39
Table 8. Single phase and two-phase heat transfer correlations.....	64
Table 9. Characteristics of the selected working fluids.	65
Table 10. Cost functions for each component.	67
Table 11. Specification of the simulated boundary conditions.	68
Table 12. Operating conditions used for the thermo-economic analysis.	71
Table 13. Summary of the three configurations chosen as possible optimum case. The asterisk solutions refer to the use of a plate heat exchanger instead of a shell and tube heat exchanger for the low-pressure evaporator.	72
Table 14. Summary of uncertainty analysis.	83
Table 15. Summary of the operating conditions used for the components sizing.	97
Table 16. Compressor operating conditions design.	97
Table 17. Condenser design conditions.....	102
Table 18. Shell and tube design conditions.....	103
Table 19. Expansion valve limit operating conditions.....	106
Table 20. Thermodynamic analysis results for R1234ze.	115
Table 21. Thermodynamic analysis results for Ammonia (R717).	115

Table 22. Thermodynamic analysis results for R1233zd(E).....	116
Table 23. Thermodynamic analysis results for Isobutane (R600a).....	116
Table 24. Thermodynamic analysis results for R134a.....	117
Table 25. Thermodynamic analysis results for Butane (R600).....	117
Table 26. Thermodynamic analysis results for Propane (R290).....	118
Table 27. Main sizing parameters of the heat exchangers.	119

Bibliography

- [1]. International Energy Agency. World Energy Outlook. 2014.
- [2]. International Energy Agency. Energy Technology Perspectives: Scenarios & Strategies to 2050. 2010.
- [3]. Report: Financing the Energy Efficient Transformation of the Building Sector in EU. <<http://www.isi.fraunhofer.de/>>; 2012 [accessed 12.06.16].
- [4]. Nejat, P., Jomehzadeh, F., Taheri, M. M., Gohari, M., Majid, M. Z. A. (2015). A global review of energy consumption, CO₂ emissions and policy in the residential sector (with an overview of the top ten CO₂ emitting countries). Renewable and sustainable energy reviews, 43, 843-862.
- [5]. European Parliament. Directive 2010/31/EU of the European Parliament and of Council of 19 May 2010 on the energy performance of buildings (recast). Official journal of the European Union; 2010. pp. 13–25.
- [6]. European Heat Pump Association, 2019. European Heat Pump Market and Statistics Report 2019. Executive Summary.
- [7]. Council EPA, 2009. Directive 2009/28/EC of the European Parliament and of the Council of 23 April 2009 on the promotion of the use of energy from renewable sources and amending and subsequently repealing Directives 2001/77/EC and 2003/30/EC. Official Journal of the European Union, 5, L 140/16-62.
- [8]. European Commission, 2013. Commission Regulation (EU) No 813/2013 of 2 August 2013 implementing Directive 2009/125/ EC of the European Parliament and of the Council with regard to Ecodesign requirements for space heaters and combination heaters.
- [9]. Council EPA, 2014. Regulation (EU) No 517/2014 of the European Parliament and the Council of 16 April 2014 on fluorinated greenhouse gases and repealing regulation (EC) No 842/2006. Off. J. Eur. Union, L 150/195-230.
- [10]. Goetzler, W., Sutherland, T., Rassi, M., Burgos, J., 2014. Research & development roadmap for next-generation low global warming potential refrigerants. Building Technologies Office, Office of Energy Efficiency and Renewable Energy, US Department of Energy, November.

- [11]. Elbel, S., Hrnjak, P. (2008). Experimental validation of a prototype ejector designed to reduce throttling losses encountered in transcritical R744 system operation. *International Journal of Refrigeration*, 31(3), 411-422.
- [12]. Sarkar, J. (2012). Ejector enhanced vapor compression refrigeration and heat pump systems—A review. *Renewable and Sustainable Energy Reviews*, 16(9), 6647-6659.
- [13]. Liu, F., Li, Y., Groll, E. A. (2012). Performance enhancement of CO₂ air conditioner with a controllable ejector. *International Journal of Refrigeration*, 35(6), 1604-1616.
- [14]. Liu, F., Groll, E. A., Li, D. (2012). Investigation on performance of variable geometry ejectors for CO₂ refrigeration cycles. *Energy*, 45(1), 829-839.
- [15]. Lee, J. S., Kim, M. S., Kim, M. S. (2011). Experimental study on the improvement of CO₂ air conditioning system performance using an ejector. *International Journal of Refrigeration*, 34(7), 1614-1625.
- [16]. Lee, J. S., Kim, M. S., Kim, M. S. (2014). Studies on the performance of a CO₂ air conditioning system using an ejector as an expansion device. *International Journal of Refrigeration*, 38, 140-152.
- [17]. Nakagawa, M., Marasigan, A. R., Matsukawa, T. (2011). Experimental analysis on the effect of internal heat exchanger in transcritical CO₂ refrigeration cycle with two-phase ejector. *International Journal of Refrigeration*, 34(7), 1577-1586.
- [18]. Nakagawa, M., Marasigan, A. R., Matsukawa, T., Kurashina, A. (2011). Experimental investigation on the effect of mixing length on the performance of two-phase ejector for CO₂ refrigeration cycle with and without heat exchanger. *International Journal of Refrigeration*, 34(7), 1604-1613.
- [19]. Banasiak, K., Hafner, A., Andresen, T. (2012). Experimental and numerical investigation of the influence of the two-phase ejector geometry on the performance of the R744 heat pump. *International journal of Refrigeration*, 35(6), 1617-1625.
- [20]. Lucas, C., Koehler, J. (2012). Experimental investigation of the COP improvement of a refrigeration cycle by use of an ejector. *International Journal of Refrigeration*, 35(6), 1595-1603.
- [21]. Minetto, S., Brignoli, R., Banasiak, K., Hafner, A., Zilio, C. (2013). Performance assessment of an off-the-shelf R744 heat pump equipped with an ejector. *Applied Thermal Engineering*, 59(1-2), 568-575.

- [22]. UNI EN 14511. Air conditioners, liquid chilling packages and heat pumps with electrically driven compressors for space heating and cooling. Part 3: Test methods.
- [23]. MATLAB and Statistics Toolbox Release 2015a, The MathWorks, Inc., Natick, Massachusetts, United States.
- [24]. Lemmon EW, Huber ML, McLinden MO. Reference Fluid Thermodynamic and Transport Properties, Nist Standard Reference Database 23, version 9.1, Physical and Chemical Properties Division, NIST, USA, 2002.
- [25]. Moffat, R. J. (1982). Contributions to the theory of single-sample uncertainty analysis. *Journal of Fluids Engineering*, 104(2), 250-258.
- [26]. Liu F, Groll EA, Ren J. Comprehensive experimental performance analyses of an ejector expansion transcritical CO₂ system. *Appl. Therm. Eng.* 2016; 98: 1061–69.
- [27]. Kornhauser, A. A. (1990). The use of an ejector as a refrigerant expander.
- [28]. Li, D., Groll, E. A. (2005). Transcritical CO₂ refrigeration cycle with ejector-expansion device. *International Journal of refrigeration*, 28(5), 766-773.
- [29]. Liu, F., Groll, E. A. (2013). Study of ejector efficiencies in refrigeration cycles. *Applied Thermal Engineering*, 52(2), 360-370.
- [30]. Butrymowicz, D. (2003). Improvement of compression refrigeration cycle by means of two-phase ejector. *Proc. 21st Int. Cong. Refrigeration*, Washington DC.
- [31]. Lucas, C., Koehler, J., Schroeder, A., Tischendorf, C. (2013). Experimentally validated CO₂ ejector operation characteristic used in a numerical investigation of ejector cycle. *International journal of refrigeration*, 36(3), 881-891.
- [32]. Angielczyk, W., Seynhaeve, J. M., Gagan, J., Bartosiewicz, Y., Butrymowicz, D. (2019). Prediction of critical mass rate of flashing carbon dioxide flow in convergent-divergent nozzle. *Chemical Engineering and Processing-Process Intensification*, 143, 107599.
- [33]. Banasiak, K., Hafner, A. (2011). 1D Computational model of a two-phase R744 ejector for expansion work recovery. *International Journal of Thermal Sciences*, 50(11), 2235-2247.
- [34]. Banasiak, K., Hafner, A. (2013). Mathematical modelling of supersonic two-phase R744 flows through converging–diverging nozzles: The effects of phase transition models. *Applied Thermal Engineering*, 51(1-2), 635-643.

- [35]. Colarossi, M., Trask, N., Schmidt, D. P., Bergander, M. J. (2012). Multidimensional modeling of condensing two-phase ejector flow. *international journal of refrigeration*, 35(2), 290-299.
- [36]. Yazdani, M., Alahyari, A. A., Radcliff, T. D. (2012). Numerical modeling of two-phase supersonic ejectors for work-recovery applications. *International Journal of Heat and Mass Transfer*, 55(21-22), 5744-5753.
- [37]. Yazdani, M., Alahyari, A. A., Radcliff, T. D. (2014). Numerical modeling and validation of supersonic two-phase flow of CO₂ in converging-diverging nozzles. *Journal of fluids Engineering*, 136(1), 014503.
- [38]. Smolka, J., Bulinski, Z., Fic, A., Nowak, A. J., Banasiak, K., Hafner, A. (2013). A computational model of a transcritical R744 ejector based on a homogeneous real fluid approach. *Applied Mathematical Modelling*, 37(3), 1208-1224.
- [39]. Banasiak, K., Palacz, M., Hafner, A., Buliński, Z., Smółka, J., Nowak, A. J., Fic, A. (2014). A CFD-based investigation of the energy performance of two-phase R744 ejectors to recover the expansion work in refrigeration systems: An irreversibility analysis. *International Journal of Refrigeration*, 40, 328-337.
- [40]. Palacz, M., Smolka, J., Fic, A., Bulinski, Z., Nowak, A. J., Banasiak, K., Hafner, A. (2015). Application range of the HEM approach for CO₂ expansion inside two-phase ejectors for supermarket refrigeration systems. *International Journal of Refrigeration*, 59, 251-258.
- [41]. Lucas, C., Rusche, H., Schroeder, A., Koehler, J. (2014). Numerical investigation of a two-phase CO₂ ejector. *International Journal of Refrigeration*, 43, 154-166.
- [42]. Banasiak, K., Hafner, A., Palacz, M. (2015). State of the art in the identification of two-phase transonic flow phenomena in transcritical CO₂ ejectors. In *Proceedings of the 24th IIR International Congress of Refrigeration* (pp. 80-88).
- [43]. Martin, K., Reiberer, R., Hager, J. (2006). Modeling of short tube orifices for CO₂.
- [44]. Fisher H G, Forrest H S, Grossel S S, Huff J E, Muller A R, Noronha J A, Shaw D A, Tilley B J 1992 Emergency relief system design using DIERS technology *The DIERS Project Manual* AIChE, New York.
- [45]. Chung, M. S., Park, S. B., Lee, H. K. (2004). Sound speed criterion for two-phase critical flow. *Journal of sound and vibration*, 276(1-2), 13-26.
- [46]. ISO/DIS4126-10 2008 Safety devices for protection against excessive pressure – Part 10 Sizing of safety valves for gas/liquid two-phase flow.

- [47]. Leung, J. C. (1986). A generalized correlation for one-component homogeneous equilibrium flashing choked flow. *AIChE Journal*, 32(10), 1743-1746.
- [48]. Leung J C 1995 *Int. Symp. on Runaway Reactions and Pressure Relief Design* Boston pp 367- 393.
- [49]. Banasiak, K., Hafner, A., Kriezi, E. E., Madsen, K. B., Birkelund, M., Fredslund, K., Olsson, R. (2015). Development and performance mapping of a multi-ejector expansion work recovery pack for R744 vapour compression units. *International Journal of Refrigeration*, 57, 265-276.
- [50]. Henning, H. M. (2007). Solar assisted air conditioning of buildings—an overview. *Applied thermal engineering*, 27(10), 1734-1749.
- [51]. Baniyounes, A. M., Ghadi, Y. Y., Rasul, M. G., Khan, M. M. K. (2013). An overview of solar assisted air conditioning in Queensland's subtropical regions, Australia. *Renewable and Sustainable Energy Reviews*, 26, 781-804.
- [52]. Güido, W. H., Lanser, W., Petersen, S., Ziegler, F. (2018). Performance of absorption chillers in field tests. *Applied Thermal Engineering*, 134, 353-359.
- [53]. Summerheat Publishable Report. Meeting cooling demands in summer by applying heat from cogeneration. April 2009.
- [54]. Hassan, H. Z., Mohamad, A. A. (2012). A review on solar-powered closed physisorption cooling systems. *Renewable and Sustainable Energy Reviews*, 16(5), 2516-2538.
- [55]. Ferreira, C. I., Kim, D. S. (2014). Techno-economic review of solar cooling technologies based on location-specific data. *International Journal of Refrigeration*, 39, 23-37.
- [56]. Zhai, X. Q., Qu, M., Li, Y., & Wang, R. Z. (2011). A review for research and new design options of solar absorption cooling systems. *Renewable and sustainable energy reviews*, 15(9), 4416-4423.
- [57]. Aphornratana, S., Sriveerakul, T. (2010). Analysis of a combined Rankine–vapour–compression refrigeration cycle. *Energy Conversion and management*, 51(12), 2557-2564.
- [58]. Nasir, M. T., Kim, K. C. (2016). Working fluids selection and parametric optimization of an Organic Rankine Cycle coupled Vapor Compression Cycle (ORC-VCC) for air conditioning using low grade heat. *Energy and Buildings*, 129, 378-395.

- [59]. Wang, H., Peterson, R., Harada, K., Miller, E., Ingram-Goble, R., Fisher, L., Ward, C. (2011). Performance of a combined organic Rankine cycle and vapor compression cycle for heat activated cooling. *Energy*, 36(1), 447-458.
- [60]. Wang, H., Peterson, R., Herron, T. (2011). Design study of configurations on system COP for a combined ORC (organic Rankine cycle) and VCC (vapor compression cycle). *Energy*, 36(8), 4809-4820.
- [61]. Li, H., Bu, X., Wang, L., Long, Z., Lian, Y. (2013). Hydrocarbon working fluids for a Rankine cycle powered vapor compression refrigeration system using low-grade thermal energy. *Energy and buildings*, 65, 167-172.
- [62]. Molés, F., Navarro-Esbrí, J., Peris, B., Mota-Babiloni, A., Kontomaris, K. K. (2015). Thermodynamic analysis of a combined organic Rankine cycle and vapor compression cycle system activated with low temperature heat sources using low GWP fluids. *Applied Thermal Engineering*, 87, 444-453.
- [63]. Dorantes, R., Lallemand, A. (1995). Influence de la nature des fluides, purs ou en mélanges non-azéotropiques, sur les performances d'une machine de climatisation à éjecto-compresseur. *International journal of refrigeration*, 18(1), 21-30.
- [64]. Sun, D. W. (1999). Comparative study of the performance of an ejector refrigeration cycle operating with various refrigerants. *Energy Conversion and Management*, 40(8), 873-884.
- [65]. Cizungu, K., Mani, A., Groll, M. (2001). Performance comparison of vapour jet refrigeration system with environment friendly working fluids. *Applied Thermal Engineering*, 21(5), 585-598.
- [66]. Selvaraju, A., Mani, A. (2004). Analysis of an ejector with environment friendly refrigerants. *Applied Thermal Engineering*, 24(5-6), 827-838.
- [67]. Kasperski, J., Gil, B. (2014). Performance estimation of ejector cycles using heavier hydrocarbon refrigerants. *Applied Thermal Engineering*, 71(1), 197-203.
- [68]. Huang, B. J., Chang, J. M., Wang, C. P., Petrenko, V. A. (1999). A 1-D analysis of ejector performance. *International journal of refrigeration*, 22(5), 354-364.
- [69]. Chen, J., Havtun, H., Palm, B. (2014). Parametric analysis of ejector working characteristics in the refrigeration system. *Applied Thermal Engineering*, 69(1-2), 130-142.
- [70]. Chen, J., Havtun, H., Palm, B. (2014). Screening of working fluids for the ejector refrigeration system. *International Journal of Refrigeration*, 47, 1-14.

- [71]. Gil, B., Kasperski, J. (2015). Efficiency analysis of alternative refrigerants for ejector cooling cycles. *Energy conversion and management*, 94, 12-18.
- [72]. Sun, D. W. (1996). Variable geometry ejectors and their applications in ejector refrigeration systems. *Energy*, 21(10), 919-929.
- [73]. Aphornratana, S., & Eames, I. W. (1997). A small capacity steam-ejector refrigerator: experimental investigation of a system using ejector with movable primary nozzle. *International Journal of Refrigeration*, 20(5), 352-358.
- [74]. Chunnanond, K., Aphornratana, S. (2004). An experimental investigation of a steam ejector refrigerator: the analysis of the pressure profile along the ejector. *Applied Thermal Engineering*, 24(2-3), 311-322.
- [75]. Eames, I. W., Ablwaifa, A. E., Petrenko, V. (2007). Results of an experimental study of an advanced jet-pump refrigerator operating with R245fa. *Applied Thermal Engineering*, 27(17-18), 2833-2840.
- [76]. Aidoun, Z., Ouzzane, M. (2004). The effect of operating conditions on the performance of a supersonic ejector for refrigeration. *International Journal of Refrigeration*, 27(8), 974-984.
- [77]. Boumaraf, L., Lallemand, A. (2009). Modeling of an ejector refrigerating system operating in dimensioning and off-dimensioning conditions with the working fluids R142b and R600a. *Applied Thermal Engineering*, 29(2-3), 265-274.
- [78]. Shestopalov, K. O., Huang, B. J., Petrenko, V. O., Volovyk, O. S. (2015). Investigation of an experimental ejector refrigeration machine operating with refrigerant R245fa at design and off-design working conditions. Part 1. Theoretical analysis. *international journal of refrigeration*, 55, 201-211.
- [79]. Shestopalov, K. O., Huang, B. J., Petrenko, V. O., Volovyk, O. S. (2015). Investigation of an experimental ejector refrigeration machine operating with refrigerant R245fa at design and off-design working conditions. Part 2. Theoretical and experimental results. *international journal of refrigeration*, 55, 212-223.
- [80]. Sadeghi, M., Mahmoudi, S. M. S., Saray, R. K. (2015). Exergoeconomic analysis and multi-objective optimization of an ejector refrigeration cycle powered by an internal combustion (HCCI) engine. *Energy Conversion and Management*, 96, 403-417.

- [81]. Zegenhagen, M. T., Ziegler, F. (2015). Experimental investigation of the characteristics of a jet-ejector and a jet-ejector cooling system operating with R134a as a refrigerant. *International Journal of Refrigeration*, 56, 173-185.
- [82]. Chen, J., Havtun, H., & Palm, B. (2014). Investigation of ejectors in refrigeration system: Optimum performance evaluation and ejector area ratios perspectives. *Applied Thermal Engineering.*, 64(1-2), 182-191.
- [83]. El-Dessouky, H., Ettouney, H., Alatiqi, I., Al-Nuwaibit, G. (2002). Evaluation of steam jet ejectors. *Chemical Engineering and Processing: Process Intensification*, 41(6), 551-561.
- [84]. Sun, D. W., Eames, I. W. (1996). Performance characteristics of HCFC-123 ejector refrigeration cycles. *International Journal of Energy Research*, 20(10), 871-885.
- [85]. Yu, J., Ren, Y., Chen, H., Li, Y. (2007). Applying mechanical subcooling to ejector refrigeration cycle for improving the coefficient of performance. *Energy Conversion and Management*, 48(4), 1193-1199.
- [86]. Mwesigye, A., Dworkin, S. B. (2018). Performance analysis and optimization of an ejector refrigeration system using alternative working fluids under critical and subcritical operation modes. *Energy conversion and management*, 176, 209-226.
- [87]. Varga, S., Lebre, P. S., Oliveira, A. C. (2013). Readdressing working fluid selection with a view to designing a variable geometry ejector. *International Journal of Low-Carbon Technologies*, 10(3), 205-215.
- [88]. Cooper, M. G. (1984). Saturation nucleate pool boiling-a simple correlation. In *ICHEME Symp. Ser. (Vol. 86, p. 786)*.
- [89]. Amalfi, R. L., Vakili-Farahani, F., Thome, J. R. (2016). Flow boiling and frictional pressure gradients in plate heat exchangers. Part 2: Comparison of literature methods to database and new prediction methods. *International Journal of Refrigeration*, 61, 185-203.
- [90]. Park, J. H., Kim, Y. S. (2004). Evaporation heat transfer and pressure drop characteristics of R-134a in the oblong shell and plate heat exchanger. *KSME international journal*, 18(12), 2284-2293.
- [91]. Shah, M. M. (1979). A general correlation for heat transfer during film condensation inside pipes. *International Journal of heat and mass transfer*, 22(4), 547-556.

- [92]. Martin, H. (1996). A theoretical approach to predict the performance of chevron-type plate heat exchangers. *Chemical Engineering and Processing: Process Intensification*, 35(4), 301-310.
- [93]. Kakaç, S., Liu, H., Pramuanjaroenkij, A. (2002). *Heat exchangers: selection, rating, and thermal design*. CRC press.
- [94]. Dittus, F. W., Boelter, L. M. K. (1985). Heat transfer in automobile radiators of the tubular type. *International Communications in Heat and Mass Transfer*, 12(1), 3-22.
- [95]. Wang, C. C., Chi, K. Y., Chang, C. J. (2000). Heat transfer and friction characteristics of plain fin-and-tube heat exchangers, part II: Correlation. *International Journal of Heat and mass transfer*, 43(15), 2693-2700.
- [96]. Quoilin, S., Declaye, S., Tchanche, B. F., Lemort, V. (2011). Thermo-economic optimization of waste heat recovery Organic Rankine Cycles. *Applied thermal engineering*, 31(14-15), 2885-2893.
- [97]. Botticella, F., De Rossi, F., Mauro, A. W., Vanoli, G. P., Viscito, L. (2018). Multi-criteria (thermodynamic, economic and environmental) analysis of possible design options for residential heating split systems working with low GWP refrigerants. *International Journal of Refrigeration*, 87, 131-153.
- [98]. Wildi-Tremblay, P., Gosselin, L. (2007). Minimizing shell-and-tube heat exchanger cost with genetic algorithms and considering maintenance. *International Journal of Energy Research*, 31(9), 867-885.
- [99]. Huang, B. J., Ton, W. Z., Wu, C. C., Ko, H. W., Chang, H. S., Hsu, H. Y., Yen, R. H. (2014). Performance test of solar-assisted ejector cooling system. *International journal of refrigeration*, 39, 172-185.
- [100]. Huang, B. J., Wu, J. H., Hsu, H. Y., Wang, J. H. (2010). Development of hybrid solar-assisted cooling/heating system. *Energy conversion and Management*, 51(8), 1643-1650.
- [101]. Autorità di Regolazione per Energia Reti e Ambiente. *Relazione annuale. Stato dei servizi*. 31 marzo 2019. Volume 1.
- [102]. Charnay, R. (2014). *Experimental study of flow boiling in horizontal minichannels at high saturation temperature (Doctoral dissertation)*.
- [103]. Lillo, G., Mastrullo, R., Mauro, A. W., Viscito, L. (2019). Flow boiling of R1233zd(E) in a horizontal tube: Experiments, assessment and correlation for

- asymmetric annular flow. *International Journal of Heat and Mass Transfer*, 129, 547-561.
- [104]. Mastrullo, R., Mauro, A. W., Viscito, L. (2017). Flow boiling of R32 in a horizontal smooth tube of 6.0 mm internal diameter: heat transfer coefficient and pressure drop. In *Journal of Physics: Conference Series* (Vol. 923, No. 1, p. 012015). IOP Publishing.
- [105]. Lillo, G., Mastrullo, R., Mauro, A. W., Viscito, L. (2018). Experimental study of flow boiling of propane in a 6 MM internal diameter horizontal tube. *Refrigeration, Sci. Technol*, 2018, 798-806.
- [106]. Mastrullo, R., Mauro, A. W., Revellin, R., Viscito, L. (2018). Flow boiling heat transfer and pressure drop of pure ethanol (99.8%) in a horizontal stainless-steel tube at low reduced pressures. *Applied Thermal Engineering*, 145, 251-263.
- [107]. Lillo, G., Mastrullo, R., Mauro, A. W., Viscito, L. (2019). Flow boiling of R32 in a horizontal stainless-steel tube with 6.00 mm ID. Experiments, assessment of correlations and comparison with refrigerant R410A. *International Journal of Refrigeration*, 97, 143-156.
- [108]. Lillo, G., Mastrullo, R., Mauro, A. W., Viscito, L. (2018). Flow boiling heat transfer, dry-out vapor quality and pressure drop of propane (R290): Experiments and assessment of predictive methods. *International Journal of Heat and Mass Transfer*, 126, 1236-1252.
- [109]. Labview release. Austin, Texas, United States of America. National Instrument.